UNIVERSITÀ DEGLI STUDI DI TRIESTE

XXXI CICLO DEL DOTTORATO DI RICERCA IN NANOTECNOLOGIE

BIORESORBABLE ENGINEERED MEMBRANES FOR GUIDED BONE REGENERATION WITH ANTIMICROBIAL PROPERTIES

Settore scientifico disciplinare: MED/28

DOTTORANDO

Federico Berton

COORDINATORE

Chiar.ma Prof. Lucia Pasquato

SUPERVISORE DI TESI

Chiar.mo Prof. Roberto Di Lenarda

CO-SUPERVISORI DI TESI

Prof. Gianluca Turco

Dott. Davide Porrelli

ANNO ACCADEMICO 2018/2019

UNIVERSITÀ DEGLI STUDI DI TRIESTE

XXXI CICLO DEL DOTTORATO DI RICERCA IN NANOTECNOLOGIE

BIORESORBABLE ENGINEERED MEMBRANES FOR GUIDED BONE REGENERATION WITH ANTIMICROBIAL PROPERTIES

Settore scientifico disciplinare: MED/28

DOTTORANDO
Federico Berton

COORDINATORE
Chiar.ma Prof. Lucia Pasquato

SUPERVISORE DI TESI
Chiar.mo Prof. Roberto Di Lenarda

CO-SUPERVISORI DI TESI
Prof. Gianluca Turco
Dott. Davide Porrelli

ANNO ACCADEMICO 2018/2019

TABLE OF CONTENTS

List of the abbreviations

β-TCP	beta tricalcium phosphate
BIC	bone to implant contact
BMPs	bone morphogenetic proteins
BPCi	conductivity index of bone particles
BV/TV	bone volume/total volume
CTL	lactose-modified chitosan
CTH	chitosan
DBBM	demineralized bovine bone matrix
DCM	dichloromethane
DMA	dynamic mechanical analysis
DMEM	Dulbecco's modified eagle medium
DMF	dimethylformamide
DW	distilled water
EDS or EDX	energy-dispersive X-ray spectroscopy
ELS	electrospinning
ETAAS	electrothermal atomic absorption spectrometry
FITC	fluorescein isothiocyanate
GBR	guided bone regeneration
GFs	growth factors
GDL	δ-glucono lactone
GPa	gigapascal
HMDS	hexamethyldisilazane
ICP-MS	inductively coupled plasma mass spectrometry
IGF-1	insulin like growth factor 1
L-PRF	leukocyte – platelet rich fibrin
LB	Luria Bertani
LDH	lactate dehydrogenase
LWR	London white resin
µCT	micro computed tomography
MTT	thiazolyl blue tetrazolium bromide
MW	molecular weight
nAg	silver nanoparticles
NB	native bone
NFB	newly formed bone
nHAp	nanohydroxyapatite
PBS	Phosphate-buffered saline
PCL	polycaprolactone
PCs	platelet concentrates
PDGF	platelet derived growth factor
PEO	polyethylene oxide
PRF	platelet rich fibrin
PRP	platelet rich plasma
Ra	roughness average
RG	residual graft
SBF	simulated body fluid
SEM	scanning electron microscopy

TFA	trifluoroacetic acid
Tb.N	trabecular number
Tb.Sp	trabecular spacing
Tb.Th	trabecular thickness
TGF-β	transforming growth factor beta
THF	tetrahydrofuran
TrSD	trabecular space dimensions
UniTS	University of Trieste
WD	working distance

Abstract

Background

The main topics of this doctoral thesis are bone regeneration and bone tissue analysis by means of nanotechnological strategies for both purposes. Briefly, the development of nanostructured membranes and scaffolds for bone regeneration procedures in oral surgery have been explored, together with the optimization of analysis protocols at the micro- and nano-scale. Therefore, three main chapters will be here described: (i) nanostructured electrospun membranes production, tailoring and analysis; (ii) nanofiber fibrin-based membrane production, tailoring and analysis; (iii) development of sound and reliable histological, histomorphometric, chemical and ultrastructural protocols for the analysis of hard tissues.

Materials and Methods

Considered that, at the first stages of this PhD project, the electrospinning device was not available at the University of Trieste (UniTS) Labs, the efforts were firstly conducted to i) acquire the knowledge about this technique and ii) the application of this methodology to the synthesis of biocompatible membranes.

The first attempts were addressed to reproduce some of the recent results reported in the scientific literature. Subsequently, thanks to the collaboration with the Tissue Engineering Laboratory, *Campus Biomedico* of Rome (Prof. Alberto Rainer), specific polymeric solutions have been prepared. Different solutions were prepared with promising results in terms of proper solvent evaporation, homogeneity of fiber diameters, and absence of defects such as beads, when electrospun.

Thereafter the necessary components for the ELS process were acquired, assembled and tested at UniTS. Different combinations of solvents for the preparation of polycaprolactone (PCL) based membranes were tested. Thereafter, an air-plasma activation process was applied in order to increase the membrane hydrophilicity. Qualitative characterization of membranes obtained by ELS, before and after plasma treatment has been performed together with the morphological analysis (orientation, presence of beads, fiber diameter) through Scanning Electronic Microscopy. The determination of surface wettability with contact angle measurements was performed. The optimal formulation was chosen for subsequent evaluation of hydrophilicity and morphology following the activation of the membranes.

Lactose-modified chitosan (CTL) was added by chemical adsorption on PCL membranes in order to increase their bioactivity. Moreover, CTL was used to deliver, on the membranes, silver nanoparticles (nAg) synthesized within CTL solution. Electrothermal Atomic Absorption

Spectrometry (ETAAS) analysis was performed to quantify nAg. MG63 cells cultured on PCL membranes with or without CTL were used for proliferation assay with daily timepoints until day eight. Lactate dehydrogenase (LDH) assay was used for cytotoxicity evaluation. The antibacterial activity of PCL-nAg membranes was tested in terms of biofilm inhibition on *Pseudomonas aeruginosa* (ATCC 27853) and *Staphylococcus aureus* (ATCC 25923), using the MTT test. Mechanical properties of the produced membranes were evaluated in dry conditions, after rapid soaking and after aging in Simulated Body Fluid (SBF). These tests were performed by means of uniaxial tensile tests for the evaluation of the elastic modulus, the deformation at failure and the ultimate tensile stress.

As second chapter of this thesis, the potentiality of another approach to produce nanostructured fibrin-based membranes was explored. These membranes were obtained by means of blood centrifugation and were tailored with a bone-inducing molecule, *i.e.* nano-hydroxyapatite (nHAp) (nanopowder, particle size <200 nm) for bone regeneration. The stability of pristine membrane in SBF was tested. At each time point, one sample was analyzed by means of SEM and subsequently with ImageJ processing tools. Then, the effects of the nHAp addition during the forming process of PRF (thus during centrifugation) were investigated.

As all the above-mentioned techniques were oriented to regenerate maxillofacial bone, a bone histomorphometric analysis protocol (not already present at UniTS at the time of writing of the present thesis) was optimized. This protocol was prepared and implemented with the ultrastructural SEM-EDS (Energy Dispersive Spectroscopy) analysis of hard tissues mounted on the histological slides. After a thorough literature analysis and a visit at the Core Facility Hard Tissue and Biomaterial Research" of Karl Donath Laboratory, University Dental Clinic of Vienna, a reliable protocol was optimized. Starting from *ex vivo* animal analysis, the protocol was extended to human bone regenerated with several different scaffolds, specifically: autografts, allografts, xenografts and alloplastic material. Human bone specimen belonged to research protocols dealing with (i) maxillary sinus augmentation with homologous bone block; (ii) bone defect treated with autologous bone particles and xenogenic cortical lamina; (iii) maxillary sinus augmentation with xenogenic particles. The experimental SEM-EDS analysis was firstly conduced on fresh bovine ribs also with inserted titanium implants, while further analyzes were conducted on grafted maxillary sinus with bone block.

Results

The production of nanostructured electrospun based bioactive membranes with antimicrobial properties started with the activation of pristine PCL membranes. The activation of the highly hydrophobic PCL membranes by means of the plasma-air treatment resulted in a drastic decrease of the contact angle. The resulted membranes had an estimated average thickness of 137.3 ± 7.0 µm and 215.6 ± 22.1 µm after 30 and 60 minutes of fiber deposition, respectively. Moreover, the membranes exhibited appropriate handling features for clinical use. In terms of mechanical properties, tested by means of uniaxial tensile test, plasma-activated PCL membranes exhibited higher toughness if compared to the untreated ones. Confocal microscopy analysis showed an improved adsorption of CTL (labelled with fluorescein) for the membranes treated with air-plasma if compared with the untreated ones. CTL adsorption was confirmed by means of ETAAS which showed a higher nAg content in membranes treated with a low energy air-plasma treatment and CTL-nAg at pH 7, thus confirming Raman findings. MG63 cells cultured on PCL membranes with or without CTL, showed a more sustained growth after 7 days on the CTL-coated membranes compared with untreated PCL membranes and PCL air-plasma treated membranes. Moreover, the presence of nAg did not hamper cell viability with respect to PCL membranes, as confirmed by LDH assay. The antibacterial activity of PCL-nAg clearly showed that the biofilm formation was strongly inhibited on the surface of PCL-CTL-nAg membranes. Mechanical resistance of the produced membranes, soaked and aged in Simulated Body Fluid (SBF) showed results superior to commercially available membranes.

For the experimental enrichment of PRF membranes the dissolution assay of the pristine membrane revealed a mean fiber diameter of 0.103 ± 0.05µm without any statistically significant differences during time; degradation assay showed a two-folds increase of the weight related to the SBF absorption in the first 2 days. From the third day a constant degradation was observed. In the time frame of this experiment, the dimensional stability of the fibrin structure up to day 7 suggested that PRF membranes may also be used uncovered in the oral cavity. After the two methods of tested nHAp enrichment for each condition a sediment of nHAp was observed to be present on the bottom of the vials. On the other hand, a limited amount of nHAp coating the fibers was detected by means of SEM-EDS analysis. Further efforts will be made to find out the best conditions to obtain a suitable coupling of the two agents without hampering the formation of fibers.

After histological preparation and optical microscope acquisition of images, the image analysis performed by means of Photoshop and ImageJ, provided data such as the relation between bone

volume/total volume; regenerated bone; residual graft particles; soft tissue; conductivity index; trabecular thickness and trabecular spacing; bone-to-implant contact ratio (BIC). For the chemical and microscopic analysis of hard tissues, SEM-EDS was used for calcium and phosphate quantification in different regions of the bone sample, after the re-lapping of the histological slide and its carbon coating. A specimen containing a titanium implant was analyzed in order to evaluate its interface with bone, and the cortical bone and the cancellous bone grown around the implant. Even if reference values are, to date, missing in the literature, it was possible to detect different grades of mineralization at the interface (different calcium concentration) and between cancellous and cortical bone.

Conclusions

The membranes produced by means of ELS showed promising results in terms of (i) reliability of production (ii) biocompatibility (ii) antimicrobial properties (iii) stability in SBF allowing the scheduling of further *in vivo* experiments with the obtained membranes. Parallelly, the experimental enrichment of PRF membranes, even showing nHAp adsorption, still need to be perfected to obtain a homogenous distribution of nHAp on membrane's surface.

Finally, the optimization of histomorphometric protocol, enhanced with the successful experimental use of SEM-EDS technology for mineralized tissue analysis, led to the formulation of a research group named "Bone Lab" registered in the Clinical Department of Surgical, Medical and Health Sciences of the University of Trieste, available also for third-party analysis.

Riassunto

Introduzione

Gli argomenti principali di questa Tesi di Dottorato sono la rigenerazione ossea e l'analisi del tessuto osseo mediante strategie nanotecnologiche per entrambi gli scopi. In breve, sono stati esplorati lo sviluppo di membrane e scaffold nanostrutturati per le procedure di rigenerazione ossea in chirurgia orale, insieme all'ottimizzazione dei protocolli di analisi su micro e nanoscala. Pertanto, verranno descritti tre capitoli principali: (i) produzione, ottimizzazione e analisi di membrane elettrofilate nanostrutturate; (ii) produzione, ottimizzazione e analisi di membrane a base di fibrina di nanofibre; (iii) sviluppo di protocolli istologici, istomorfometrici, chimici e molecolari riproducibili e affidabili per l'analisi dei tessuti duri.

Materiali e metodi

Tenendo conto del fatto che, nelle prime fasi di questo progetto di Dottorato, i dispositivi di *electrospinning* non erano disponibili presso i Laboratori dell'Università degli Studi di Trieste, gli sforzi sono stati inizialmente condotti per i) acquisire le conoscenze su questa tecnica e ii) l'applicazione di questa metodologia per la sintesi di membrane biocompatibili.

I primi tentativi furono indirizzati a riprodurre alcuni dei recenti risultati riportati nella letteratura scientifica. Successivamente, grazie alla collaborazione con il Tissue Engineering Laboratory, Campus Biomedico di Roma (Prof. Alberto Rainer), sono state preparate alcune soluzioni polimeriche. Sono state preparate diverse soluzioni con risultati promettenti in termini di corretta evaporazione del solvente, omogeneità dei diametri delle fibre e assenza di difetti come le *beads*.

Successivamente sono stati acquisiti, assemblati e testati i componenti necessari per il processo di ELS. Sono state testate diverse combinazioni di solventi per la preparazione di membrane a base di policaprolattone (PCL). Successivamente, è stato applicato un processo di attivazione aria-plasma al fine di aumentare l'idrofilia della membrana. La caratterizzazione qualitativa delle membrane ottenute da ELS, prima e dopo il trattamento al plasma, è stata eseguita insieme all'analisi morfologica (orientamento, presenza di *beads*, diametro della fibra) attraverso la microscopia elettronica a scansione. È stata determinata la bagnabilità della superficie con misurazioni dell'angolo di contatto. La formulazione ottimale è stata scelta per la successiva valutazione di idrofilia e morfologia a seguito dell'attivazione delle membrane.

Il chitosano modificato con lattosio (CTL) è stato aggiunto mediante adsorbimento chimico sulle membrane del PCL al fine di aumentarne la bioattività. Inoltre, CTL è stato utilizzato per incorporare, sulle membrane, nanoparticelle d'argento (nAg) sintetizzate all'interno della soluzione di CTL.

L'analisi ETAAS è stata eseguita per quantificare nAg. Le cellule MG63 coltivate su membrane PCL con o senza CTL sono state utilizzate per il saggio di proliferazione con *timepoints* giornalieri fino all'ottavo giorno. Il dosaggio della lattato deidrogenasi (LDH) è stato utilizzato per la valutazione della citotossicità. L'attività antibatterica delle membrane PCL-nAg è stata testata in termini di inibizione del biofilm su Pseudomonas aeruginosa (ATCC 27853) e Staphylococcus aureus (ATCC 25923), utilizzando il test MTT. La resistenza meccanica delle membrane prodotte è stata valutata dopo immersione e invecchiamento in Simulated Body Fluid (SBF), mediante prove di trazione uniassiali per la valutazione del modulo elastico, della deformazione a rottura e dello sforzo limite.
Come secondo capitolo di questa tesi, è stata esplorata la potenzialità di un altro approccio per produrre membrane a base di fibrina nanostrutturate. Queste membrane sono state ottenute mediante centrifugazione del sangue e sono state implementate con nano-idrossiapatite (nHAp) (nanopolvere, particelle di dimensioni <200 nm) per la rigenerazione ossea. È stata testata la durabilità di membrane native in SBF. Ad ogni tempo di indagine stabilito, un campione è stato analizzato con SEM e successivamente con gli strumenti di elaborazione del programma ImageJ. Inoltre, sono stati studiati gli effetti dell'aggiunta di nHAp durante il processo di formazione di PRF (quindi durante la centrifugazione).
Poiché tutte le tecniche sopra menzionate erano orientate a rigenerare l'osso maxillofacciale, è stato ottimizzato un protocollo di analisi istomorfometrica dell'osso (non ancora presente all'Università degli Studi di Trieste al momento della stesura della presente tesi). Questo protocollo è stato preparato e indagato tramite l'analisi ultrastrutturale SEM-EDS (Energy Dispersive Spectroscopy) dei tessuti duri montati sui vetrini istologici. Dopo un'attenta analisi della letteratura e una visita presso la Core Facility Hard Tissue and Biomaterial Research del Karl Donath Laboratory, University Dental Clinic di Vienna, è stato definito un protocollo riproducibile. A partire dall'analisi degli animali *ex vivo*, il protocollo è stato esteso all'osso umano rigenerato con diversi scaffold, in particolare: autotrapianti, allotrapianti, xenotrapianti e materiale alloplastico. I campioni di osso umano appartenevano a protocolli di ricerca riguardanti (i) aumento del seno mascellare con blocco osseo omologo; (ii) difetto osseo trattato con particelle ossee autologhe e lamina corticale eterologa; (iii) rialzo del seno mascellare con particelle xenogeniche. L'applicazione sperimentale dell'analisi SEM-EDS è stata inizialmente condotta su costole di bovino fresche con impianti di titanio inseriti, mentre ulteriori analisi sono state condotte su seno mascellare innestato con blocco osseo.

Risultati

La produzione di membrane bioattive nanostrutturate a base di PCL elettrofilate con proprietà antimicrobiche è iniziata con l'attivazione di membrane PCL native. L'attivazione delle membrane PCL altamente idrofobiche mediante il trattamento plasma-aria ha comportato una drastica riduzione dell'angolo di contatto. Le membrane risultanti avevano uno spessore medio stimato di 137,3 ± 7,0 µm e 215,6 ± 22,1 µm dopo 30 e 60 minuti di deposizione di fibre, rispettivamente. Inoltre, le membrane presentavano caratteristiche di maneggevolezza appropriate per l'uso clinico. In termini di proprietà meccaniche, testate mediante test di trazione uniassiale, le membrane PCL attivate al plasma hanno mostrato una maggiore tenacità rispetto a quelle non trattate. L'analisi microscopica confocale ha mostrato un miglior assorbimento di CTL (marcato con fluoresceina) per le membrane trattate con plasma ad aria rispetto a quelle non trattate. L'adsorbimento di CTL è stato confermato mediante ETAAS che ha mostrato un contenuto di nAg più elevato nelle membrane trattate con un trattamento plasma-aria a bassa energia e CTL-nAg a pH 7, confermando così i risultati delle analisi al Raman. Le cellule MG63 coltivate su membrane PCL con o senza CTL, hanno mostrato una crescita più sostenuta dopo 7 giorni sulle membrane rivestite CTL rispetto alle membrane PCL non trattate e alle membrane trattate con aria-plasma PCL. Inoltre, la presenza di nAg non ha ostacolato la vitalità cellulare rispetto alle membrane PCL, come confermato dal test LDH. L'attività antibatterica di PCL-nAg ha mostrato chiaramente che la formazione di biofilm era fortemente inibita sulla superficie delle membrane di PCL-CTL-nAg. La resistenza meccanica delle membrane prodotte, imbevute e invecchiate nel fluido corporeo simulato (SBF) ha mostrato risultati superiori alle membrane disponibili in commercio.

Per quanto concerne le membrane in PRF, il test di dissoluzione della membrana originaria ha rivelato un diametro medio delle fibre di 0,103 ± 0,05 µm senza differenze statisticamente significative nel tempo; il saggio di degradazione ha mostrato un aumento di due volte del peso correlato all'assorbimento di SBF nei primi 2 giorni. Dal terzo giorno è stato osservato una diminuzione costante del peso delle membrane in PRF. Nel periodo di tempo di questo esperimento, la stabilità dimensionale della struttura di fibrina fino al giorno 7 ha suggerito che le membrane PRF possono anche essere utilizzate esposte nella cavità orale. In entrambi i due metodi di arricchimento nHAp testati per ciascuna condizione, è stato osservato che un sedimento di nHAp era presente sul fondo delle fiale. D'altra parte, è stata rilevata una quantità limitata di rivestimento nHAp delle fibre mediante analisi SEM-EDS. Ulteriori sforzi saranno fatti per scoprire le migliori condizioni per ottenere un accoppiamento adeguato dei due agenti senza ostacolare la formazione di fibre.

Dopo la preparazione istologica e l'acquisizione di immagini al microscopio ottico, l'analisi delle immagini eseguita mediante Photoshop e ImageJ ha fornito dati come la relazione tra volume osseo / volume totale; osso rigenerato; particelle residue di innesto; tessuto molle; indice di conducibilità; spessore trabecolare e spaziatura trabecolare; rapporto di contatto osso-impianto (BIC). Per l'analisi chimica e microscopica dei tessuti duri, SEM-EDS è stato utilizzato per la quantificazione del calcio e del fosforo in diverse regioni del campione osseo, dopo la lucidatura del preparato istologico e del suo rivestimento in carbonio (solo alcuni rapporti sono disponibili in letteratura). È stato analizzato un campione contenente un impianto in titanio per valutare la sua interfaccia con l'osso e l'osso corticale e l'osso spongioso cresciuti attorno all'impianto. Anche se i valori di riferimento mancano ancora in letteratura, è stato possibile rilevare diversi gradi di mineralizzazione all'interfaccia (diversa concentrazione di calcio) e tra osso spongioso e corticale.

Conclusioni

Le membrane prodotte mediante ELS hanno mostrato risultati promettenti in termini di (i) affidabilità della produzione (ii) biocompatibilità (ii) proprietà antimicrobiche (iii) durata in SBF che consente la programmazione di ulteriori esperimenti in vivo con le membrane ottenute. Parallelamente, l'arricchimento sperimentale delle membrane PRF, che mostra anche l'adsorbimento di nHAp, deve ancora essere perfezionato per ottenere una distribuzione omogenea di nHAp sulla superficie della membrana.

Infine, l'ottimizzazione del protocollo istomorfometrico, migliorata con l'uso sperimentale riuscito della tecnologia SEM-EDS per l'analisi dei tessuti mineralizzati, ha portato alla formulazione di un gruppo di ricerca chiamato "Bone Lab" registrato presso il Dipartimento Universitario Clinico di Scienze Mediche, Chirurgiche, e della Salute dell'Università degli Studi di Trieste, disponibile anche per analisi in conto terzi.

Introduction and thesis objectives

General introduction

Tissue regeneration and tissue engineering represent highly multidisciplinary fields that combine different approaches to restore, maintain or improve tissue and organ functions of the human body [1]. These fields arise from the combination of materials engineering, biology and medicine, and explore the use of biomaterials, cells, growth factors (GFs), nanomedicine, immunomodulation, gene therapy and other strategies. The design of biomaterials is aimed at the preparation of hydrogels, scaffolds, membranes, and fillers that have to allow, sustain and promote cell adhesion, migration, proliferation, differentiation and function.

Bone tissue is a specialized connective tissue that plays key roles in several physiologic functions: protection and support for organs, movement, blood production, storage and homeostasis of calcium and other minerals, blood pH regulation, mesenchymal and hemopoietic cell progenitors housing [2]. It is formed of inorganic mineral crystals, that accounts for the 60-70% of the dry mass; the principal mineral component is hydroxyapatite [HAp, $Ca_{10}(PO_4)_6(OH)_2$], but there are also small amounts of other inorganic salts. The remaining part of the dry mass is composed for the 10–20% by collagen fibers, with a prevalence of collagen type I, proteoglycans and non-collagenous proteins such as osteocalcin, osteopontin, osteonectin, fibronectin and thrombospondin [3]. According to the structure, bone can be categorized in two types: the cortical (compact) and the trabecular (cancellous or spongy) bone. The 80% of the skeletal bone is composed of cortical bone; it possesses an elastic modulus around 20 GPa and a limited porosity (5-10%) and its average ultimate compression strength is 105-131 MPa [4,5]. In contrast, the porosity of trabecular bone is higher (approximately 50–95%), but it presents lower mechanical properties: the elastic modulus ranges from 25 to 240 MPa, while the ultimate compressive strength ranges from 0.2 to 10.4 MPa [6]. The jaw bones represent the field of interest of the regeneration of mineralized tissues for an oral surgeon. The jaws show both cortical and cancellous bone, house the teeth and can encounter atrophy after tooth loss, periodontal disease, infections and traumas. The functional and clinical direct consequence of bone resorption is the incapability of restore properly edentulism or tooth bone support. In the oral field the same principles of tissue engineering have been explored through the design of scaffolds, membranes, injectable materials to ameliorate physiologic bone regeneration in terms of time, volume and quality. In particular, a surgical procedure named guided

bone regeneration (GBR) follows the principle of tissue isolation and separation with volume maintenance. GBR guides the bone matrix through the formation of mineralized bone, separating it from faster turn-over tissues such as connective and epithelial, and preserving the newly formed bone tissue from tissue shrinkage and muscular activity (*e.g*. tongue, cheeks). Commonly used materials for GBR are affected by mechanical, biocompatibility and resorbability limits, which can be overcome by different strategies such as nanotechnologies. In this field, nanofibers and especially electrospun nanofibers, are interesting for applications in the production of membranes based on both synthetic and natural polymers. Besides, despite autologous bone substitutes have shown historically the best performances in bone regeneration, they bring the inner limitation of a second surgical donor site together with patient's augmented mobility. From 2000 however, the easy technique of generate hemoderivatives directly from the patient's peripheral blood in outpatient procedure gain attention in scientific and clinical community. Second generation of hemoderivatives such as leucocyte derived PRF (L-PRF) have shown promotion of soft tissue healing thanks to the platelet growth factors (PDGF, VEGF, IGF, EGF, FGF, TGFβ-1) [7]. However, probably because of the documented limited *in vitro* durability of GFs, they appear not enhancing bone healing. Nonetheless scientific research is exploring the tunability of these implantable fully autologous scaffolds and membranes with biocompatible and osteoinductive materials.

Bone regeneration via electrospun nanofiber membranes

Nanofibers in Tissue Engineering (TE) represent an extremely attractive subgroup of biomaterials due to their unique intrinsic properties. Nanofiber-based membranes or scaffolds exhibit high surface-to-volume *ratio*, which allows an improved cell adhesion. Moreover, these structures offer tunability with proteins, drugs and ligands. The mechanical and morphological properties are even more promising thanks to the customizing dimensions of the fibers, their orientation and packing, porosity and density. Finally, the resulted three-dimensional structure of the obtained nanostructured material mimics the morphology of the extracellular matrix, consisting predominantly of collagen fibrils, coupled with elastin and other macromolecules such as glycoproteins [8]. Furthermore, nanofibers can promote specific cellular functions such as adhesion, proliferation, differentiation, and modulate stem cell behaviour [9,10].

Several techniques have been proposed in literature to fabricate nanofibers: phase separation technique [11], self-assembly fibers [12], template synthesis [13] and electrospinning [14] to name some. Among these techniques, electrospinning is a cost-effective technique that can be used to

prepare nanofibers. Electrospinning (ELS) technique has risen its popularity since its early development in the 1930s [15] along with the refinements of its basic components and setup.

This technique is used for polymeric solutions that can be modified and enriched with bio-active molecules. Thanks to their features, electrospun nanofibers have been attractive also in the dental field: periodontal regeneration [16], coatings for caries prevention [17], enrichment of resin composites [18], implant surface modification [19], wound healing of mucosa [20], drug releasing systems [21] and bone regeneration [22]. In GBR, membranes should maintain the shape of the defect in which the bone is stimulated to regenerate. The membrane should also protect the initial blood clot from any compression, shielding the bone matrix during maturation from infiltration of soft tissues cells. Therefore, these membranes should maintain suitable mechanical properties at least for three months of permanence exhibiting at the same time a proper bio-degradability which avoids second surgery for patients [23,24].

The most studied electrospun polymers in this field can be classified into natural polymer and synthetic polymer, also blended. Nanofibers prepared with synthetic polymers exhibit better mechanical properties than those based on natural ones. An interesting strategy to ameliorate nanofibers mechanical properties and bioactivity is to combine different synthetic polymers or natural polymers or even to mix natural with synthetic polymers [25]. Some examples of studied polymers are PCL (polycaprolactone) [26], PLA (polylactic acid) [27], alginate [28], hyaluronic acid (HA) [29] chitosan [30], silk fibroin [31], PLGA poly(lactic-co-glycolic acid) [32], cotton cellulose [33], PTFE (polytetrafluorethylene) [34]. These polymers have been also used in combination with mineral compounds such as hydroxyapatites or nano-hydroxyapatites, calcium phosphate, tricalcium phosphate, etc., as nanoscaled reinforce and/or to improve the bioactivity. It has been shown that the performance of a simple polymer can be positively affected by the introduction of small amount (< 1 wt.%) of nanoscale reinforcements [35]. The latest research is focused on functionalizing polymeric nanostructured electrospun membranes with antimicrobial and bone promoting agents. For the former action, the most commonly used agents are represented by amoxicillin [36], metronidazole [37], ciprofloxacin [38] (as antibiotics); Polyvinylpyrrolidone [39], silver nanoparticles [30], zinc oxide [40]. For the latter property, BMPs [41], diphosphonates [42] and naringin [43] have been investigated. Among the numerous polymers already presented in literature for ELS, PCL was chosen for this research project because its favourable characteristics (resorbability, tunability, biocompatibility, ease of production, ease of spinnability). Most of all, the FDA approval for its use in implantable devices appeared to be of paramount importance. This

aspect prospectively gives this basis research a clinical purpose and an easier translation from the bench to the bedside [44]. Moreover, among biodegradable synthetic polymers PCL is the one with the slowest degradation kinetic [45].

The versatility offered by ELS make possible the preparation of bi- or multilayered membranes, which can have different properties on the two sides of the membrane, corresponding to different tissue compartment in the surgical site of application [46]. Ideal membranes for guided bone regeneration should be biocompatible, space making, permeable to fluids but acting as barriers for cells, slowly resorbable, bone promoting and coupled with antimicrobial properties; expectantly not expensive. All the aforementioned properties can be reached starting from electrospun polymers or polymer mixtures, which result in nanostructured membranes with proper mechanical properties that can eventually be tuned with antimicrobial and bone-promoting compounds. Yang and co-workers successfully fabricated PLGA/HAp collagen/amoxicillin nanofiber membranes through coaxial electrospinning: in vitro analysis showed hydroxyapatite deposition on the membrane, a release of amoxicillin up to 40 hours and no signs of fibroblasts on the opposite side of the membrane after 48 hours of culture [47]. More recently, Lian and co-workers developed a bi-layered electrospun membrane with osteogenic and antibacterial properties based on a softer layer of (PLGA)/gelatin nanofibers incorporating dexamethasone-loaded mesoporous silica nanoparticles (DEX@MSNs), and a denser layer of PLGA nanofibers loaded with doxycycline hyclate (DCH). *In vitro* evaluation showed the effective antibacterial potency of the DCH/PLGA membrane together with an enhanced osteoinductive capacity for rat bone marrow stromal cells (BMSCs) [46]. Moreover, the Chinese group of He *et al*. verified the antimicrobial properties and bone formation induction of an electrospun composite membrane made of gelatin (Gln) and chitosan (CS) containing hydroxyapatite nanoparticles (nHAp) and (Pac-525)-loaded PLGA microspheres (AMP@PLGA-MS)[48]. Permeability was successfully tested for a PCL/PLGA electrospun membrane with the fluorescein isothocyanate-bovine serum albumin (FITC-BSA; Sigma) used as a nutrient model [49]. The permeability through the membrane is important for the supply of nutrients and oxygen, and for the occurrence of the essential processes of bone regeneration, therefore one of the goals of the manufacturing of this PCL/PLGA membrane for GBR was the addition of two hydrophilic additives to PLGA and PCL, respectively: Pluronic F127 (Mw 12,500; BASF, Parsippany, NJ) and Tween 80 (polysorobate 80; Yakuri Pure Chemicals, Japan). Simultaneously, to date, the state of the art of commercially available resorbable membranes is represented by the cross linked heterologous collagen-based (type I and type III, derived from swine) bilayer membrane Bio Gide®

(Geistlich Pharma AG, Wolhusen, Switzerland); whereas the non-degradable benchmark product is a titanium reinforced expanded polytetrafluoroethylene (ePTFE) membrane named Cytoplast® (Osteogenics Biomedical, Lubbock, USA). Hence, is evident the paramount disparity in terms of technology and fabrication processes between the commercially available membranes and the state of the art of scientific research. At the time of writing this PhD Thesis, the evidences reported in literature remains at the *in vitro* or *in vivo* (animal model, small sizes) level. Thus, someone might argue if the promising results reported by the basic research, may be similarly good in the human application or even superior to the current outcomes.

Bone regeneration with enriched hemoderivatives

Platelet-rich fibrin (PRF) belongs to a second generation of platelet concentrates, as its processing is simplified and no biochemical treatment of blood is required [50]. Nowadays, it is known that platelets play a crucial role not only in hemostasis, but also in the wound healing process. In 1974 the theory concerning a possible regenerative potential of platelets was introduced for the first time; Ross *et al.* in 1974 [51] were the first authors to describe a platelet growth factor. Gassling *et al.* [52] published a study in 2010 where the authors compared the use of the PRF membrane with the collagen membrane (Bio-Gide) to evaluate which membrane was the best suitable form GBR. The authors observed that after the activation of the platelets trapped inside the fibrin matrix, the released growth factors stimulated the mitogenic response in the periosteum, inducing a better wound healing. Platelet-rich plasma (PRP) was used as a means to introduce growth factors such as PDGF, TGF-β and IGF-1 in the surgical site, in order to enrich the physiological clot to accelerate wound healing and stimulate bone regeneration [53]. Generally, a human blood clot consists of 95% of erythrocytes, 5% of platelets, less than 1% of leukocytes and millions of fibrin filaments. A PRP clot contains about 4% of erythrocytes, 95% of platelets and 1% of white blood cells [54].

The birth of a second family of blood derivatives (called second generation blood products) can be ascribed to the studies of Dr. Joseph Choukroun in the early 2000s, inventor of the PRF. Choukroun thought of a simple and inexpensive protocol to obtain the PRF: 9ml of blood is taken from the patient and the tube, without adding anticoagulant, is immediately centrifuged at 3000 rpm for 10 minutes. Choukroun observed that the architecture of fibrin was deeply dependent on the polymerization processes and the preparation technique, concluding that the slow polymerization of the PRF seems to generate a fibrin network very similar to the natural one, with the advantage of a more efficient migration and cell proliferation. In order for fibrinogen to polymerize, the inner surface of the tube must be coated with silica, which acts as an activator. Without the addition of

anticoagulants, the platelets soon activate the coagulation cascade. The platelets are located in a massive way in the fibrin mesh, so as to release the growth factors. The fibrin network allows the progressive release of growth factors in a time frame of about 7-11 days. According to the study conducted by Simonpieri *et al.* [55], the use of the PRF membrane in bone grafting offers four advantages:

• First, the fibrin clot has an important mechanical role, in fact the PRF membrane maintains and protects the additional grafted biomaterials, as well as acting as a biological connector between the wound and the adjacent areas.

• Secondly, the PRF membrane facilitates cell migration, in particular for the endothelial cells necessary for neo-angiogenesis, vascularization and graft survival.

• Platelet cytokines (PDGF, TGF-β, IGF-1) are gradually released as the PRF matrix is reabsorbed, thus supporting a perpetual healing process.

• The presence of leukocytes and cytokines in the fibrin clot plays a significant role in the self-regulation of inflammatory and infectious phenomena within the grafted material.

In the literature there are numerous scientific articles which confirm that in the PRF protocol the absence of the use of thrombin and calcium chloride (as in PRP production) allows to obtain a fibrin clot with a physiological and very elastic molecular structure [56][57][50]. Furthermore, the growth factors being released for over a week, allow for rapid healing of soft tissues, particularly during the first two weeks of healing, which appear to be the most critical [58].

Conversely, enhanced bone regeneration remains still controversial. Apparently, based on scientific clinical evidence, PRF seems not to help to ameliorate bone regeneration efficiency. However there is a great effort in basic research to enrich the hemoderivatives with bone promoting agents such as alendronate [59], DBBM [60], β-TCP [61] with promising results compared with the bone promoting agents or PRF alone.

Bone regeneration analysis

Histomorphometry is a highly specialized type of analysis performed on histological sections that aims to evaluate parameters concerning the structure of bone tissue (trabeculae, bone marrow, cortical bone), resorption and its new formation. It is therefore essential to assess the degree of tolerability and the effectiveness of a treatment at the bone level and to highlight the physiopathological mechanisms in place. In particular, the histomorphometry is the only means that allows a study of the bone tissue on three levels: cellular, of the single remodelling unit and tissue. This analysis allows the visualization of an image in two dimensions, with a high resolution and a

high contrast. Bone biopsy is the way to harvest the specimen from the living body. The sample must be taken through the use of a drill with a low number of revolutions and under copious irrigation to avoid possible alterations to the bone structure. The analysis is based on the evaluation of three types of measurements that include perimeters, areas and lengths that together will give a presentation of the two-dimensional structure of the sample, highlighting areas, distances and distributions. What histomorphometric analysis usually aims at evaluating concerns neoformation and bone resorption, the distribution of the different components and the cell population. This aspect is fundamental for the analysis of regenerated bone starting from a scaffold or a membrane: parameters such as connectivity index, highlights the biocompatibility and osteoconductivity of a bone substitute. Taking into account, for example, the value of Tb.N, which indicates the number of trabeculae present, it can be referred to the mechanical properties of the analyzed bone.

The parameters related to bone microarchitecture, in fact, are particularly important for assessing bone quality, as they seem to be the main risk factor for fracture. This can be demonstrated through the Euler principle according to which an important resistance to compression is lost in the case in which a single horizontal trabecula is reabsorbed.

Histomorphometry represents the gold standard in the analysis of the two-dimensional structure of the bone, with particular attention to microarchitecture and the distribution of trabeculae. However, other techniques have been introduced as supplementary analysis, such as micro-CT, which provides a more detailed three-dimensional evaluation.

The histomorphometric analysis, in fact, being only two-dimensional, does not take into account the way in which the different dimensional classes are connected to each other, as for example one could evaluate through the more modern Trabecular Space Dimension (TrSD) parameter. TrSD may help to traduce a bidimensional assessment of a bone in a more realistic three-dimensional one. Histomorphometry is also a time-consuming technique and the procedures for obtaining the sample to be analyzed are invasive. In a recent article by Gandolfi *et al.* [62] in which an EDX analysis was performed on nine titanium implant specimens with surrounding bone, extracted after a period of time ranging from two months to 17 years. Nitrogen (N) values and those related to calcium (Ca) and phosphorus (P) have been identified and collected in order to determine the mineralization of bone tissue (Ca / N, P / N). In this way, also SEM with EDX may support mineralised tissue analysis in a deeper manner, studying qualitatively and quantitatively interface between native bone and scaffolds or implanted system or the degree of mineralization.

AIM of the research

Nanofiber based membranes and scaffolds represent an extremely interesting starting point for development of implantable device for bone regeneration purposes. Nowadays clinical practice is pretty far from the results and the prospective of the basic research, thus the implementation of new research protocols based both on electrospun synthetic and natural polymers together with the enrichment of autologous hemoderivatives represent the starting point of this thesis. Finally, the analysis of the efficacy of these devices need to be thoroughly investigated through qualitative and quantitative methods such as histomorphometry and SEM-EDS ultramolecular analysis of mineralized tissues. Thus, this thesis has three main objectives, as depicted in Fig. 1:

- the production of a novel nanostructured electrospun membrane based on PCL enriched with nAg as antimicrobial agent and CTL as bioactive molecule;
- the enrichment of a nanostructured autologous hemoderivatives membranes with HAp;
- the optimization and introduction as standard research protocol at University of Trieste of histomorphometric analysis and SEM-EDS experimental application to the mineralized tissues analysis.

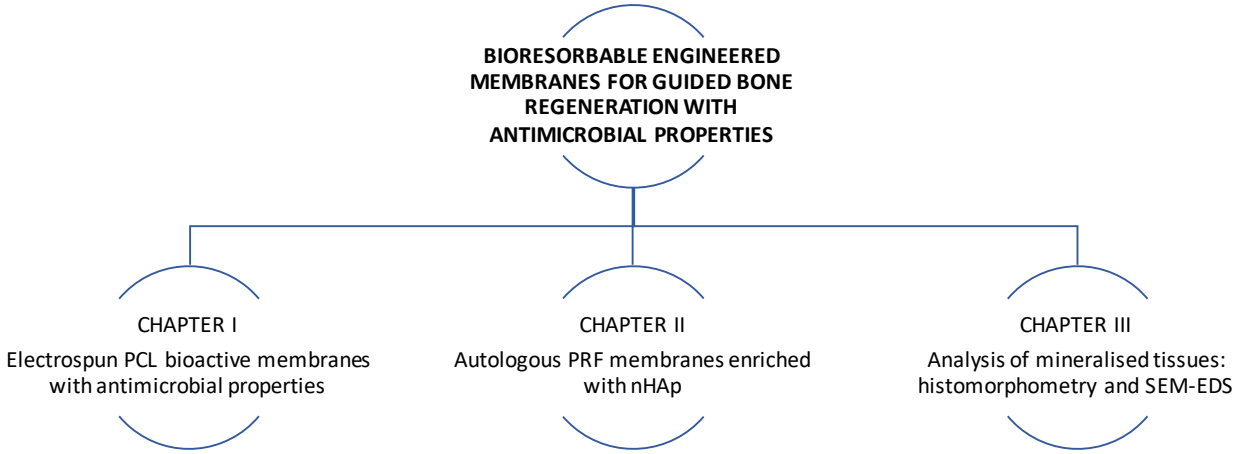

Fig. 1: Schematic representation of the thesis organization.

Variables affecting electrospinning process

Despite the broad spectrum of polymers that can be electrospun, an equilibrium between the physical and chemical properties and the ratio between the solute and the solvents has to be thoroughly seek, along with the multiple variables that may affect the final morphology of the obtained fibers. A list of the relevant parameters is provided in the following table (Tab. 1) [63–65].

Solution parameters	**Process parameters**	**Environmental parameters**
Viscosity	Voltage	Humidity
Concentration	Flow rate	Temperature
Conductivity	Shape of collector	Air flow of the chemical hood
Dielectric constant	Needle gauge	-
Surface tension	Distance	-
Charge of jet	Angle	-
Solvent type	Motion	-
Polymer type	-	-
Polymer molecular weight	-	-
Polymer solubility	-	-
Boiling point	-	-

Tab. 1: a list of the relevant parameters that may affect the final morphology of electrospun nanofibers is provided.

The final goal of the process is the fabrication of nanofibers with diameters at the nanoscale and without the presence of defects (*e.g.* beads, which are the expression of incomplete solvent evaporation). Precise choice of the principal polymer and its adequate solvents should be settled in order to obtain limited surface tension, adequate viscosity and charge density. This has to favour the formation of a continuous flow, which must not collapse in droplets, or beads, after potential difference administration. Both viscosity and surface tension, in conjunction with polymer molecular weight, polymer concentration, conductivity of the solution, influence the fiber morphology and porosity.

Molecular weight depends on the chain length of the polymer and can be related to the entanglements of the molecules. This fact explains why high molecular weight results in viscous solutions compared to low molecular weight. Therefore, the molecular weight of the polymer should be correctly considered for the selection of solvents and concentrations. Indeed, if the solution exhibit too high viscosity, this will hamper the flow through the capillary and the polymer may dry up or drip at the needle tip. Conversely, solutions with relatively low concentration will result into droplets.

Solubility and boiling point of the solvent are paramount factors. Volatile solvents are ideal options due to rapid evaporation during the transit from the needle tip to the collector [66]. High boiling points solvents may not evaporate completely prior to hit the target, resulting in flat ribbon shape fibers (Fig. 2) instead of circular fibers, presence of beads or other defects (Fig. 3) [67]. The volatility of the solvent may affect the final microscopic characteristics of the obtained fibers including porosity, shape and size.

Fig. 2: nanofiber-based membrane obtained with the following parameters: chitosan 2.5% w/V + lactose-modified chitosan 0.5% w/V in acetic acid 90%, 15 kV of potential, 27G needle, 0.6 ml/h of flow rate. Ribbon-like fibers can be appreciated. Quanta250 SEM, FEI, Oregon, USA; 2000x.

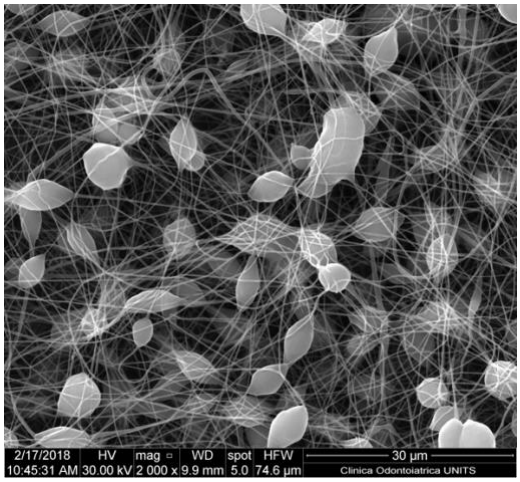

Fig. 3: nanofiber-based membrane obtained with the following parameters: PCL 6% w/V in DCM/methanol (MeOH) 7:3, 17 KV of potential, 27G needle, flow rate of 0.6 ml/h. The formation of multiple beads can be appreciated. Quanta250 SEM, FEI, Oregon, USA; 2000x.

Besides the aforementioned process parameters, which are mainly related to the polymeric solution, several others have to be taken into consideration: voltage, distance between the needle tip and the collector, flow rate, needle gauge and type of collector. Starting from the latest, in the conventional ELS set up, collectors can be static, round shaped and covered by a common aluminium foil. According to the final macroscopic structure of the biomaterial however, the collector can be oscillating, or rotative and can be flat or cylindrical. Nanowire-in-microtubes can be obtained in contrast with co-electrospinning: an alternative setup which allows for the production of core-shell fibers and inner hollow fibers [68–70]. The electrodes applied both on the metallic needle and on the collector, bring the potential difference from the energy supply. Many combinations of voltage can be administered: usually from 7 kV to 35 kV, distributed equally or diversely between the needle tip and the collector. The flow rate of the syringe pump should be regulated in accordance with the applied voltage in order to maintain a continuous collection of fibers on the target. Comparing low with high voltages, these latter result in a smaller Taylor cone and, therefore, in thinner fibers with higher rate of deposition on the target. However, critical voltage may vary among polymeric solutions. The formation of thinner nanofibers with an augmentation of the applied voltage is attributed to the stretching of the polymer solution in correlation with the charge repulsion within the polymer jet. The increases in the diameter and formation of beads with an increase in the applied voltage are attributed to the decrease in the size of the Taylor cone and increase in the jet speed for the same flow rate [71]. The higher the voltage, the larger the fiber diameter due to the increased feed rate. Diversely, the increment of the flow rate would turn in occurrence of defects (beads) because of the improper evaporation of the solvent, prior to the fiber deposition [64]. The

proper regulation of the flow rate is also function of the distance between the metallic needle and the collector. This parameter should allow for the correct solvent evaporation during the transit between the source and the target.

Depending on the polymer and the solvent, the needle diameter can vary. Smaller internal diameter reduces the probability of occlusion of the spinneret due to less exposure time of the jet to the environment. Reduction in needle internal diameter increases the surface tension of the solution corresponding to smaller droplet. This causes the decrease of Jet acceleration. So jet gets more flight time before deposition; this results in smaller diameter of the fibers [65]. Usual needle diameters are reported to be from 18G to 30G [72–74].

In order to stabilize the Taylor cone, the flow rate needs to be adjusted in a correct range. A constant and stable flow rate is necessary to minimize the beads formation in the electrospun web of fibers [64]. A lower flow rate is preferable to let the solvent evaporate properly [75]. However, there should always be a minimum feed rate of the spinning solution. It has been observed that the fiber diameter and the pore diameter (*i.e.* the void portion of the structure) increase with increased polymer flow rate and by changing it, the morphological structure can be slightly altered. Few studies have systematically investigated the relationship between solution feed or flow rate and the fiber morphology and size [76,77]. Nonetheless, it can be stated that high flow rates result in beads due to the not optimal drying time prior to fiber accumulation on the target [78,79]. Along with the feed rate, also the needle-to-collector distance affects the solvents evaporation: as the distance increases, using the same voltage the magnitude of the electric field decreases. However, the effect of needle-to-collector distance on fiber morphology is not as significant as the other parameters. Common reported distances for solution ELS are 15 cm to 30 cm [72]. Another important variable is represented by conductivity of the solution. High conductivity enables polymer solutions to carry greater charge compared to low conductivity. Therefore, high conductivity yields greater tensile forces and reduction in nanofiber diameter [80]. Generally, electrospun nanofibers with the smallest fiber diameter can be obtained with the highest electrical conductivity and it has been found that the jet radius varies inversely with the cube root of the electrical conductivity of the solution [81]. Conductivity of polymer solution can also be enhanced using surfactants. The approach of increasing the solution conductivity by salt addition has also been explored for polymers such as, polyoxyethylene oxide (PEO) [82], collagen type I-PEO [83], PVA [84], polyacrylic acid (PAA) [85], polyamide-6 [86] and others.

Apart from solution and processing parameters, also the ambient parameters (*e.g.* humidity, pressure and temperature) influence the fiber morphology. The variation in humidity while spinning polystyrene solutions was studied and it was showed that an increase in the humidity results in the appearance of small circular pores on the surface of the fibers; a further increase in the humidity leads to the pores coalescing [87]. In 2004 the effect of temperature, ranging from 25 to 60 °C, was investigated on the ELS of polyamide-6 fibers and it was found that higher temperatures led to smaller fiber diameter. The authors attributed this phenomenon to the decrease in the viscosity of the polymer solutions at increased temperatures [86].

Material and methods

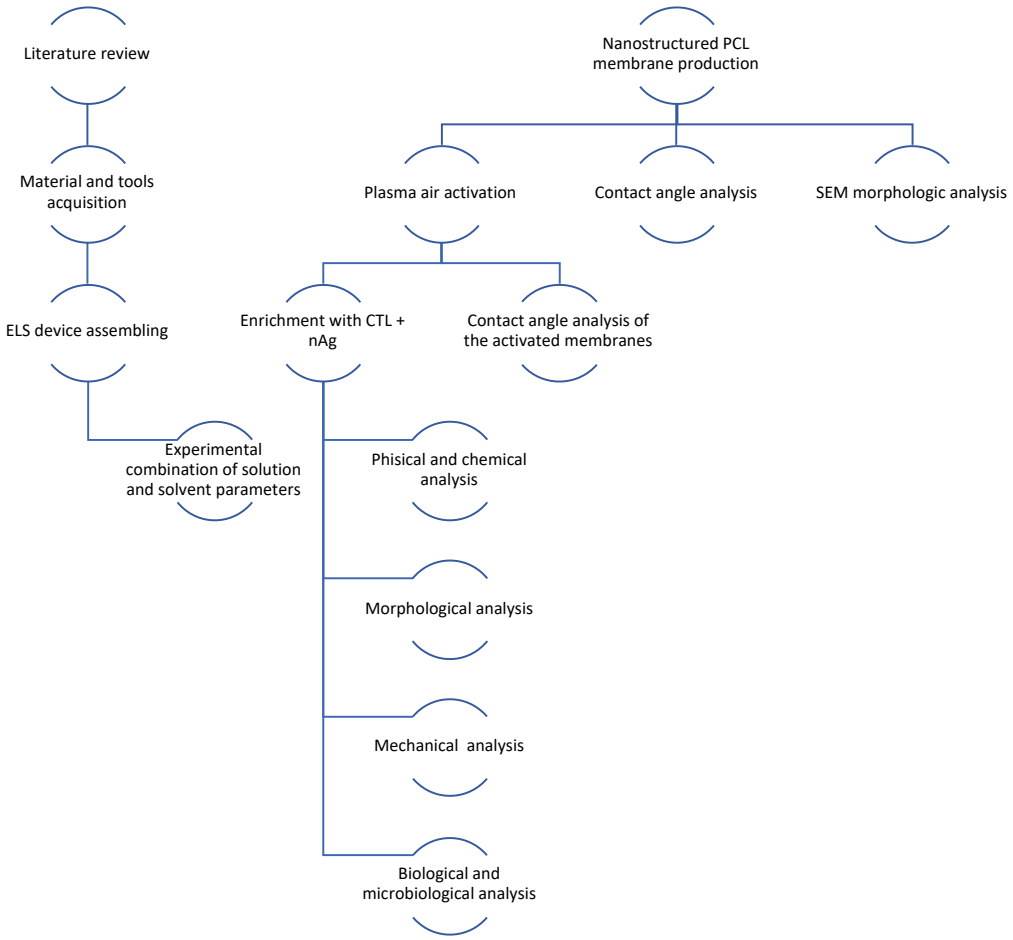

Fig. 4: experimental set-up

Electrospinning device assembly

This technique was firstly applied in 1934 by Anton Formhals and represents a combination of two techniques which are the electrospray and the spinning of fibers [88]. A high electric field is applied to both the syringe needle, which contains a polymeric solution, and to the collector (Fig. 5).

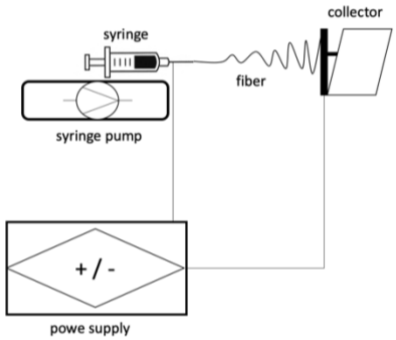

Fig. 5: schematic representation of the essential set-up of an electrospinning device.

The collector and the syringe needle are kept at the proper distance one from the other. Metallic plates, aluminium foils and rotating drums can be used as target for the collection of nanofibers during the electrospinning process. The potential difference is able hence to overcome the surface tension of the polymeric solution ejected from the needle tip and assume the so called “Taylor cone” configuration [89] (Fig. 6). This process shapes the polymeric solution into a jet of charged fluid that is electrostatically attracted by the collector. The solvent evaporates during this transit from the needle to the collector allowing for the accumulation of dry fibers on it.

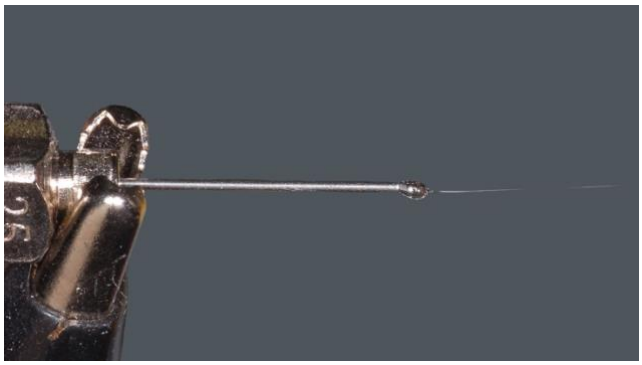

Fig. 6: Taylor cone obtained with the following parameters: a solution of polycaprolactone (PCL) 12% w/V in dichloromethane/dimethylformamide (DCM/DMF) 7:3 applying 17 kV of potential and 0.6 ml/h of flow rate and using a 25G needle. Nikon D3500, macro 105 Sigma tamron lens, Sigma ring flash.

Experimental setup

The set-up for carrying out the ELS experiments (Fig. 5) consists of several components: first, a syringe containing the polymeric solution, a needle is applied to it and the syringe is positioned on a syringe pump, which has the function of regulating the flow rate with which the polymer solution will be extruded from the syringe; in front of this system there is a target covered with an aluminium sheet on which the fibers will be collected during the formation phase. The needle positioned on the syringe and the collector are both connected to an electric potential generator to allow the formation of an electric field at the two ends capable of breaking the surface tension of the solution containing the polymer dissolved in the solvents and thus generating the fiber that will deposit on the collector.

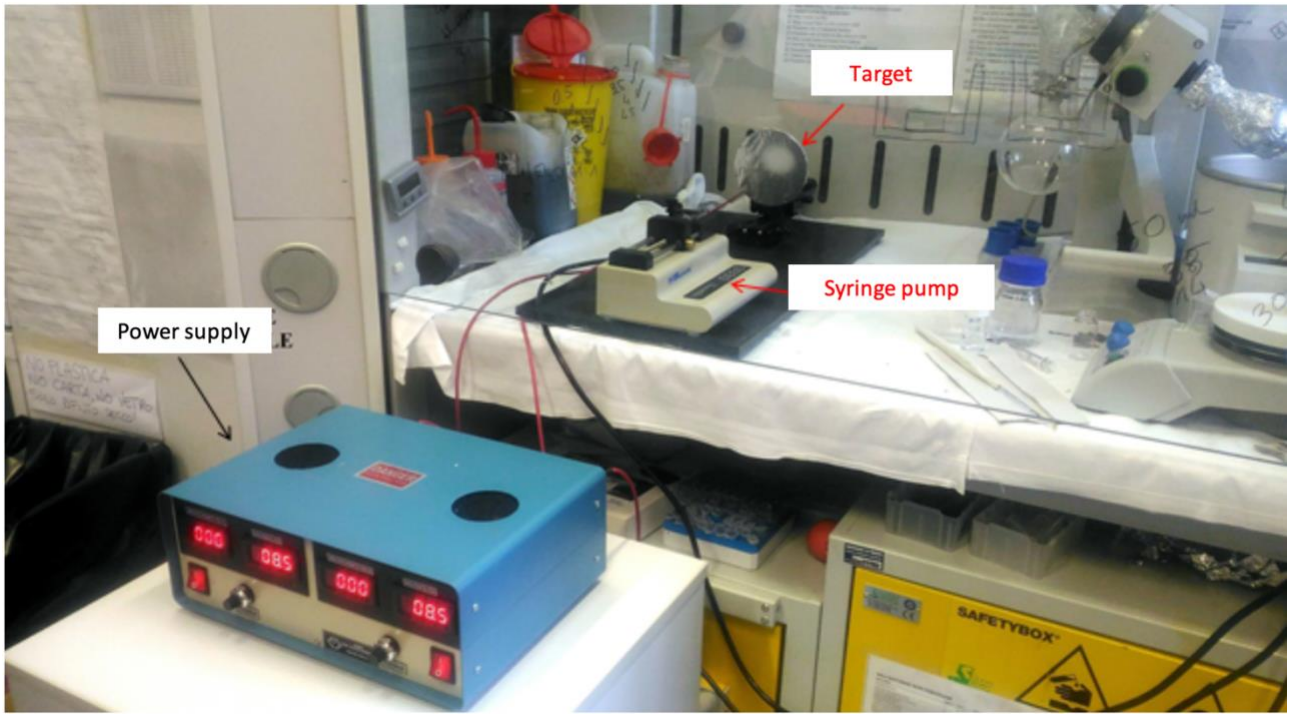

Fig. 7: image of the set-up used during the PCL membrane production experiments. The syringe pump is positioned under chemical hood with regulated air-flow.

Materials

Poly (ε-caprolactone) (PCL, Mw: 80000), organic solvents such as: dichloromethane (DCM), N, N-dimethylformamide (DMF), tetrahydrofuran (THF), chloroform ($CHCl_3$) and methanol (MeOH), the needles and glass syringes were purchased by the company Sigma-Aldrich (USA). The D-ES30PN-20W potential generator used during the experimentation was produced by Gamma High Voltage Research Inc. (Ormond Beach, FL, USA). Finally, the syringe pump was produced by KD Scientific

(Holliston, MA, USA). Silver nitrate ($AgNO_3$), ascorbic acid ($C_6H_8O_6$), LDH (lactate dehydrogenase)-based TOX-7 kit, in-vitro toxicology assay (Resazurin based, Alamar Blue) TOX-8 kit, phosphate buffered saline (PBS), Luria–Bertani (LB) broth, LB Agar and Brain Heart Infusion (BHI) were purchased from Sigma-Aldrich (Chemical Co. USA). Trypsin/EDTA solutions, Fetal Bovine Serum (FBS), penicillin streptomycin 100X, l-glutamine 100X and Dulbecco's modified Eagle's medium (DMEM) were purchased from EuroClone (Milan, Italy). All other chemicals were of analytical grade.

Preparation of PCL solutions

To obtain the polymeric solutions, PCL was solubilized by overnight stirring, in a first step in one of the solvents: THF or DCM. In the second solubilization phase, an additional solvent (DMF) was added. The mixture thus obtained was stirred for at least 30 minutes, in order to allow the mixing of the two solvents.

The target is positioned on a slit which allows the experimenter to adjust the distance between it and the syringe needle. With the same mixture of solvents used and the polymer concentration, the following parameters have been changed: voltage (kV), needle-target distance (cm), flow rate (mL/h) and internal diameter of the needle (G); furthermore, fiber collection time vary from a few seconds (15 s) up to hours, depending on the desired width of the membrane.

Solvents and parameters of PCL solutions for ELS

Once the solutions were obtained, these were loaded into a glass syringe (inner diameter 9 mm), to which a metal needle was applied, whose internal diameter varied according to the desired product. Subsequently, the syringe containing the polymeric solution was placed on the syringe pump, the needle and the target (covered by an aluminium sheet) were connected to the generator of electric potential and, finally, after the ignition of the generator and syringe pump, the procedure was activated. The parameters that have been changed in this experimental phase are reported in the following tables and are:

- Polymer concentration (%)
- Ratio of the solvents used
- Distance between the needle and the fiber collector (cm)
- Electric field intensity (kV)
- Internal diameter of the needle (G)
- Flow rate (mL/h)
- Collector fiber deposition times (T_{ELS})

Each parameters range was selected after a thorough analysis of the recent literature, and varied in order to get the most reproducible nanofiber-based membrane with the fiber diameter in the nanoscale, homogeneity of diameter dimension distribution and pores size, the absence of impurities and defects. The rationale of the parameters combination always arose from the information published in the literature. All these efforts were made to obtain a stable and easy to handle membrane for surgical purposes.

THF/DMF

PCL concentration (%)	Solvent ratio	Needle-collector distance (cm)	Voltage (kV)	Needle gauge (G)	Flow rate (mL/h)	T_{ELS} (min.)
6	1:1	12	15	23	0.4	5
	3:7	15	20	25	0.6	
	7:3	24	27	27	0.8	
					1.0	
					1.5	
					2.0	
8	1:1	15	15	27	1	5
		24				

Tab. 2: the table shows the variation of the experimental parameters performed during the experimental session, aimed at investigating the THF / DMF solvent mixture.

DCM/DMF

PCL concentration (%)	Solvent ratio	Needle-collector distance (cm)	Voltage (kV)	Needle gauge (G)	Flow rate (mL/h)	T_{ELS} (min.)
6	7:3	12	10	23	0.6	5
		24		25	1.0	
8	7:3	24	10	27	0.6	5
			17			
10	7:3	24	10	27	0.6	5
			17			
12	7:3	8	10	23	0.2	5
		16	15	25	0.4	30
		24	17	27	0.6	60
			24		1.0	

Tab. 3: the table shows the variation of the experimental parameters performed during the experimental session, aimed at investigating the mixture of DCM / DMF solvents.

Scanning electron microscope (SEM)

The central part of the obtained samples has been harvested (1 cm^2). This portion was deposited on a carbon double-sided tape, previously placed on an aluminium sample holder (stub). Subsequently, the metallization with gold of the samples was performed using a Sputter Coater K550X (Emitech, Quorum Technologies Ltd, UK). Samples were analyzed with a scanning electron microscope (Quanta 250 SEM, FEI, Oregon, USA). The micrographs were obtained using the secondary electron detector. The working distance was set at 10 mm, to obtain the appropriate magnifications the acceleration voltage was set at 30 kV. At least 10 images were taken for each sample, at different magnifications and in different portions of the sample. The dimensional analysis of the fibers was performed with the help of a plugin, DiameterJ, created for the ImageJ analysis software; DiameterJ is able to analyze an image and calculate the diameter of the nano-microfibers for each pixel present along the fiber axis and produce, as a final result, a series of quantitative data. The average of the fiber diameters and the respective standard deviations obtained with DiameterJ were subsequently processed using Excel 2010 software.

Plasma-air treatment

Thanks to the collaboration with Dr. Denis Scaini of the International School for Advanced Studies of Trieste (SISSA), the PCL membranes were subjected to a plasma-air treatment, in order to increase the hydrophilicity of this polymer. This operation was performed by setting the plasma air at low (6.8 W) and medium (10.5 W) power, for a duration of 5 minutes, using the PDC-32G Plasma Cleaner (Harrick Plasma, Ithaca NY, USA), RF frequency 8-12 MHz.

Contact angle

The wettability test was carried out at room temperature with the aid of an optical microscope (model Leica MZ16) equipped with a digital camera (Leica DFC 320) and a 45° inclined mirror, which allowed to visualize the profile of the liquid drop deposited on the sample. A solution of distilled water was used, to which the Blue Methylene dye 0.05% was added. The drop of water (volume 4 µL) was deposited on the sample in a peripheral position with the aid of an Eppendorf® p10 micropipette. To facilitate the stabilization of the balance between liquid and solid phase, the images were acquired after 30 s from the drop deposition on the surface of the analyzed samples. Pictures have been processed and acquired via Image Pro 3D Suite software and data obtained were further processed using Excel 2010 software. In this test, four samples were analyzed for each type

of membrane: plasma-air-activated PCL membranes, low-power activated plasma-air membranes, activated and CTL-coated membranes and activated membranes coated with CTL-nAg.

CTL production

CTL (lactose modified chitosan) was prepared according to the procedure reported elsewhere starting from highly deacetylated chitosan [90]. The composition of CTL was determined by means of ^{1}H-NMR and resulted to be: glucosamine residue 27 %, N-acetylglucosamine 18 % and 2-(lactit-1-yl)-glucosamine 55 %. The calculated relative MW of CTL is around 1.5×10^{6}.

CTL nAg production

Silver nanoparticles (nAg) were obtained by reducing silver ions with ascorbic acid in CTL solution. Freeze-dried CTL was dissolved in deionized water to obtain a 4 g/L solution. Silver nitrate ($AgNO_3$) was added to CTL at final concentration of 1 mM; then, ascorbic acid was added at final concentrations of 0.5 mM. The solution was kept for 4 hours at room temperature in darkness and then stored at 4 °C.

Computerized micro-tomography (µCT)

In order to evaluate the thickness of the PCL membranes obtained after 30 min and 60 min of fiber deposition on the collector, computed micro-tomographies were obtained by means of a customized cone-beam system called TOMOLAB. The samples were placed on the rotor and the acquisitions were performed with the following parameters: source-sample distance (FSC), 80 mm; distance source-detector (FDS), 250 mm; magnification, 3.1x; binning, 2x2; resolution, 8 µm; dimension of tomographic projections (pixels), 1984x1984; number of tomographic projections, 1440; number of slices, 1332; energy of beam, E = 40 kV; beam intensity, I = 200 µA; exposure time, 1.3 s. The process of reconstruction of the slices and correction of the artefacts deriving from the acquisition of the projections were carried out with the Cobra Exxim software. The Fiji software [91] was used for analysis of scans and measurement of membrane thicknesses.

CTL confocal microscope analysis of adsorption on electrospun PCL membranes

For this experiment, PCL membranes not treated with plasma-air and treated at low and medium power were prepared. These PCL membranes were obtained by applying two different voltages (10 kV and 17 kV). On these membranes, CTL labelled with FITC having a concentration of 2 mg/mL was adsorbed. In a 96-well flat-bottomed plate for tissue culture, 12 samples were placed in the form of

discs, obtained with the help of a circular scalpel (punch) for 6 mm diameter skin biopsies. On each disk a volume of 200 µL of fluorescent CTL (CTL-FITC) was added and allowed to adsorb overnight. The following day, the samples were washed 3 times in distilled water (5 minutes for each wash) and then allowed to dry under a biological hood.

The images of the samples on which the CTL-FITC was adsorbed were acquired with a Nikon Eclipse C1 microscope, with a Nikon Plan Fluor lens (numerical aperture: 2.1, dry) using an argon laser (488 nm) and an acquisition channel at 515-530 nm. The images obtained were analyzed using Fiji software.

FTIR analysis

The polycaprolactone, the CTL, the PCL membranes (obtained by applying a 10 kV and 17 kV voltage) treated with plasma air at low and medium power, on which the CTL was adsorbed were characterized by infrared spectroscopy in transform of Fourier (Nicol ATR model 6700 Thermo Scientific, MI, Italy). The infrared spectrum of the samples was measured in a wave number range of 4000–400 cm^{-1}. All spectra were obtained through the accumulation of 32 scans with a resolution of 4 cm^{-1}.

Raman Analysis

The Raman spectra were obtained using a B & WTek iRaman plus spectrometer, with a 20x objective. A 785 nm laser, whose power was 300 mW, was used as excitation source. For each spectrum 3 accumulations have been acquired, each lasting 5 seconds. The spectra have been corrected and normalized with the baseline.

Electrothermal atomic absorption spectrometry (ETAAS)

The total amount of silver was also determined by electrothermal atomic absorption spectrometry (ETAAS) with Zeeman background correction. A Thermo M AA series spectrometer equipped with a GF95Z graphite furnace and an FS95 furnace autosampler (Thermo Electron Corporation, Cambridge, UK) was used for the analysis. The analyzes were conducted using a calibration curve obtained by dilution (range: 0-10 µg/L) of a silver standard solution (10 µg/mL) for ICP analysis (Sigma-Aldrich, USA). The detection limit (LOD) at the analytical wavelength of 328.1 nm was 0.1 µg/L and the accuracy of the repeatability measurements (RSD%) for the analysis was always less than 5%.

The statistical analysis was performed with the Origin software, verifying that the data followed a normal distribution (Kolmogorov Smirnov test) and that the variances were homogeneous (Levene's test). The data were compared with each other with an ANOVA t-test applying Tukey's post-hoc correction.

Simulated body fluid (SBF) production and membrane dissolution assay

The SBF was prepared by dissolving reagent-grade chemicals of NaCl, $NaHCO_3$, KCl, K_2HPO_4, $MgCl_2{\cdot}6H_2O$, $CaCl_2$, Na_2SO_4 in distilled water and buffering at a pH of 7.40 with tris(hydroxymethyl)aminomethane $(CH_2OH)_3CNH_2$ and 1.0 M HCl at 36.5 °C. The final ion concentrations is nearly equal to those of human blood plasma (Na^+ 142.0, K^+ 5.0, Mg^{2+} 1.5, Ca^{2+} 2.5, Cl^- 147.8, HCO_3^- 4.2, HPO_4^{2-} 1.0, SO_4^{2-} 0.5 mM). Weight variation of membranes was evaluated after 1, 2, 3, 4, 8, 12, 16, 20 weeks of soaking in SBF at 37 °C.

Mechanical testing with DMA

Mechanical resistance of the membrane was tested with uniaxial tensile tests by means of a Dynamic Mechanical Analysis (Electroforce 3300, TA Instruments, 1 59 Lukens Dr, New Castle, DE 19720, US). For the purpose the same membranes used in the dissolution assay, have been cropped in a dog-bone shape thanks to a custom templated produced with a 3D printer (Ultimaker3 Extended). The testing machine mounted a load cell of 22 N with a maximum excursion of deformation of 25 mm. Samples were tested at the constant deformation of 1 mm/min. Maximum strength and strain, or strain and stress at break, and elastic modulus were recorded.

Cell culture and in vitro tests

The line of human osteoblastic cells derived from osteosarcoma (MG63, ATCC number: CRL-1427) was grown in DMEM supplemented with 10% FBS, penicillin 100 U/mL, streptomycin 0.1 mg/mL, L-glutamine 2 mM, at 37° C and with 5% pCO_2. Cells were passed (trypsin 0.25%) twice a week when the confluence level was estimated at about 70-90% of the available culture space.

To carry out cellular in vitro tests on the membranes, these were sectioned into 6 mm diameter disks, with the aid of a sterile punch for biopsies, sterilized under UV light for 30 minutes and placed in 96-well culture plates (Biofil, treated for tissue adhesion).

SEM and cell adhesion and proliferation tests

For cell adhesion and proliferation experiments, 3000 MG63 cells (ATCC number: CRL-1427) were seeded on each sample in 40 µL of DMEM medium supplemented with 10% FBS, penicillin 100 U/mL, streptomycin 0.1 mg/mL, L-glutamine 2 mM, at 37° C and with pCO_2 5%. After 4 hours (to ensure cell adhesion), 200 µL of complete DMEM medium were added to each well. For the SEM analysis 2 disks were prepared for each experimental time and for each type of membrane. At each experimental time interval, the membranes were washed in PBS and fixed for 45 minutes with 4% PFA in PBS. Subsequently, the samples were washed in deionized water and dehydrated with 20-minute steps in ethanol solutions in water with increasing concentration (30%, 50%, 70%, 90%, 100%) and subsequently in solutions of hexamethyldisilazane in ethanol (50% and 100%). After the evaporation of hexamethyldisilazane, the membranes were metallized with gold (Sputter Coater K550X, Emitech, Quorum Technologies Ltd, UK) and analyzed by SEM (Quanta250 SEM, FEI, Oregon, USA) using the secondary electron detector and using an acceleration voltage of 30 kV.

Cell proliferation

Cell proliferation was tested by seeding MG63 cells on membrane surface and analysing their proliferation rate using Alamar Blue™ test at different time points.

For the Alamar Blue™ test 8 disks were prepared for each type of membrane (treated with low-power plasma-air, treated with plasma-air and CTL adsorbed and treated with plasma-air and adsorbed CTL-nAg), of which 2 are been used as white; the samples were placed in a 96-well flat-bottomed culture plate. In each well containing the membrane, 3000 MG63 cells were placed and left for 24 h in a humid atmosphere of 5% CO_2 at 37° C. Adhesion and cell growth were assessed by Alamar Blue™ assay. The tests were performed at 1, 3, 6 and 8 days. At each experimental time point the culture medium was removed and 200 µL of Alamar Blue™ were added to DMEM (10%) for each well. After 4 hours of incubation at 37° C in the dark, 150 µL were taken from each well for fluorescence reading; each well was washed with PBS and 200 µL of medium were subsequently added. Fluorescence reading was performed using a GloMax Multi + Detection System (Promega) spectrofluorimeter using an excitation wavelength of 525 nm and collecting the fluorescence emission in the range 580-640 nm.

The statistical analysis was performed with the Origin software, verifying that the data followed a normal distribution (Kolmogorov Smirnov test) and that the variances were homogeneous (Levene test). The data were compared with each other with an ANOVA test applying Tukey's post-hoc correction.

Cell toxicity

Cell toxicity was tested measuring the lactate dehydrogenase (LDH) released from MG63 cells cultured in the presence of the membranes and in the presence of negative and positive controls of toxicity. In vitro cytotoxicity of PCL-CTL-nAg was evaluated by using lactate dehydrogenase cytotoxicity assay (SIGMA TOX-7LDH assay). UV-sterilized membranes were placed in Dulbecco's modified Eagle's medium, inactivated fetal bovine serum 10 %, penicillin 100 U/mL, streptomycin 100 µg/mL and L-glutamine 2 mM for 24 h. After 24 h of incubation, the cytotoxicity test was performed by direct contact of the cells with the swollen membranes (20 mg per well). Cells were seeded into 24-well plates (30000 cells per well) and incubated 24 hours before the cytotoxicity test. The experiments were performed in triplicate. Cells were than incubated for 24 and 72 hours with membranes. After 24 and 72 hours, the medium was collected and the test was performed following the manufacturer's protocol. The absorbance was measured at 490 nm and 690 nm, with a Tecan Nano Quant Infinite M200 Pro plate reader. The cytotoxicity was calculated using the following equation:

$$\%\ LDH\ release = 100 \times \frac{(A_{490} - A_{690} treated\ cells) - (A_{490} - A_{690} medium)}{(A_{490} - A_{690} cell\ lysate) - (A_{490} - A_{690} medium)}$$

normalizing the values for the total LDH of the control cell lysate.

Polystyrene (PS) was used as a negative control; zinc embedded polyurethane (PU/Zn) membrane and Triton X-100 0.01% in PBS were used as positive control.

Biofilm inhibition

The antibacterial activity of PCL membranes containing silver nanoparticles was tested in terms of biofilm inhibition on Pseudomonas aeruginosa (ATCC 27853) and Staphylococcus aureus ATCC 25923, using an MTT test to assess biofilm viability.

A customized set-up was set up for the biofilm deposition test: test tubes were used, the bottom of which was cut; this allowed to immobilize the membranes (about 1 cm in diameter) by fixing them in the cap of the tube, so as to prevent any bacterial migration in the region of the membrane in close contact with the cap of the tube. The removal of the bottom of the tube allowed the insertion of the bacterial solutions used for the experimentation. For experimentation, plasma-air activated PCL membranes were used, activated by low-power plasma-air and covered by CTL and activated

membranes covered by CTL-nAg; all the membranes used were not deprived of the aluminium sheet used in the production phase by ELS. As a white of bacterial growth, test tubes containing only 10% LB medium were used, without the bacterial strains.

Cells from two different bacterial strains, *Pseudomonas aeruginosa* ATCC 27853 and *Staphylococcus aureus* ATCC 25923 were grown on an LB agar plate and subsequently allowed to grow overnight in 4 mL of LB liquid medium at 37 ° C under agitation (140 rpm). The following day a re-inoculum was performed by taking an aliquot of 200 µL for S. aureus and 400 µL for P. aeruginosa from the initial culture, adding it to 10 mL of new LB medium. The refreshment was left to grow in an incubator for about 1 hour and 30 minutes, in agitation (120 rpm), at 37° C until reaching an optical density (Optical Density - OD) equal to about 0.3 measured at a length d wave of 600 nm. To estimate the bacterial concentration, a predictive model was used, in which at OD equal to 0.3 at a wavelength of 600 nm there are 107 CFU / mL for P. aeruginosa ATCC 27853, while for OD 600 nm equal to 0.1 are present 5 × 107 CFU / mL for S. aureus ATCC 25923. The concentration of bacteria in re-inoculate was then calculated, both of which were then diluted to a final concentration of 106 CFU / ml in diluted LB medium (10% in PBS). For each well containing the samples, 200 µL of diluted bacterial suspension was deposited, except for some samples to which only diluted LB (Luria Bertani) medium was added, for control. The whole was incubated for 72 h at 37° C in a humid atmosphere. At the end of incubation, the exhausted LB medium was removed from the aspiration wells; for the elimination of planktonic cell deposition, two washings were performed with 300 µL of fresh 10% LB, taking care not to touch or disturb the biofilm with the flow and the tip. Then, away from the light, 200 µl of 10% LB medium enriched with 1 mg / mL of MTT (Thiazolyl Blue Tetrazolium Bromide, Sigma-Aldrich) were added. The 24-well flat-bottomed plate was then sealed with the parafilm and covered with aluminium foil to be incubated for 4 h at 37° C in the dark. After incubation, the medium with MTT was removed, and a wash with 300 µL of PBS was performed. The content of the wells was solubilized with 200 µL of lysis solution 20% Sodium Dodecyl Sulfate (SDS, Fluka) in 50% H2O and 50% Dimethylformamide (DMF, Romil). The plate was again sealed with parafilm and aluminium and incubated at 37° C overnight in the dark. Subsequently, 100 µL were taken from each well and deposited in a 96-well microtiter plate with a flat bottom. Then, the absorbance reading was taken at 570 nm with the Nanoquanta infinite instrument M200pro (Tecan).

Results

PCL-based solutions

Two formulations of solvent mixtures were used for the preparation of electrospun PCL membranes. Specifically, Tetrahydrofuran (THF) with N, N-dimethylformamide (DMF) was used based on the work of Nhi *et al.* [92] and dichloromethane (DCM) with DMF referring to the article by Du *et al.* [93].

Here, various parameters have been changed in order to optimize the experimental set-up for the best production of electrospun polymeric membranes. Table 4 summarizes the results of the parameter optimization phase.

Solvents	PCL Concentration (%)	Fibers mean diameters (nm)	Observations
THF/DMF	6	150-275	Beads
	8	200-250	Aggregates, instable solvent
DCM/DMF	6; 8; 10	350-700	Beads and aggregates
	12	500-1900	No defects, homogeneous fiber diameter

Tab. 4: Sum of the results obtained with different parameters of ELS.

The first mixture of solvents taken into consideration for the preparation of PCL membranes involves the use of Tetrahydrofuran (THF) and N, N- dimethylformamide (DMF). The use of this mixture proved to be unpromising from the beginning for the production of PCL nanofibers, since despite the fibers obtained having very small and homogeneous diameters (Fig. 8), in all the tested conditions a complete evaporation of the solvents has never been achieved, with the consequent formation of fibers presenting numerous defects (beads) and aggregates (Fig. 9).

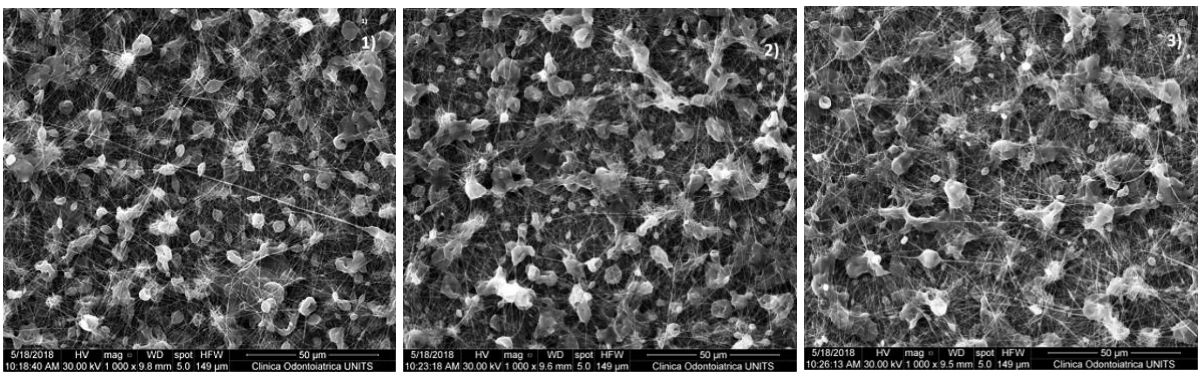

Fig. 8: Images obtained by SEM analysis of PCL nanofibers in 6% THF / DMF 7: 3 with set-up of 24 cm of needle-collector distance, 15 kV, needle 25 G in which the flow was varied rate: 1) 1 mL / h; 2) 1.5 mL / h; 3) 2 mL / h (scale bar: 50 µm).

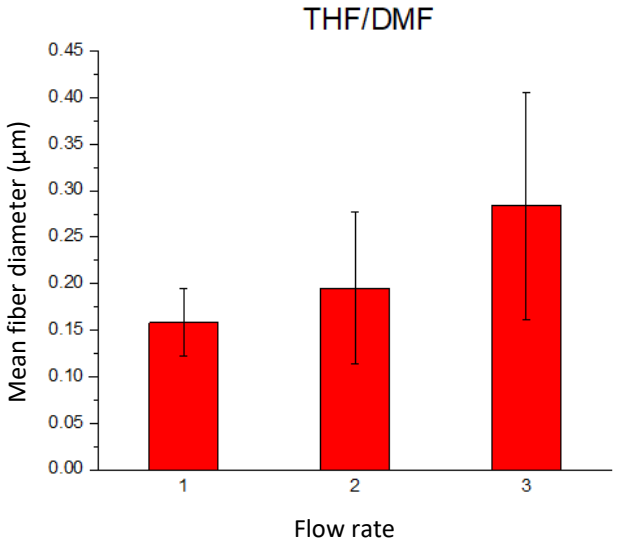

Fig. 9: The average diameters (µm) and the standard deviations of PCL fibers at 6% in THF / DMF 7: 3 are reported, obtained with the following set-up: PCL 6% in THF / DMF 7: 3 with set-up of 24 cm away needle-collector, 15 kV, needle 25 G in which the flow rate has been changed: 1) 1 mL / h; 2) 1.5 mL / h; 3) 2 mL / h

In the attempt to obtain nanofibers without defects and to decrease the average fiber diameter, in the subsequent tests the PCL concentration parameters were changed (8% w / v), the ratio between the two solvents (1:1 ; 3:7 and 7:3), the distance between needle and collector (15 and 24 cm), the flow rate (0.4; 0.6; 0.8; 1; 1.5; 2 mL/h), the voltage (15 kV; 20 kV and 27 kV) and needles used (23 G; 25 G and 27 G). Despite the variation of all the parameters indicated above and the obtainment of nanometric fibers, the obtained membranes also showed numerous beads and defects, probably for the instability of THF used in the realization of such membranes. For this reason, it was considered appropriate to use other types of solvents, in order to obtain a reliable system that is as free of defects as possible.

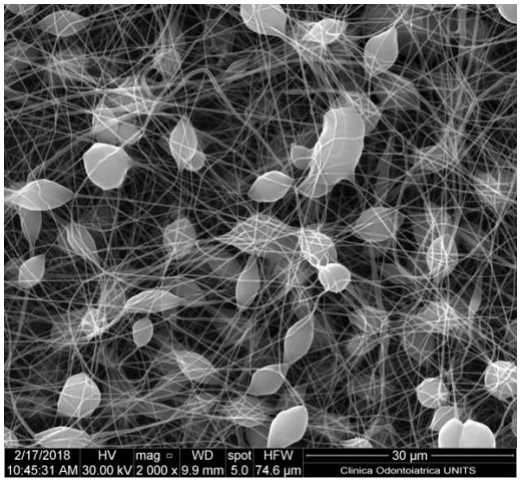

Fig. 10: image obtained by SEM analysis in which PCL fibers are reported at 15% w / v, needle-collector distance 24 cm, voltage 27 kV, needle 21 G and flow rate 10 mL / h (scale bar: 30 µm).

The second solvent mixture used for the preparation of the polymeric membranes used is the dichloromethane (DCM) and the N, N- Dimethylformamide (DMF). The work of Du *et al.* [93] was taken as a reference for this experimental chapter. In this work, the PCL is used with a concentration of 12% w / v with a 7: 3 ratio between the DCM and the DMF, respectively. The initial experimental set-up includes a distance of 24 cm between the needle and the collector, 10 kV of potential and a flow of 0.6 mL/h. At the end of the examination of the experimental options it was possible to conclude that the best experimental set-up for this mixture of solvents is the following: DCM/DMF in 7:3 ratio, PCL at 12% w/v, 24 cm of distance between needle and target, 0.6 mL/h of flow rate, 25G and 27G needles and a voltage in the range, 10 kV to 17 kV. The PCL fibers thus obtained do not have surface defects and expose a rather homogeneous fibrous matrix and this is in agreement with what was obtained in the work of Du *et al.* [93]. At the end of the system optimization phase with the DCM/DMF it emerged that the PCL fibers obtained by applying a voltage of 17 kV exhibited thinner average diameters than the fibers obtained by applying a potential of 10 kV (Fig. 11). Three solutions were prepared (A; B; C) and two tests were carried out for each: the first test was carried out applying a potential of 17 kV, 10 kV for the second. The experimental set-up remained unchanged. Furthermore, from the histogram shown in Figure 12 it can be seen that there is no significant variation in the average diameters of the fibers obtained by electrospinning the three solutions and that therefore a reproducible system can be obtained using these settings.

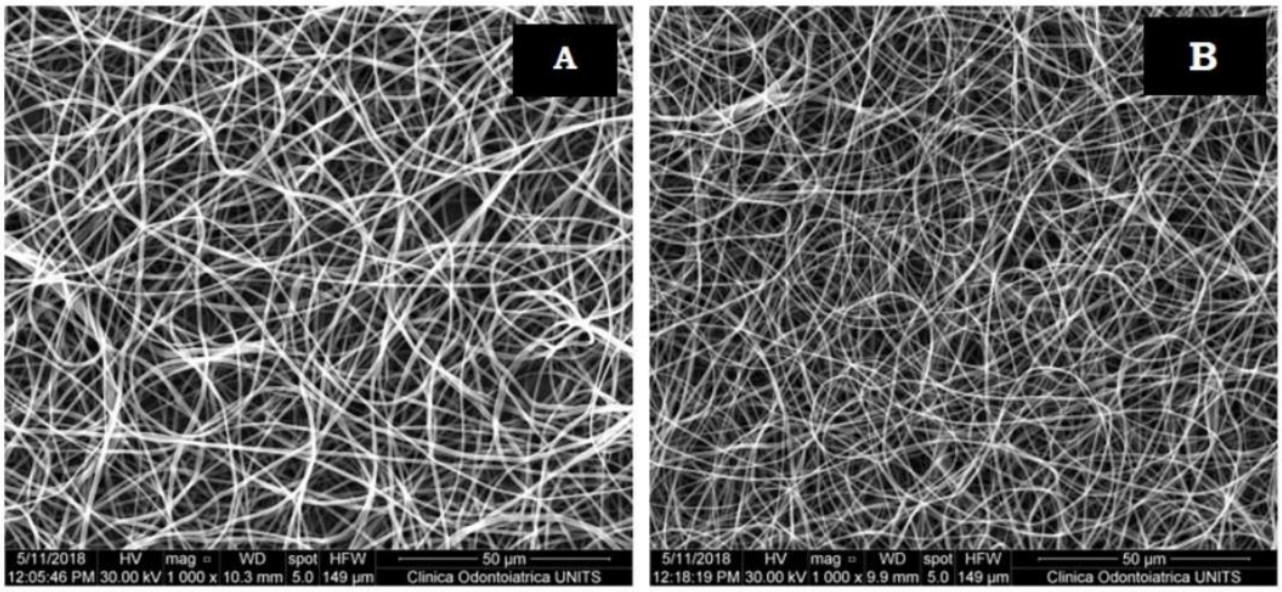

Fig. 11: images obtained by SEM analysis showing the PCL fibers at 12% w / v, needle-collector distance 24 cm, voltage A) 10 kV and B) 17 kV, needle 27 G and flow 0.6 mL / h (scale bar: 50 µm).

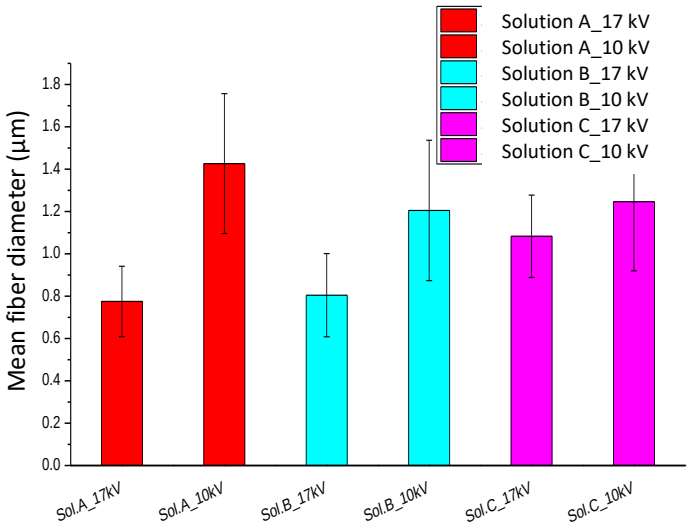

Fig. 12: Histogram showing the average diameters of the three PCL solutions 12% w / v in DCM / DMF in a 7: 3 ratio, needle-collector distance of 24 cm, flow 0.6 mL / h and needle 27G, in which 17 kV and 10 kV are the potentials that have been changed.

µCT examination of PCL membranes

The images obtained by computerized micro-tomography (µCT) and subsequent data processing were carried out with the aim of determining the thickness of the membranes. This information is in fact indispensable especially in view of the mechanical characterization of these membranes. PCL membranes obtained by applying a potential of 10 kV and left to deposit on the collector for 30 minutes were examined, 17 kV electrospun membranes for 30 minutes and membranes obtained

by applying a 17 kV potential and made to deposit on the target for 60 minutes; the differences in terms of thickness between the aforementioned samples are noticeable in Figure 13.

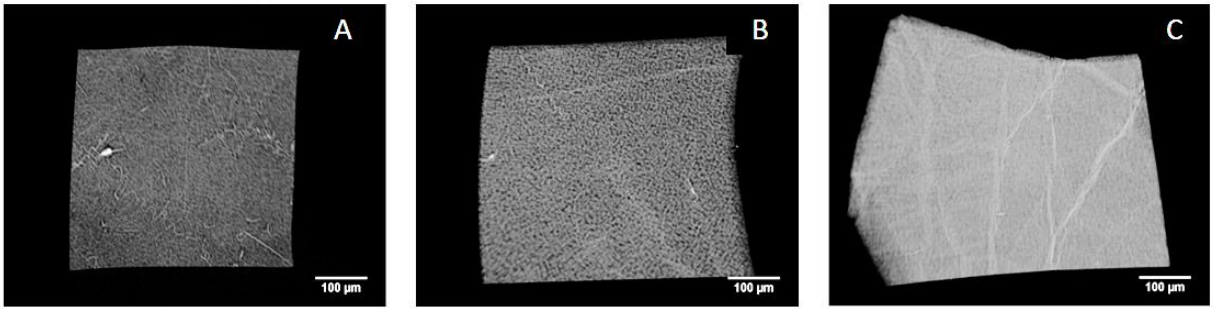

Fig. 13: Image obtained from the investigation using µCT. A) 10 kV electrospun for 30 min, from B) 17 kV deposited for 30 minutes and from C) 17 kV obtained after 60 minutes of deposition (scale bar: 100 µm). The processing of data from the µCT allowed us to quantify the thickness of the membranes (Table 3).

	Thickness (µm)
10 kV 30 min	46.6 ± 3.5
17 kV 30 min	137.3 ± 7.0
17 kv 60 min	215.6 ± 22.1

Tab. 3: average thicknesses of the PCL membranes at 12% w / v, 24 cm of needle-collector distance, 0.6 mL / h, 27G needle and 10 kV potential (electrospun for 30 minutes) and 17 kV (electrospun for 30 min and 60 min), as obtained from µCT analysis.

Comparing the membranes obtained after 30 minutes of deposition of the fibers at 17 kV and 10 kV of potential, it is found that the former have a thickness three times higher than the latter; it is assumed that, most likely, the bundle of fibers obtained by applying a potential of 17 kV was more focused than that of the fibers obtained at 10 kV; in this precise context, this could be explained by the fact that, for the adopted process parameters, 10 kV was too low to allow more focused deposition of the polymeric fibers, with consequent deposition of the same on a larger surface of the collector. With regard to the 17 kV electrospun fibers, the results obtained are in line with what was expected, as the fibers left to deposit on the target for 60 minutes have a thickness almost double than those obtained after 30 minutes of deposition.

Mechanical testing stability of electrospun membranes

Membrane stability was evaluated as weight variation of samples soaked in SBF. The results, reported in Fig. 14, show that membranes are stable over time in terms of weight loss, indeed the slight increase of weight that can be observed is constant and can be ascribed to a retention of liquid after the evaporation.

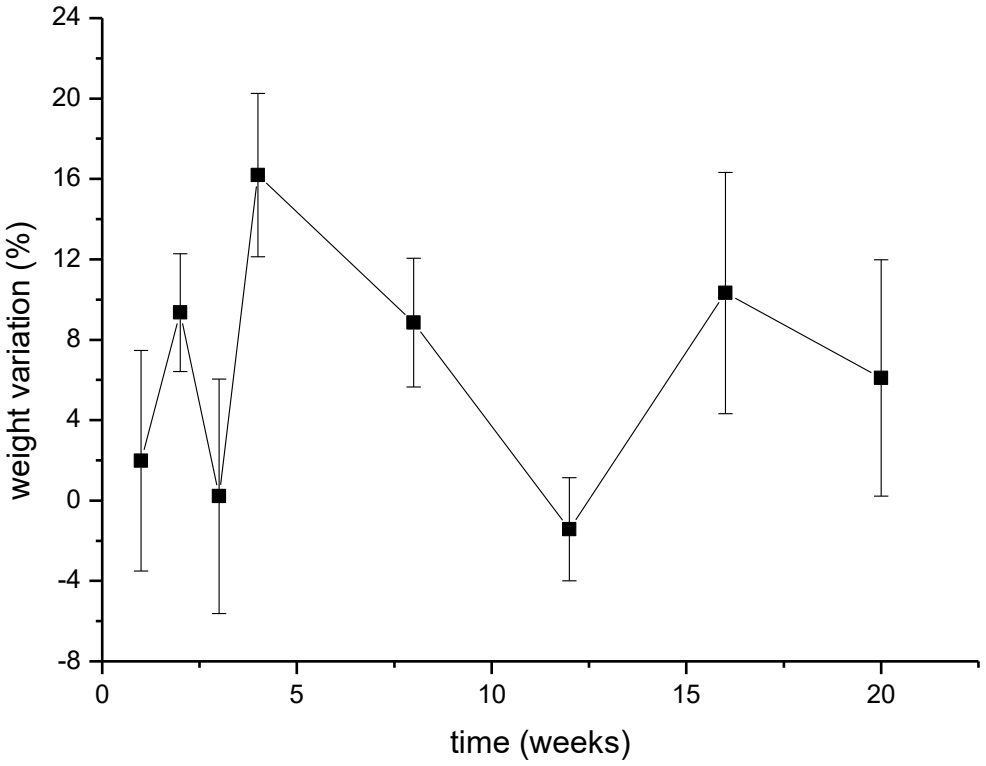

Fig. 14: weight variation graph has been elaborated for both pristine and aged membranes.

Uniaxial tensile tests allowed to evaluate the elasticity (expressed as the Young modulus), and the mechanical resistance of the membranes in terms of maximal strength (stress) and deformation (strain). Young modulus variations (reported in Fig. 15) show a slight decrease over time. The variations can be related to the variability in the electrospinning process and in the nanofiber deposition and organization, indeed the samples for each time point derive from the same membrane.

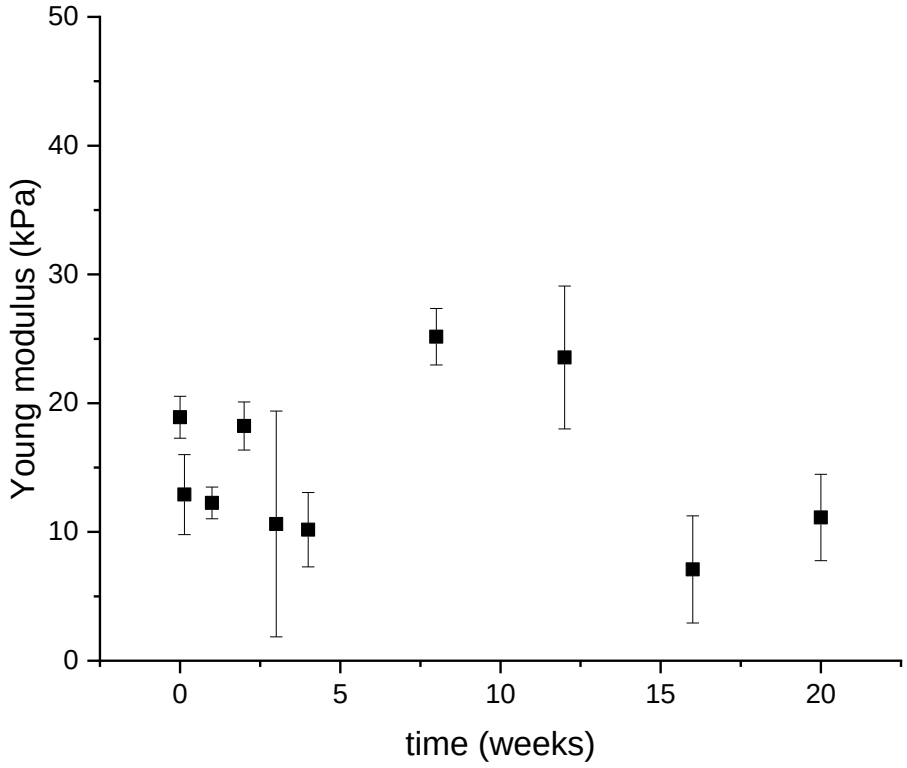

Fig. 15: variation of the membranes Young modulus over time. A slight decrease of the average value can be appreciated.

The evaluation of maximum stress and strain which membrane undergo is limited to the fact that the DMA can apply a maximum displacement of 20 mm. Up to 12 weeks membranes show a good mechanical resistance, indeed they can be deformed for all the displacement allowed by the DMA. As reported in figure 16 the maximum deformation decreases after 12 weeks when the membranes start to break.

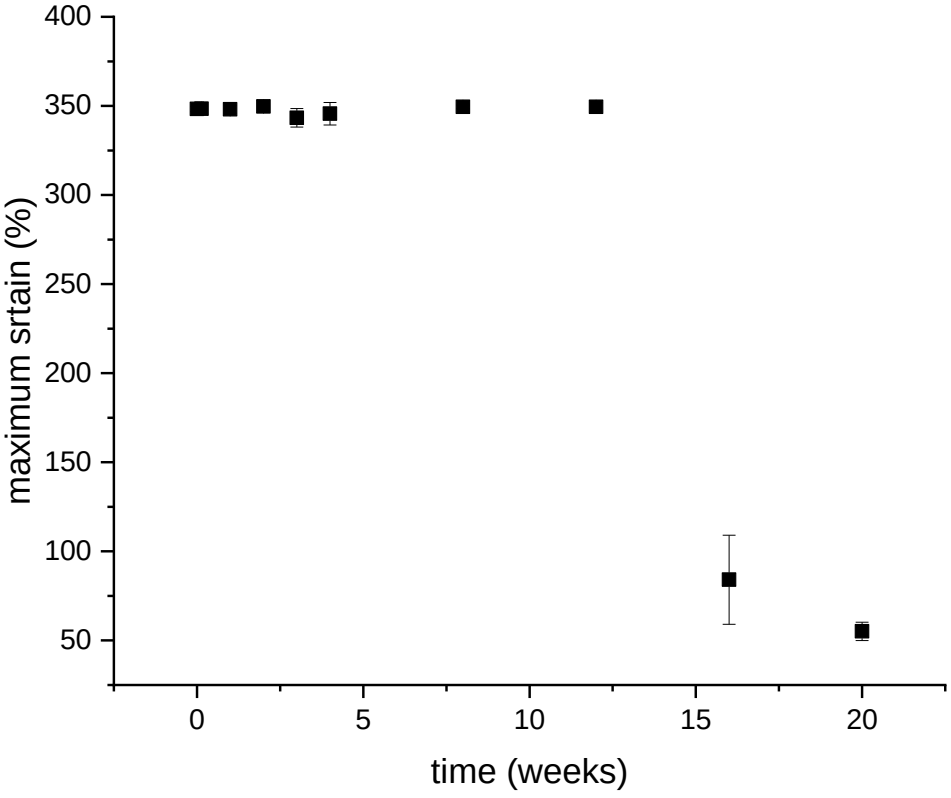

Fig. 16: Variations of the maximum strain over time. A constant behavior can be appreciated during aging until 12 weeks.

As observed for the maximum strain, the maximum stress in almost constant for 12 weeks; the variability of the values up to 12 weeks can be related, as for the Young modulus, to the variability of the electrospinning process.

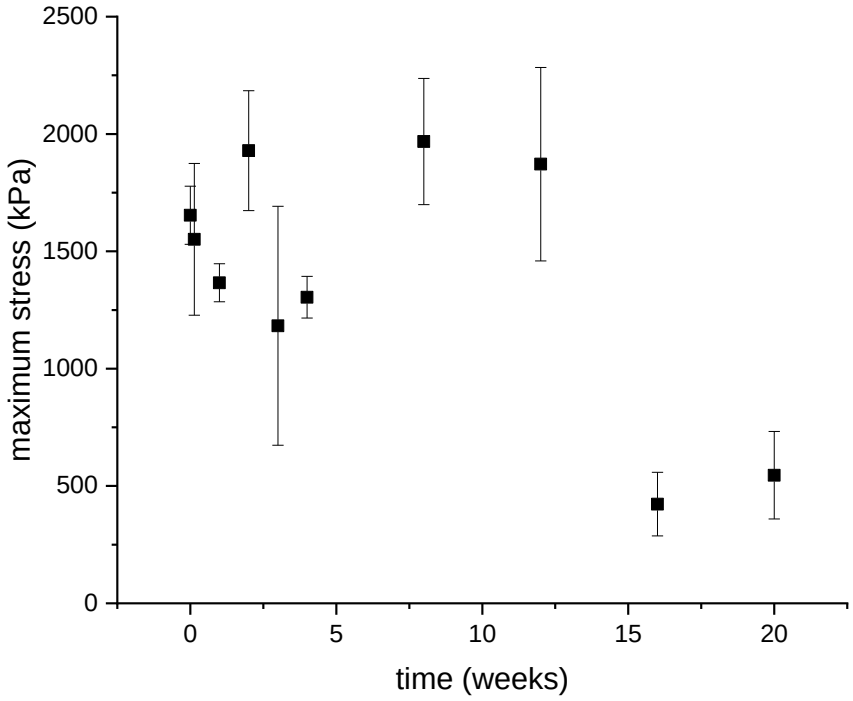

Fig. 17: Variations of the maximum stress over time. A constant behavior can be appreciated during aging until 12 weeks.

All together, these results show that (Fig. 15 and 17) the membranes are stable even after weeks of immersion in SBF. It should be noted that the elasticity slightly decrease over time and that the parameters of maximum stress and maximum deformation change as the membranes break after 16 weeks. This behavior of PCL nanostructured membranes satisfy the mechanical resistance desirable for GBR purposes [47].

CTL e CTL-nAg adsorption on PCL membranes

In the series of experiments and characterization of polymeric fibers, it was possible to evaluate the adsorption of CTL on PCL fibers and how this influences the morphology of the fibers themselves. Furthermore, the effect of low and medium power plasma-air treatment on fiber morphology was evaluated by depositing the samples both in distilled water and in two CTL 2 mg/mL solutions having different pH (pH = 4.5 and pH = 7). The analyzed experimental conditions are reported as follows: membranes prepared at 10 and 17 kV were tested, on which CTL was adsorbed at pH 4.5 or 7, after treatment with low or medium power plasma. Controls were analyzed membranes not treated with plasma or with CTL and membranes treated with plasma and distilled water.

No morphological variation of the fibers was observed by qualitatively comparing the images obtained with the SEM of the membranes produced at the two different voltages (10 kV and 17 kV) not treated with plasma-air and immersed in water or in a CTL solution.

The qualitative considerations were confirmed by the quantitative analysis of the average diameters of the fibers in which no significant variation was shown (Fig. 18).

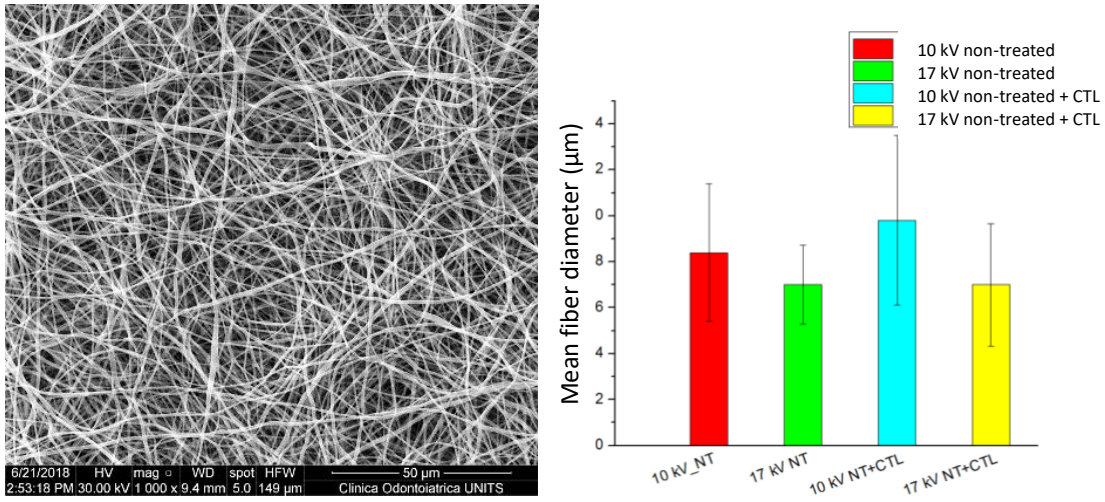

Fig. 18: representative image of a 17 kV electrospun membrane with CTL adsorbed on PCL fibers (left) (scale bar: 50 µm) and histogram showing the average diameters of the PCL at 12% p / v not-treated with plasma air (10kV and 17kV), immersed overnight in water or in a CTL solution (right).

The plasma-air treatment at low and medium power does not alter either the morphology or the average diameter of the PCL fibers (Fig. 19).

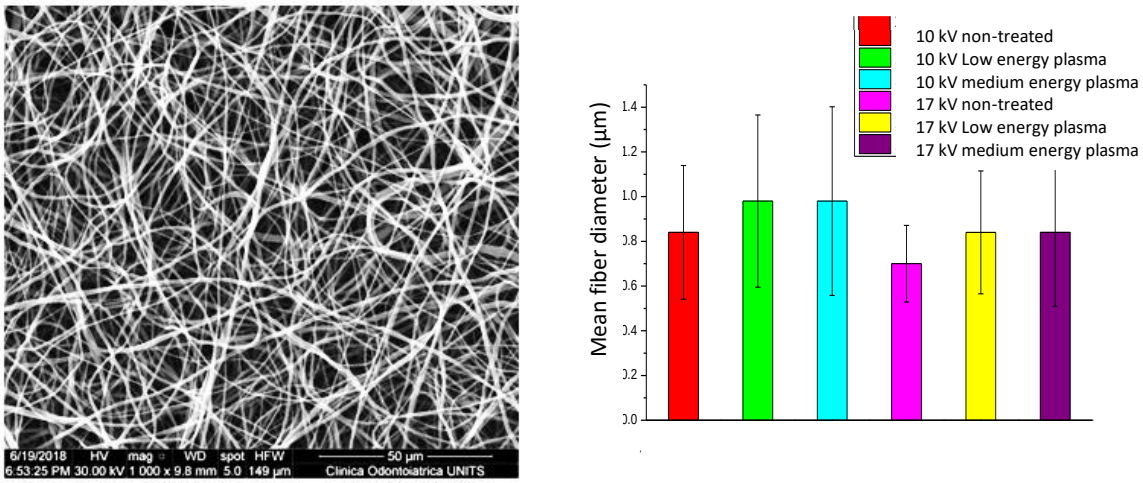

Fig. 19: representative image of PCL membrane 12% p / v electro-wired at 17 kV to which a medium-power plasma-air treatment (left) (scale bar: 50 µm) was applied and histogram showing the

average diameters of the PCL membranes at 12% w / v (10 kV and 17 kV) treated with plasma-air at low and medium power (right).

The PCL 12% w / v membranes (10 kV and 17 kV) treated with low-power plasma-air and placed in water (without CTL adsorption) do not undergo alterations, while the two types of membranes treated with plasma-air at medium power exhibit an altered morphology, in which the fibers are merged with each other; this could be explained by the fact that the medium power treatment weakens the structure of the fibers, which, being more hydrophilic, tend to absorb water and modify accordingly. This behavior could be exploited for the encapsulation of molecules and hydrophilic drugs. Despite the morphological variation of the fibers, the average of the fiber diameters does not show significant changes (Fig. 20).

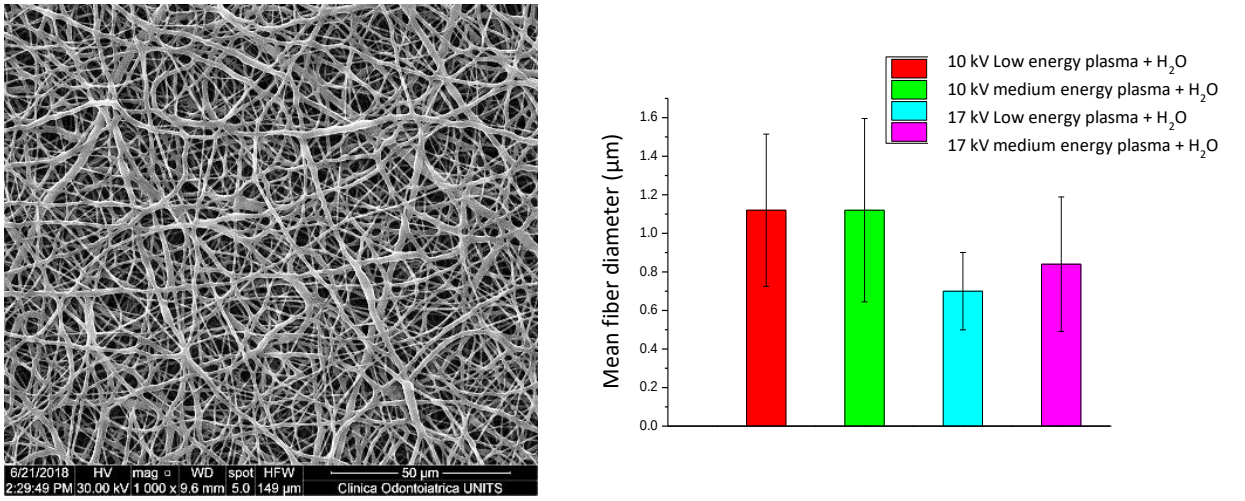

Fig. 20: representative image of PCL membrane 12% p / v electrospun at 17 kV and placed in distilled water to which a medium-power plasma-air treatment (left) (scale bar: 50 µm) and histogram was applied showing the average diameters of PCL membranes at 12% w / v (10 kV and 17 kV) treated with plasma air at low and medium power and placed in distilled water (right).

Finally, the samples obtained were compared with the two different potential intensities (10 kV and 17 kV), treated with low-medium power plasma-air on which the CTL was adsorbed. Both from the qualitative analysis using scanning electron microscopy (SEM) and from the subsequent processing of the data it was verified that the addition of the CTL on these fibers does not alter either the morphology or the average thickness of the diameters (Fig.21).

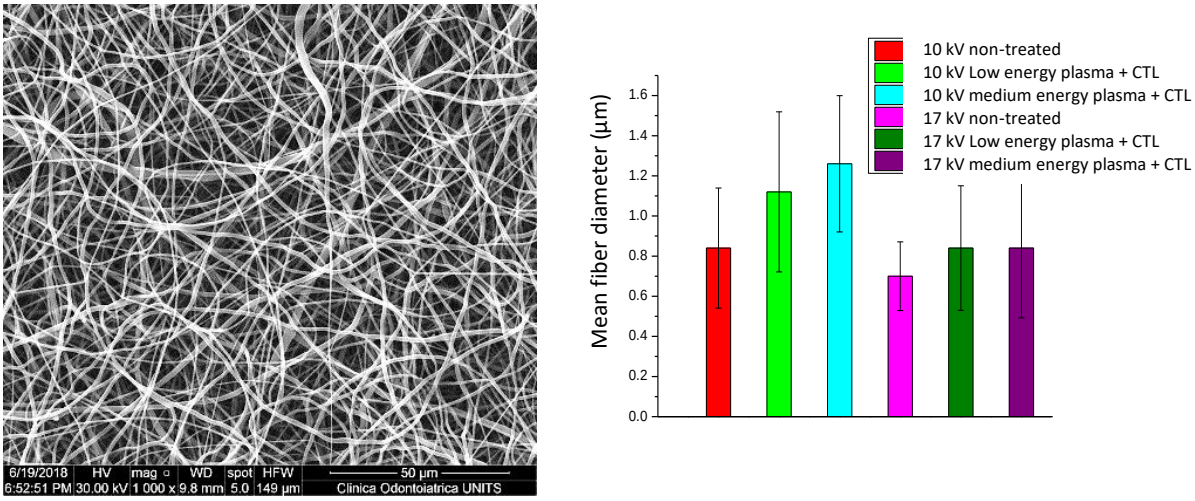

Fig. 21: representative image of PCL membrane 12% p / v electrospun at 17 kV, on which the CTL was adsorbed. A medium-power plasma-air treatment (left) (scale bar: 50 µm) was applied to this membrane. The histogram shows the average diameters of PCL membranes at 12% w / v (10 kV and 17 kV) treated with plasma air at low and medium power and placed in a solution of CTL 2 mg / mL (right).

Confocal microscope assessment of CTL adsorption

The visualization of polymeric membranes by confocal microscopy was used to evaluate the degree of CTL adsorption on PCL fibers. Here, PCL membranes without plasma-air treatment or treated at low and medium power were used. For each type of membrane and condition under examination, two samples were prepared, which were housed in a 96-well flat-bottomed plate and immersed overnight in a 2 mg / mL CTL solution labeled with FITC.

The confocal visualization (Fig. 22) highlighted the importance of plasma-air treatment as regards the adsorption of CTL on polymeric fibers, resulting essential for a homogeneous distribution of polysaccharide on fibers.

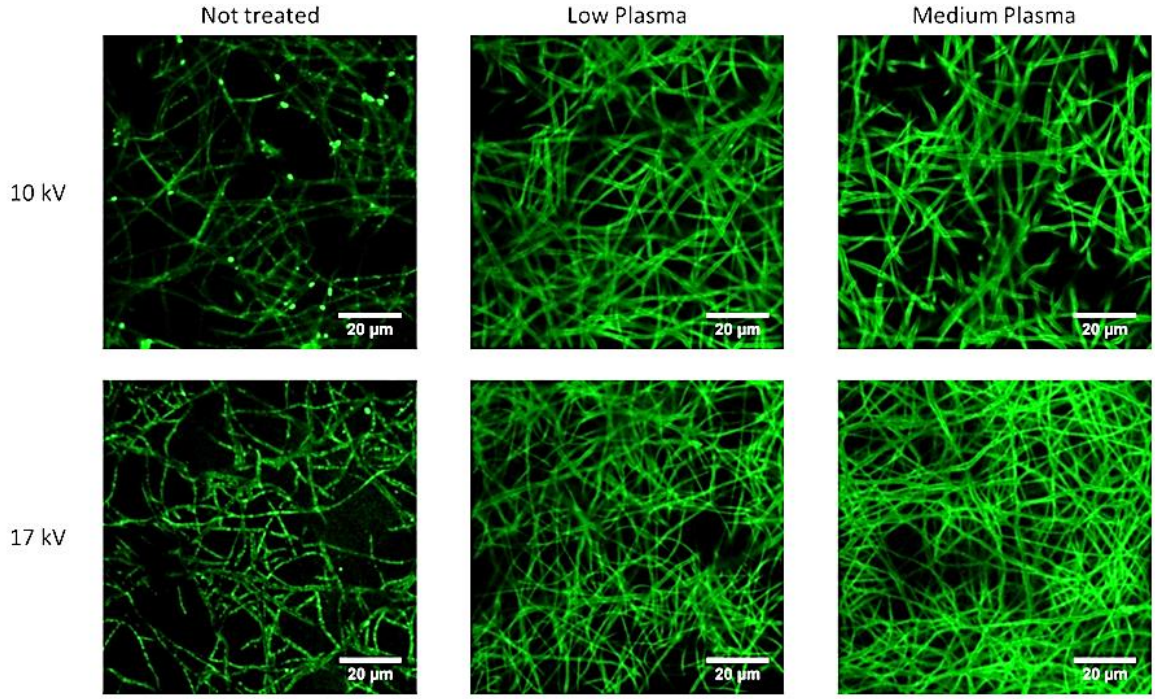

Fig. 22: analysis by confocal microscopy to evaluate the adsorption of CTL-FITC on polymeric membrane fibers without plasma-air treatment and with medium and low power treatment (20 µm scale bar).

FT-IR analysis

The FT-IR analysis was conducted to analyze the adsorption of the modified polysaccharide on PCL fibers. To this end, the PCL and CTL spectra were first identified. The infrared spectra of the PCL membranes on which the CTL was adsorbed (Fig. 23) are difficult to interpret, as they do not report clear bands attributable to the polysaccharide. It has been hypothesized that the reason may lie in the limited adsorption of CTL. Therefore, further investigations are needed, which foresee the use of a method with a larger detection range.

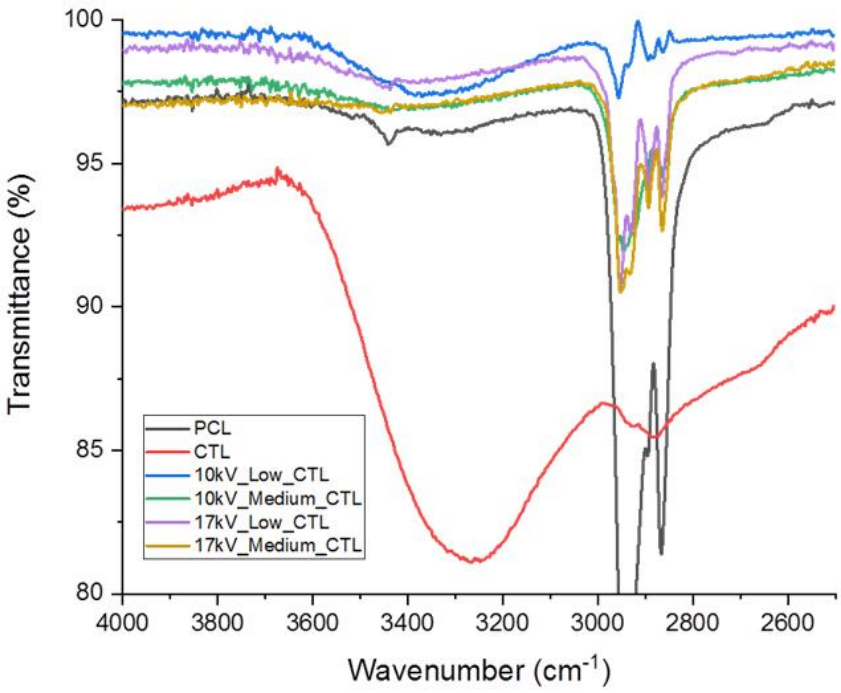

Fig. 23: FT-IR spectrum of PCL (black), CTL (red), electrospun membranes at 10 kV to which a plasma-air low and medium power treatment was applied (blue and green, respectively) together with CTL adsorption; 17 kV membranes to which a plasma-air low and medium power treatment was applied (wisteria and orange, respectively) together with CTL adsorption.

Raman analysis

Raman spectroscopy was used trying to exploit the plasmonic effect of CTL-nAg silver in order to obtain spectra that indicated the occurrence of CTL adsorption on polymeric fibers. Also in this case, the limited concentration of CTL does not allow to visualize the characteristic bands of the polymer. This analysis has brought attention to a 230 cm^{-1} band (Fig. 24), due, presumably, to stretching phenomena of Ag-N and / or Ag-O bonds, indicating the presence of silver and hence the successful adsorption of CTL on the surface of the polymeric membrane. This band is more evident on the PCL membrane activated with low-power plasma-air and put in solution of CTL-nAg 2 mg / mL at pH = 7. This data, in addition to confirming the presence of CTL on the surface of the fibers, highlighted the best conditions for an effective CTL coating obtained on membranes treated with low-power plasma-air under pH conditions equal to 7.

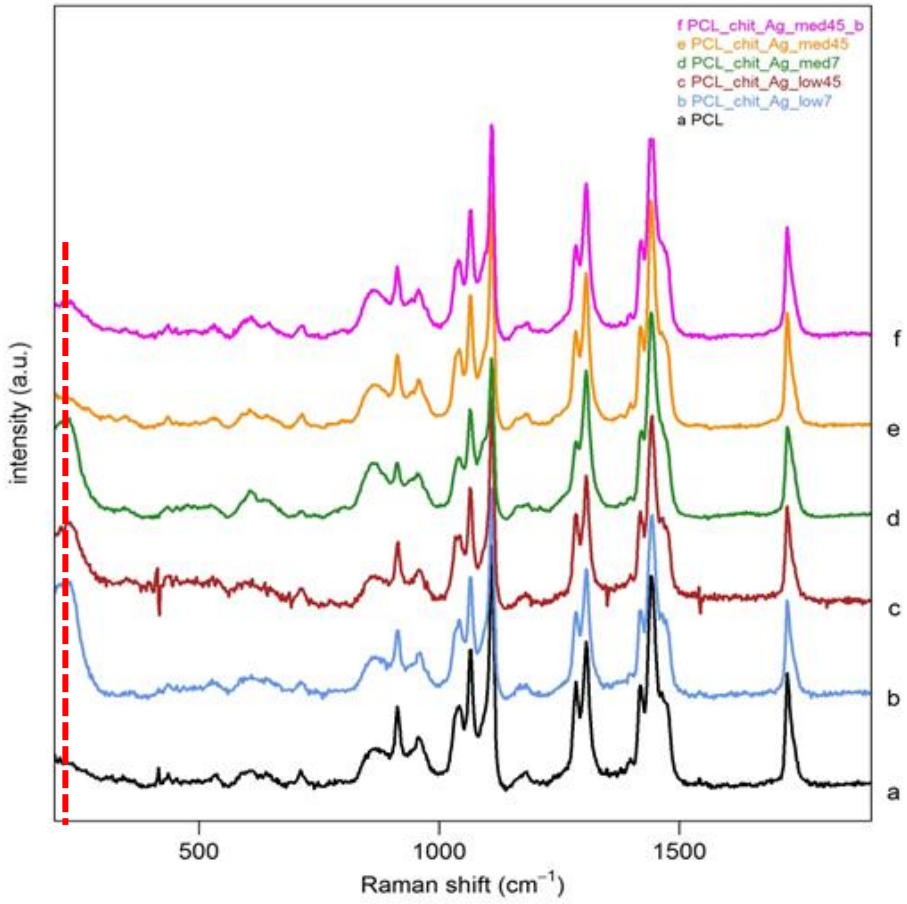

Fig. 24: Raman spectrum of PCL (black) and PCL samples with different plasma-air treatment power on which the CTL-nAg 2 mg / mL was adsorbed in two different pH conditions (pH = 4.5 and pH = 7). The red dotted line indicates the 230 cm-1 band due to Ag-N and / or Ag-O stretching phenomena.

Electrothermal atomic absorption spectrometry (ETAAS)

The total amount of silver present on the PCL membranes contacted with CTL-nAg 2 mg / mL overnight solution was determined thanks to the electrothermal atomic absorption spectrometry (ETAAS). Round-cropped PCL membrane specimens (6 mm in diameter) activated with low-power plasma-air and deposited in CTL-nAg solution at pH = 4.5 and pH = 7 were examined; moreover, activated with medium-power plasma-air deposited in CTL-nAg solution at pH = 4.5 and pH = 7 were assessed. For each type of membrane, four samples were analyzed. From this analysis, emerged that the only statistically significant difference between the samples considered exists for samples treated with medium-power plasma-air and placed in a CTL-nAg solution with pH at 4.5. For these reasons, in subsequent experiments, it was therefore decided to use membranes treated with plasma-air at low power, in order not to apply too aggressive treatments on the samples, which could alter the structure of the fibers and to use CTL / CTL-nAg solutions at pH=7, as pH comparable

to the physiological one, which avoids the solubilization of the silver ions present in the nanoparticles. From the data obtained and reported in Figure 21 it is possible to state that the adsorption of the CTL-nAg occurred in all types of samples and conditions tested.

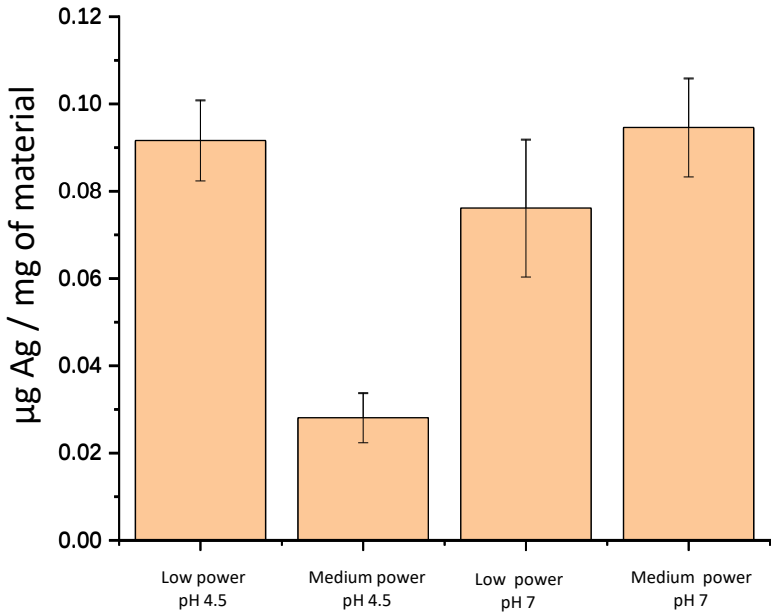

Fig. 25: histogram showing the quantity of silver (µg) for each milligram of material analyzed at different plasma-air treatment power at pH = 4.5 and pH = 7.

PCL, PCL-CTL and PCL-CTL-nAg membrane wettability test through contact angle measurements
Effect of plasma air treatment on contact angle examination

The PCL membranes were activated both with a low-power and medium plasma-air treatment in order to verify whether the alteration of the fibers was a phenomenon independent or not from the power of the treatment. The images shown in Figures 24-25 show that the fibers treated with a low-power plasma-air and immersed in water, although highly hydrophilic do not show alterations with respect to the fibers treated and kept in the dry state. It appears that the treatment applied is sufficient to obtain hydrophilic nanofibers, but does not alter its structure.

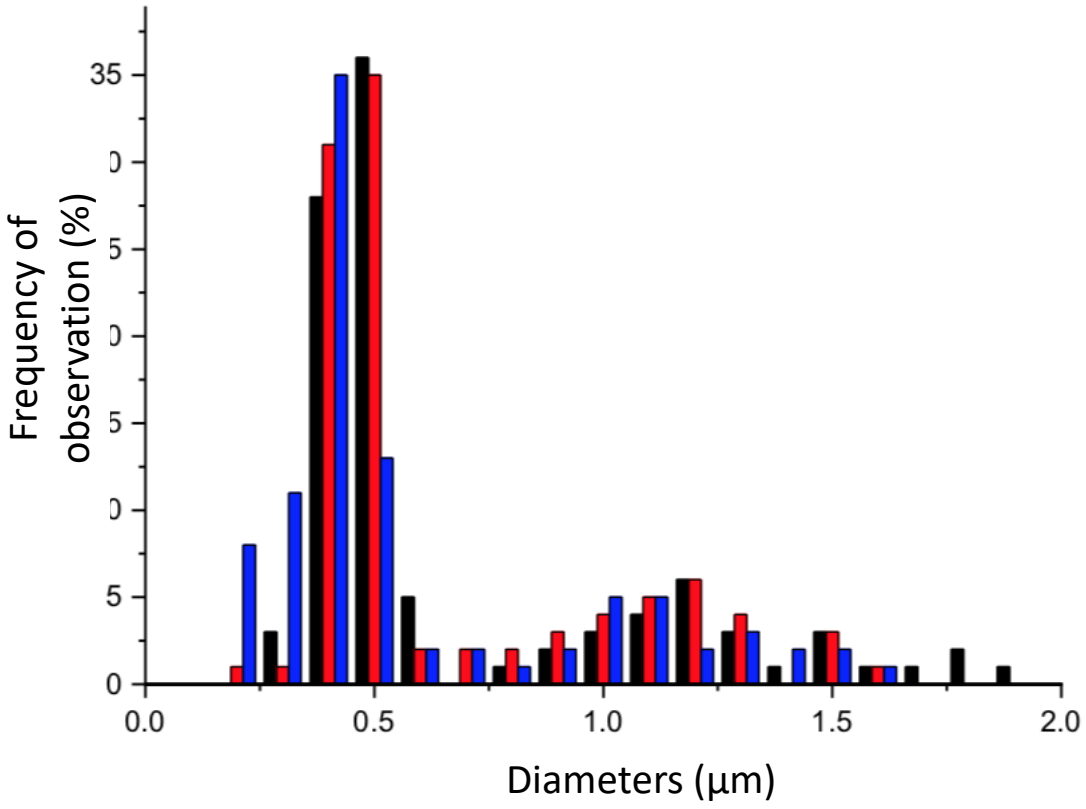

Fig. 26: distribution of PCL nanofiber diameters, obtained with set-up of 0.6 mL / h, 24cm, 10kV, not treated (black), treated with plasma-air (red), treated with plasma-air and then immersed in water (blue). Frequency of observation is intended for percentage of the total.

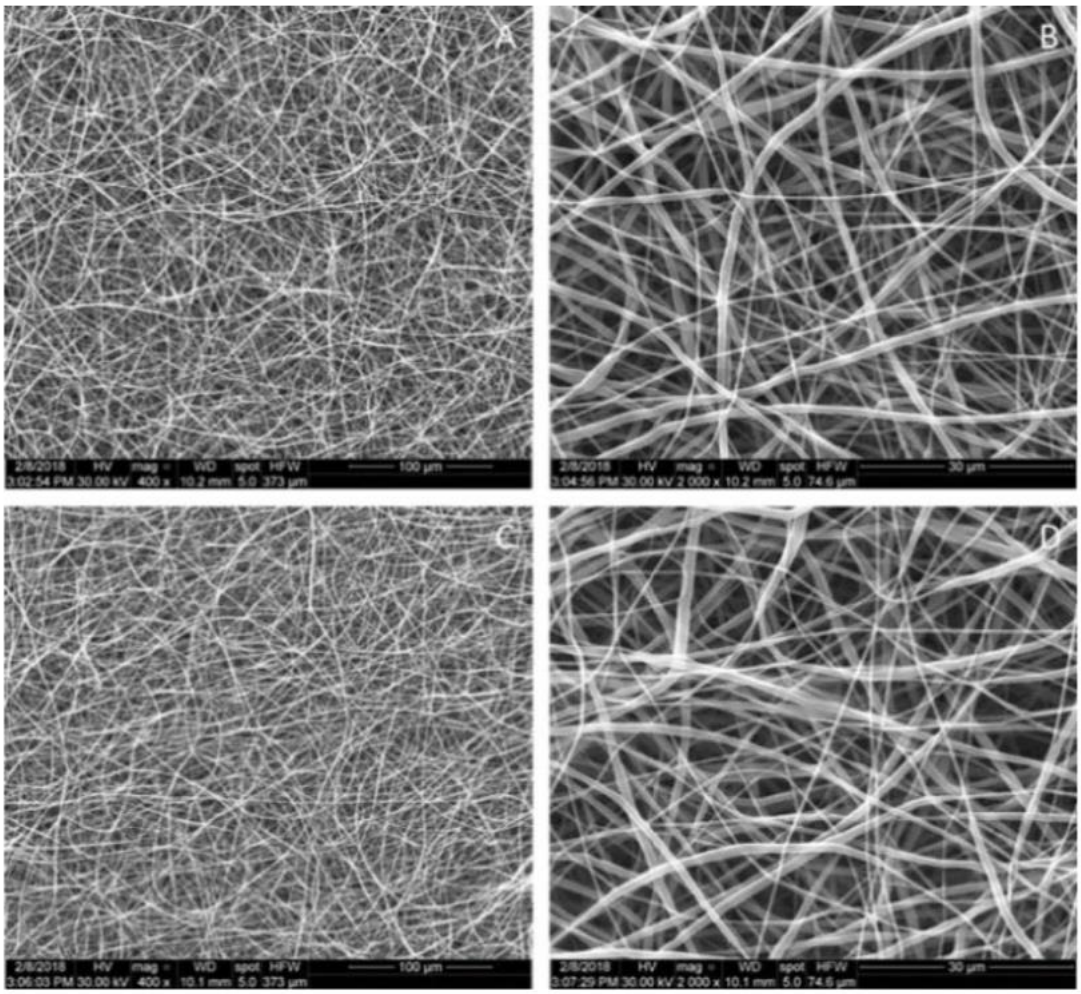

Fig. 27: images obtained by SEM analysis of PCL nanofibers in 12% in DCM / DMF with set-up of 0.6 mL / h, 24cm, 10kV, plasma treated (PCL Plasma Low, AB) and treated with plasma and then stored in water (PCL Plasma Low Water, CD).

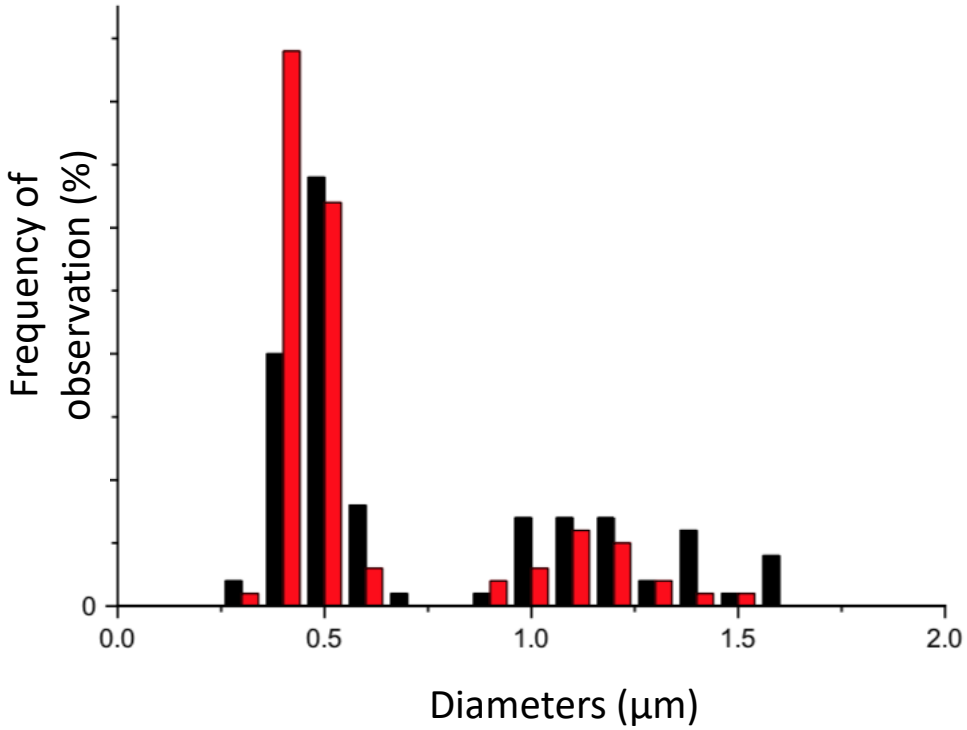

Fig. 28: histogram of the frequency of fiber diameter values obtained with set-up of 0.6 mL / h, 24cm, 10kV, 23G of PCL alone treated with Low plasma (black), PCL treated with Low plasma and then treated with water (red). Frequency of observation is intended for percentage of the total.

The histogram in Figure 28 shows the distribution of the diameters of the nanofibers treated with low-power plasma-air immersed or not in water, and allows to appreciate the minimum variations of the nanofiber diameter distributions between the two samples. For the analysis of the effects of the plasma-air treatment on the hydrophilicity of the membranes contact angle assay was used.

To analyze the effects of plasma-air treatment and the adsorption of the CTL and CTL-nAg on the hydrophilicity of the membranes, contact angle measurements were performed using a stereomicroscope, placing a drop of distilled water (volume 4 µL) on the samples examined and displayed the profile. The images shown in Figure 23 clearly show the marked hydrophilicity of the membranes processed with low-power plasma-air treatment and membranes always treated with plasma-air on which the CTL and CTL-nAg were adsorbed.

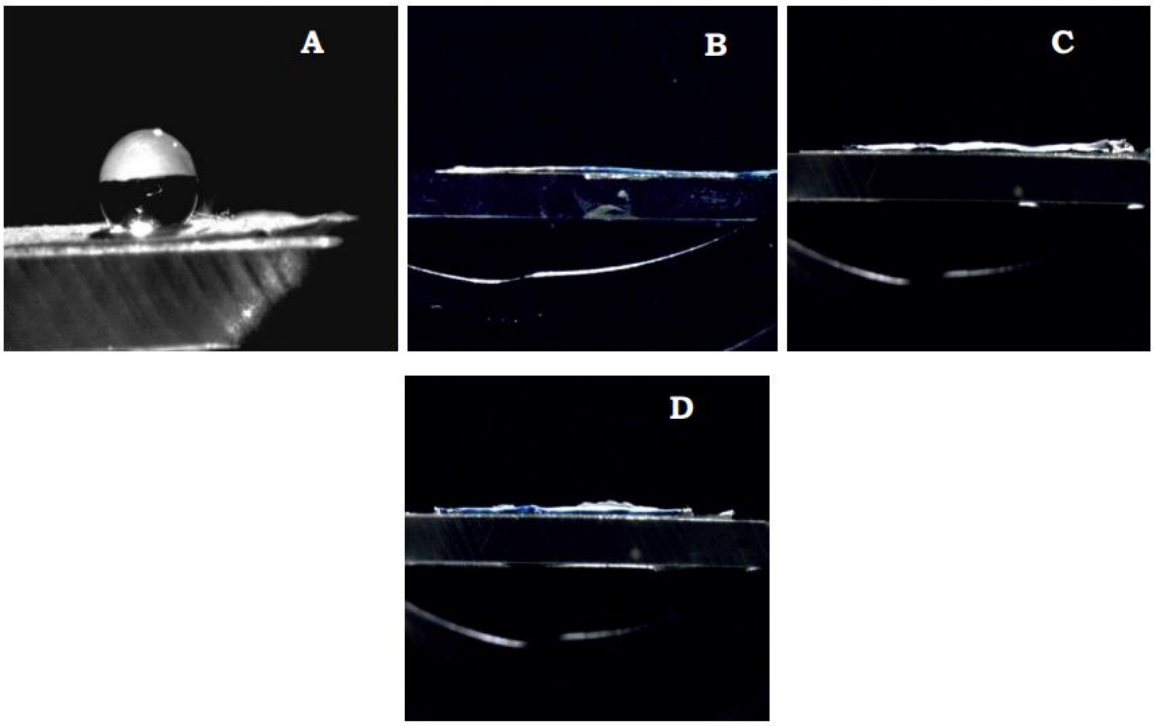

Fig. 29: image showing the profile of the drop deposited on the D membrane samples. Control PCL (A), of membranes treated with low-power plasma-air (B), of treated and coated membranes with CTL (C) and treated and coated membranes with CTL-nAg.

The contact angle values were collected on four samples for each type of membrane, on which two drops of distilled water were deposited. These values are shown in Table 4.

Sample	**Contact angle (°)**
Ctrl (PCL)	128.1 ± 3.5
Low-energy (on PCL)	24.1 ± 4.4
Medium-energy (on PCL)	22.1 ± 5.1
Activated low + CTL	0
Activated low + CTL-nAg	0

Tab. 4: contact angle values, in terms of mean and standard deviation, for each plasma air treated sample.

As previously described, the PCL is a polymer having high hydrophobicity and this is confirmed by the contact angle values reported in Table 4 and by the data present in the literature [94]. Plasma-air membrane activation and CTL and CTL-nAg coating lead to a drastic reduction of the contact

angle. The 0° values reported in Table 4 are nominal, since the high hydrophilicity of the membranes activated with low power air plasma and the activated membranes on which the CTL was adsorbed and the CTL-nAg did not allow the contact angle measurement. Further investigations will be required by performing dynamic contact angle measurements in order to obtain more accurate data. However, obtaining such low contact angle values is partly due to the effect of plasma-air treatment, as confirmed by data in the literature [95][96], but in part could be attributed to an effect of capillarity from the fibers, which allows the infiltration of water into the membrane.

Biofilm deposition assay to test the antimicrobial properties of CTL-nAg

Silver nanoparticles, which possess antimicrobial properties, added to the CTL [97][98] has been used to enhance antimicrobial properties of the produced membranes. In bacterial spp., the thiol groups (-SH) of membrane proteins, which are exposed to the extracellular portion of the membrane, are the main molecular targets of the antimicrobial activity of silver [99][100].

During the experiment, the medium used for the growth of the *Stafiloccocus aureus* and *Pseudomonas aeruginosa* bacterial strains was diluted with PBS since the activity of the silver nanoparticles (Ag-NPs) present in the CTL could have been altered due to high protein concentration in the medium. The bacterial strains of S. aureus and P. aeruginosa were grown in test tubes containing plasma-air not activated membranes, tubes with PCL membranes coated with CTL and tubes with PCL and CTL-nAg membranes.

The preliminary optical density (OD) results obtained allowed to evaluate the deposition of bacterial biofilm. This biofilm, compared to PCL membranes and PCL-CTLs, is almost absent only in the case of membranes in which the CTL-nAg has been adsorbed (CTL-nAg histogram in Figure 26). This preliminary result suggests that these silver nanoparticles confer anti-biofilm activity to the membranes. On the other hand, a high deposition of biofilm at OD 570 nm is observed on the non-activated PCL membranes and the activated PCL-CTLs. It is also noted that, as far as the production of bacterial biofilms is concerned, the membranes in which the nAg-free CTL was adsorbed (CTL histograms in Figure 26) do not give significantly different results from the membranes not activated with plasma-air treatment. These results, therefore, further highlight the need to use antibacterial compounds in association both with polymeric membranes and with those coated with polysaccharides. From the preliminary results obtained from this biofilm deposition assay, a high anti-biofilm activity was found by silver nanoparticles, when compared with the values obtained in untreated membranes and in PCL-CTL membranes and this is confirmed by works reported in the literature that recognize silver as a powerful antimicrobial agent [97][98][101].

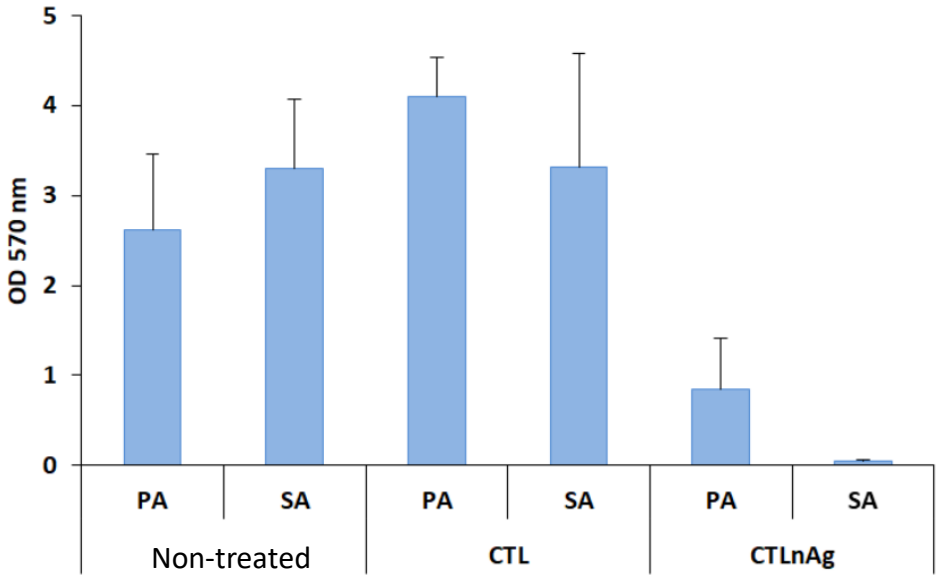

Fig. 30: histogram showing the optical density values at 570 nm obtained during the biofilm deposition assay on PCL-activated plasma membranes, on PCL-CTL membranes and on PCL-CTLnAg membranes. PA= *Pseudomonas aeruginosa;* SA= *Stafiloccocus aureus.*

Alamar Blue™ assay

This test was performed using a human osteosarcoma cell line (MG63) for a period of 8 days. Figure 29 shows that on day 3 the three different types of membranes analyzed show the same proliferation rate, on day 6 there is a slight distancing between the proliferation rate of the membranes with the CTL (PCL-CTL) and the CTL -nAg (PCL-CTLnAg) compared to those of PCL simply activated with plasma-air; while on day 8 a clear superiority of PCL-CTL membranes can be observed compared to the other two types of membranes. The lower proliferative rate at day 8 of PCL-CTLnAg compared to PCL-CTL could be explained by the fact that silver could significantly slow down cell proliferation.

The greatest proliferation rate was observed on activated PCL-CTL membranes, followed by activated PCL-CTLnAg membranes and activated PCL membranes, demonstrating that CTL can confer bioactive properties to the materials with which it is functionalized, in accordance with the work of Donati et al. [90]. The lower rate of PCL-CTLnAg proliferation compared to PCL-CTL is here attributed to a hypothetical slowing down of cell proliferation by nAg, or to a toxic effect of nAg. Additional tests with LDH were conducted to assess toxicity.

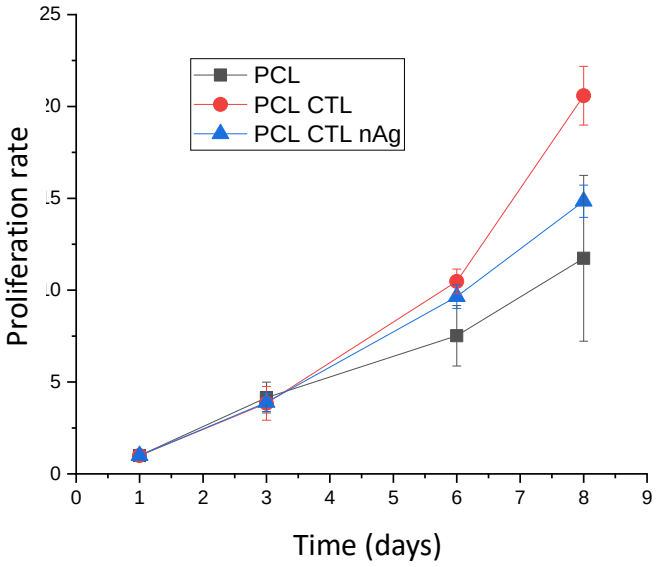

Fig. 31: cell proliferation rate on plasma-air activated PCL membranes (black), PCL-CTL membranes (red) and PCL-CTLnAg membranes (blue) at different time-points.

Figure 27 shows the measurement of fluorescence intensity at the experimental day 1. This data indicates the number of cells adhering on the membranes at the first experimental time. This graph shows how, among the three types of membranes analyzed here, PCL-CTLs can be considered the most suitable from the point of view of cell adhesion.

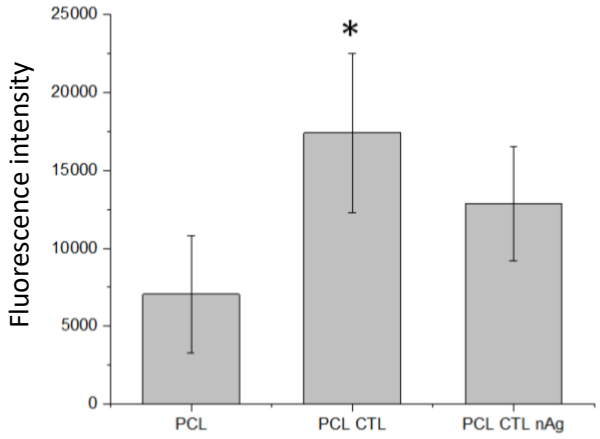

Fig. 32: histogram showing the fluorescence intensity of the three types of membranes analyzed. The asterisk indicates a statistically significant difference in the comparison between groups (T-test, $p < 0.05$).

Cytotoxicity test with LDH

Data reported in the following graph, and the cell density and morphology analyzed with optical microscopy, confirm that the presence of silver nanoparticles is not toxic. Moreover, the released LDH is comparable between Ctrl and PCL, and the possible presence of organic solvent residues can be excluded.

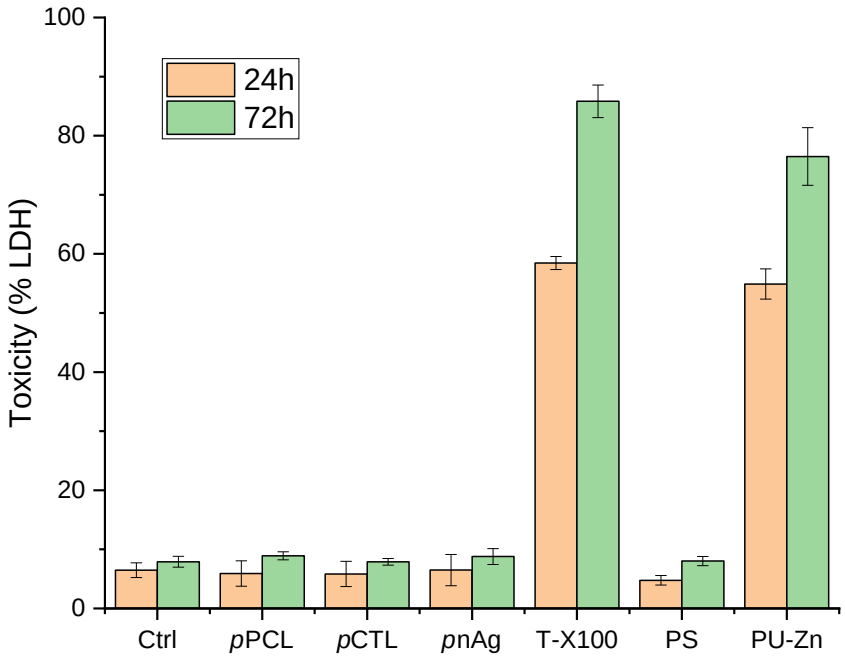

Fig. 33: histogram reporting LDH assay. Non-significant difference in samples containing silver nanoparticles in comparison with negative controls is recorded (as tested with Mann-Whitney U test). The toxicity of positive controls (T-X100 and PU-Zn) is statistically significant with respect to controls and PCL samples (as tested with Mann-Whitney U test)

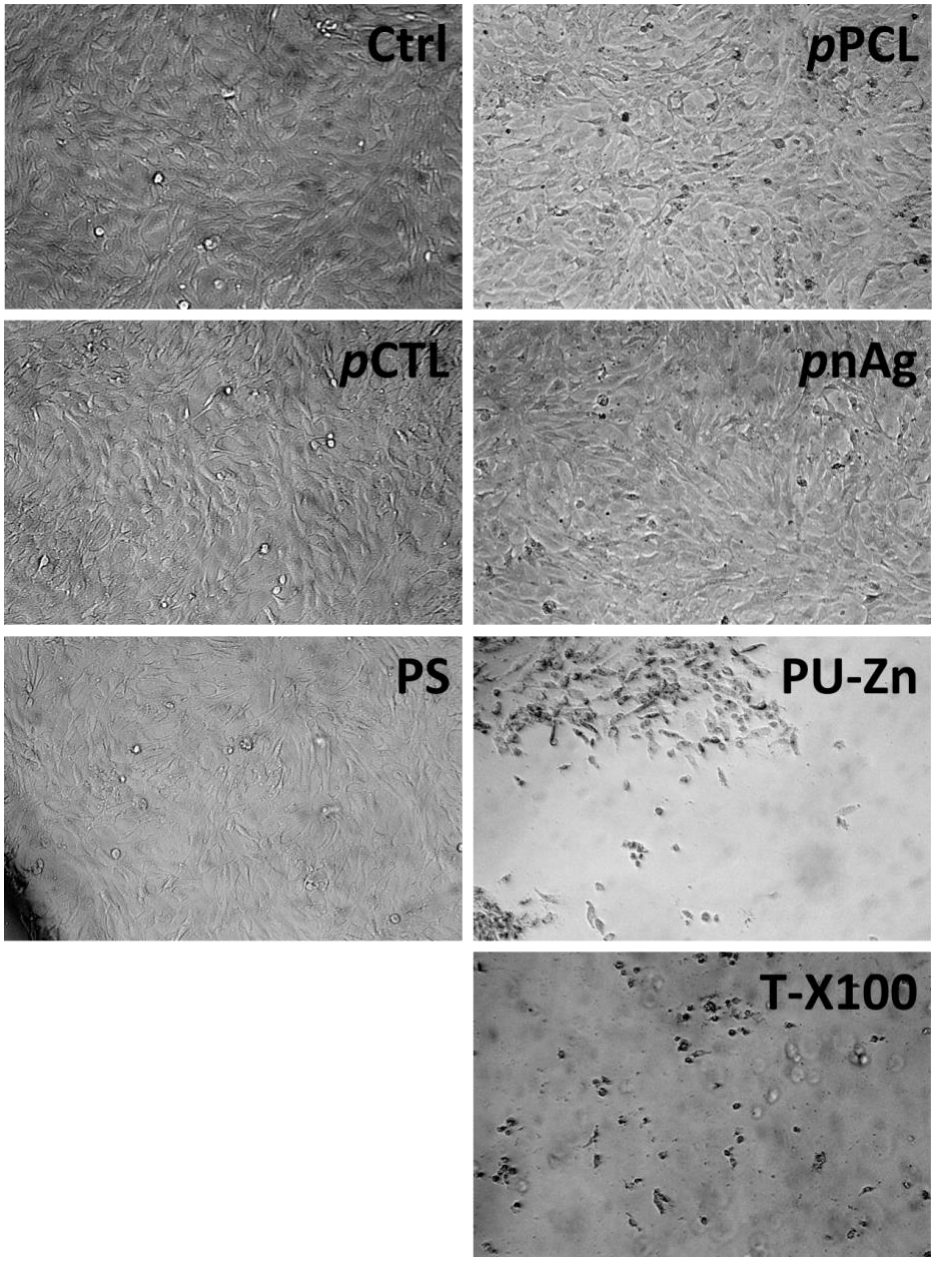

Fig. 34: Evaluation of cell density and morphology at the optical microscope (10X magnification) of cells used for the LDH test, after 72 h. ctrl: Cell culture medium, pPCL: plasma activated membrane, pCTL: CTL coated pPCL, pnAg: CTL coated pPCL, PS: polystirene, negative control, PU-Zn: polyurethane-zinc, positive control, T-X100: Triton X-100 0.01% in PBS, positive control.

SEM analysis of human MG63 osteosarcoma cells grown on electrospun membranes

SEM visualization of fixed and dehydrated membranes was conducted at different incubation times: on days 1 and 8. This technique was chosen in order to highlight the morphology of the cells and their contact with the surface of the membranes. Figure 35 compares qualitatively the different rate of cell proliferation between plasma-air activated PCL membranes, PCL-CTL membranes and PCL-CTL-nAg membranes at different experimental time-points.

After 8 days of incubation, the MG63 cells appear well adherent and diffused on the surface of the three membranes used for the experimentation, in particular on the PCL-CTL membranes and this is in line with the data obtained in the Alamar Blue™ assay (fluorescence intensity and rate of cell proliferation). Similarly, in Figure 31 it is possible to appreciate the elongated shape of the cells in close contact with the surface of the membranes. From these images it can be seen how the substrate realized is highly biocompatible and how it promotes cell adhesion and proliferation and this is in agreement with many works present in the literature, which demonstrate that the membranes obtained by ELS technique possess the potential to promote the adhesion and proliferation of osteoblastic cells in the process of bone regeneration [102][103].

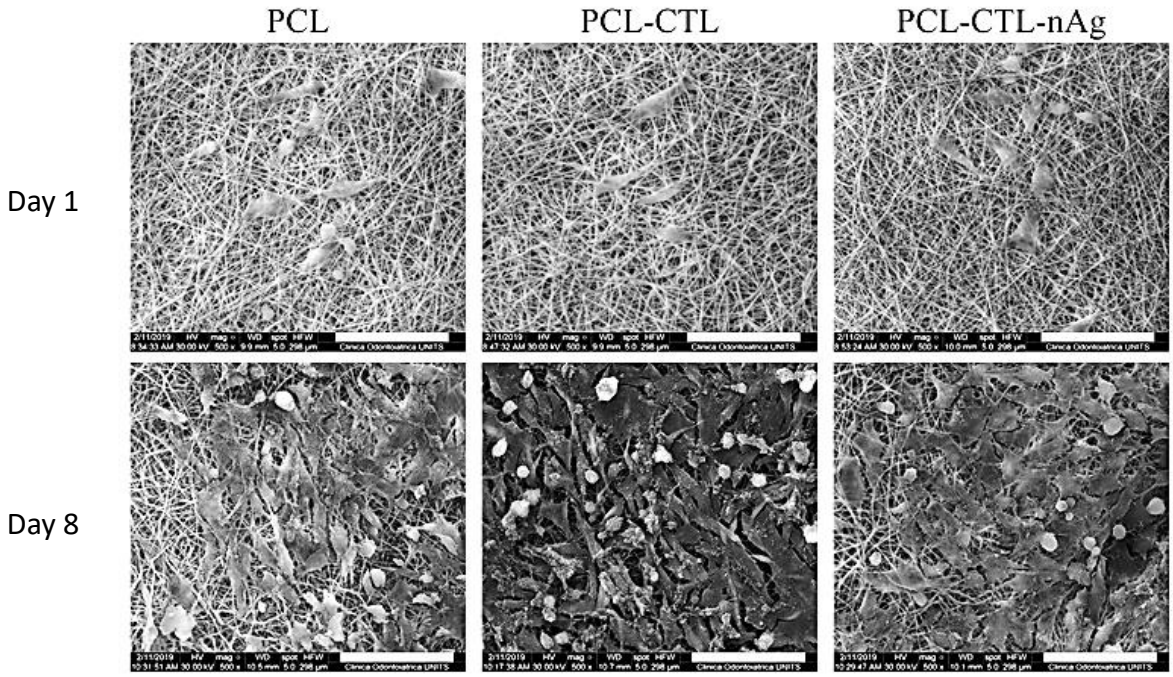

Fig. 35: SEM images of MG63 cells at different experimental time-points (day 1 upper row, day 8 lower row) on plasma-air activated PCL membranes (left), PCL-CTL membranes (center) and PCL-CTLnAg membranes (right) (scale bar: 50 µm).

Chapter 2 Autologous nanofiber-based membranes in bone regeneration: platelet rich fibrin

Actual trends in hemoderivates

Second generation hemoderivatives (*e.g.* PRF) represent nowadays well established resources for accelerated wound healing [104]. One of the most flourishing field of application is regenerative dentistry, in which PRF was demonstrated to have evidence based clinical efficacy in facilitate soft tissue healing [105–107]. Conversely, applications in regenerative dentistry to enhance bone healing remain still a matter of debate [58][108]. PRF fulfils three main criteria of tissue engineering by simultaneously 1) acting as a scaffold containing 2) living cells and 3) growth factors [109].

PRF contains a high concentration of leukocytes, which act to promote local wound healing and fight infection [110]. In the absence of anti-coagulants, PRF forms a 3-dimensional scaffold following 10-12 minutes of centrifugation at 200-700 g force. More recently, lower centrifugation speeds and time have been proposed to further optimize the number of leukocytes and subsequent release of growth factors from PRF formulations [111]. When centrifuged at extremely low g-forces (~60 g for 3 minutes as opposed to 700 g for 12 minutes to produce standard PRF), the blood separates into a plasma-rich supernatant without the use of anti-coagulants. This liquid upper layer is primarily composed of fibrinogen and thrombin that has not yet converted to fibrin. Therefore, prior to fibrin formation, injectable PRF remains in its liquid consistency for approximately 10-15 minutes following centrifugation.

Additional growth factors, cytokines, antibiotics and other regenerative biomolecules have been proposed as combination strategies with liquid-PRF for delivery into host tissues. Actual fields of research for this topic are e.g. the use of PRF as autologous delivery system [112] Liquid PRF is currently being utilized for the local delivery of angiogenic and regenerative growth factors following injections in a similar manner to PRP for the management of various conditions including osteoarthritic knees and rotator cuff tears [113,114].

Material and methods

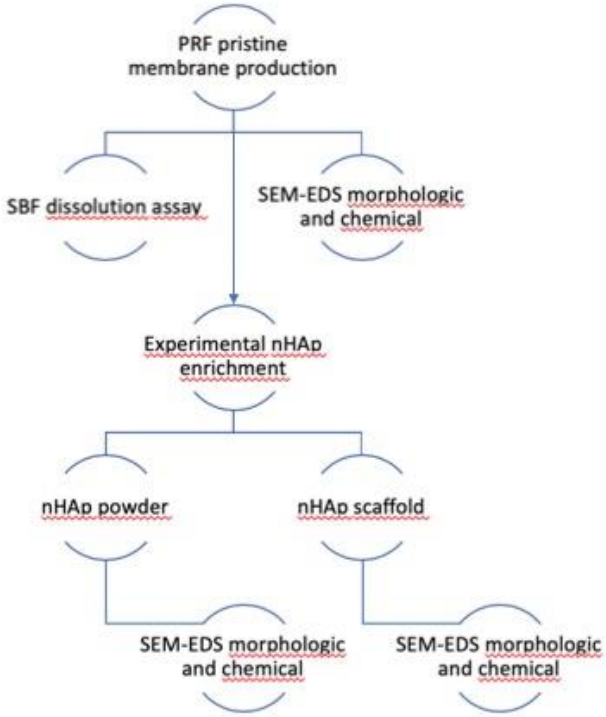

Fig. 37: experimental set-up

Materials

Hydroxyapatite nanopowder, <200 nm particle size (BET), ≥97%, synthetic; Sigma Aldrich, St. Louis, Missouri, US. Plastic dedicated vials of 9ml vacuum preloaded were acquired from IntraSpin by Intra-Lock™ (U.S.A.); the centrifuge was acquired directly by IntraSpin of Intra-Lock™ (U.S.A.); disposable kits for blood sample consisted in butterfly needle (green), a vacuum holder available at our university hospital. The membrane preparation kit (Xpression Fabrication Kit) was acquired by Intra-Lock™ (U.S.A.) and consisted in a metallic box containing one perforated and one flat metallic plate; phosphate buffered saline (PBS), SBF, ethanol, glutaraldehyde, HMDS; LF1060 sodium alginate samples isolated from Laminaria hyperborean were provided by FMC BioPolymer AS (Norway). The relative molar mass ("molecular weight", MW) was found to be 186600 ± 110.

Membrane production

Starting from a simple peripheric venous blood withdrawal inside dedicated tubes from a single healthy donor subject the vials have been immediately centrifuging (within 90 seconds) by IntraSpin by Intra-LockTM centrifuge for 12 minutes at 2700 rpm. The fibrin clots obtained have been

compressed for two minutes using a press supplied with the Xpression Fabrication Kit, in order to obtain membranes with a thickness of 1mm (Fig. 38 and Fig. 39).

Fig. 38: fibrin clot separation after centrifugation phase.

Fig. 39: PRF membranes obtained after two minutes of compression below dedicated press.

Alginate-HAp freeze dried scaffold production

Homogeneous calcium alginate hydrogels gels were prepared by blending the alginate (LF1060) solution (final concentration 2% w/V) with HAp (0.5% w/V) followed by the addition of GDL (60 mM). Only 30% of total HAp was solubilized by GDL (corresponding to a concentration of free calcium 15 mM), leaving a total of 0.35% w/V as solid component. The suspension was degassed prior to the addition of GDL to avoid bubble formation. Alginate/Hydroxyapatite a in mixture hydrogels poured in 9ml plastic tubes were stepwise cooled by immersion in a liquid cryostat (circulating bath 28L, VWR, Radnor, PA, USA), where silicon oil was used as refrigerant fluid. Temperature was decreased stepwise from 20 to -20° C by 5° C steps with 30 min intervals for equilibration, after which samples were freeze-dried (ALPHA 1-2 LD plus freeze-dryer, CHRIST, Osterode am Harz, Germany) for three days to obtain porous scaffolds.

HAp enrichment: first experiment

After blood withdrawal in dedicated 9mL plastic tubes, nHAp was added before centrifugation. Three amounts of nHAp powder (0,1mg; 1mg, 10mg) were added individually to three different tubes. Subsequently the mixture was centrifuged for 12 minutes at 2700 rpm. The vials were opened and the clots were hang with surgical forceps and were separated with surgical scissor from the red phase and the obtained fibrin clots were compressed for two minutes using a press supplied with the Xpression Fabrication Kit, in order to obtain membranes with a thickness of 1mm.

HAp enrichment: second experiment

Membranes were obtained as reported in the previous paragraph.

Different scaffold shapes have been explored in order to reach the best configuration in terms of HAp enrichment of the membranes: long cylindrical with singular axial hole, long cylindrical with multiple diagonally distributed holes, short cylindrical with singular axial hole. All the aforementioned shapes were derived from the produced alginate-HAp freeze dried scaffold. The starting shape was the one obtained from the plastic tube in which the alginate-nHAp was freeze-dried. Then the cylinders were scraped with a 11 blade surgical scalpel. This procedure was adopted to remove the superficial compact layer of the scaffold which could have hampered the blood diffusion within it. Thereafter the cylinders were punctured with an iron-made sharp instrument of 2.5mm of diameter for a single hole along the main axis of the cylinder (option 1); a single hole like the previous, with other multiple holes starting from the surface and reaching the axial hole, randomly executed (option 2); short cylinders obtained cutting a long single-holed long cylinder in four pieces of 1cm of height each (option 3) (Fig. 40).

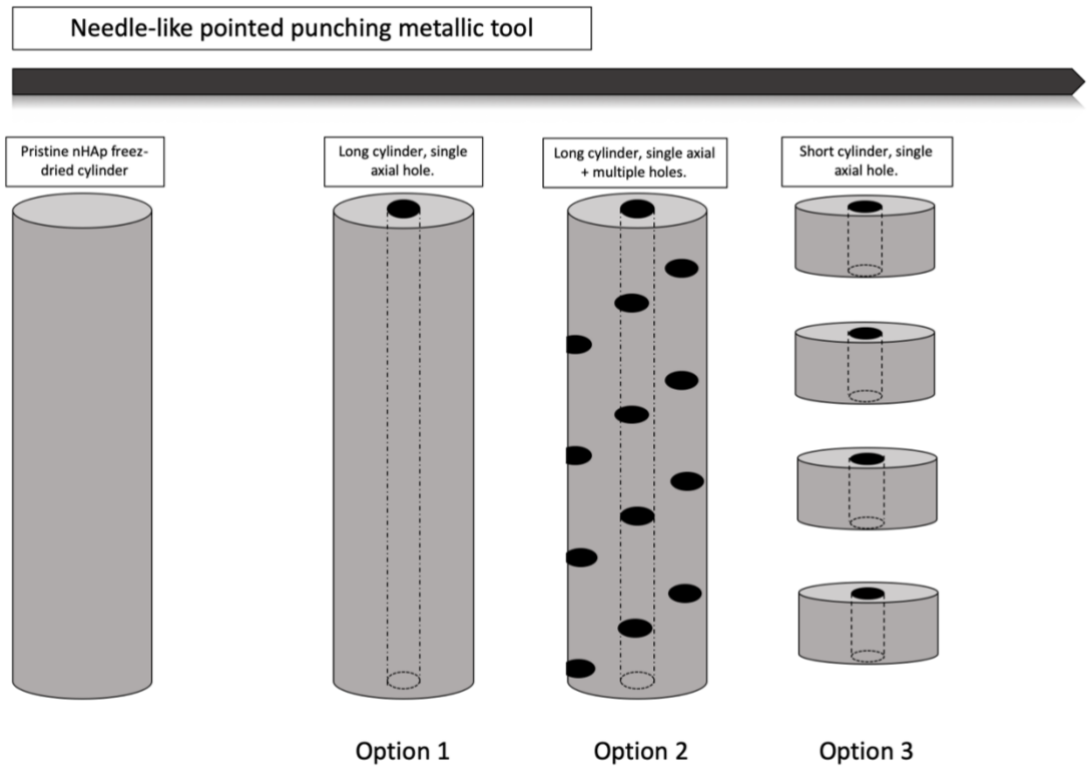

Fig. 40: schematic representation of nHAp scaffold processing for the second experiment.

SEM morphologic analysis

The samples underwent a dehydration process, first with distilled water and ethanol and followed by ethanol and HMDS. The dehydrating scales consisted of leaving punches for half an hour at increasing ethanol concentrations, starting at 20% and growing at 40%, 50%, 70%, 80%, 90% and 100%. The same concentrations were used with the HMDS solution. After two hours, the HMDS solution was eliminated and the punches were left under the hood until they were completely dry. The gold metallization of the samples was performed using a Sputter Coater K550X (Emitech, Quorum Technologies Ltd, UK). When the operation was completed, the samples were analyzed with a scanning electron microscope (Quanta 250 SEM, FEI, Oregon, USA). The micrographs were obtained using the secondary electron detector. The working distance was set at 10 mm, to obtain the appropriate magnifications the acceleration voltage was set at 30 kV. At least 10 images were taken for each sample, at different magnifications and in different portions of the sample. The dimensional analysis of the fibers was performed with the help of a plugin, DiameterJ, created for the ImageJ analysis software; DiameterJ is able to analyze an image and calculate the diameter of the nano-microfibers for each pixel present along the fiber axis and produce, as a final result, a

series of quantitative data. The average of the fiber diameters and the respective standard deviations obtained with DiameterJ were subsequently processed using Excel2010 software.

SEM EDS chemical analysis

Samples were dehydrated as described in the previous paragraph. In order to allow the chemical analysis the samples have been covered with sputtered carbon for EDS analysis.

Mechanical testing with DMA

See detailed description in previous chapter.

Simulated body fluid (SBF) production

See detailed description in previous chapter.

SBF dissolution assay

Evaluation of the in vitro membrane stability was performed with SBF with a pH of 7.40 and ion concentrations nearly equal to those of human blood plasma (Na^+ 142.0, K^+ 5.0, Mg^2+ 1.5, Ca^{2+} 2.5, Cl− 147.8, HCO_3^- 4.2, HPO_4^{2-} 1.0, SO_4^{2-} 0.5 mM). Every obtained membrane was punched with a 8mm circular punch in two different parts of the membrane: one closer to the red phase called “tail” and one closer to the top called “head” in order to investigate a possible different behaviour of the samples according to the distribution of the fibrin fibers, leukocytes and platelets. In each well 2 mL of sterile SBF solution were prepared to accommodate the membranes. Throughout the experiment, the punches were stored in an incubator at a constant temperature of 37° C to recreate an environment similar to that found in the oral cavity. Every 24 h the membranes, hold in a metallic customized weighted grind, have been weighted with an analytical balance (AND HR-120, A&D Instruments LTD, Oxfordshire, UK) and the SBF has been substituted for every time point till the complete dissolution of the sample.

Results

SEM morphologic analysis of pristine PRF membranes

SEM analysis of pristine PRF membranes after centrifugation (2700 rpm for 12 minutes) of entire blood sample resulted in nanometric homogenously and randomly distributed fibrin fibers. In isolated field of the samples analyzed, red blood cells and platelets have been observed (Fig. 37 and 39).

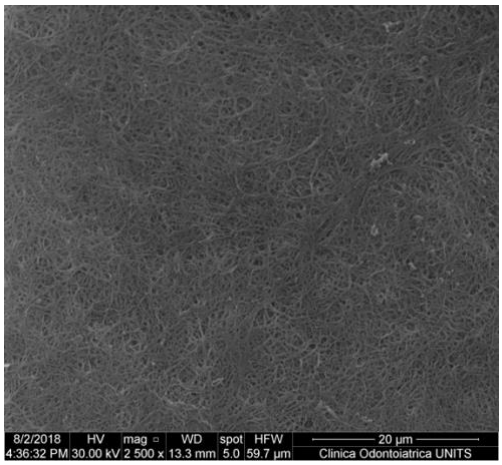

Fig. 37: shows a pristine PRF membrane. See the randomly distributed fibrin fibers. SEM microscope, 2500x magnification. pristine PRF membrane under 2500x magnification SEM microscope (Scale bar 20 µm).

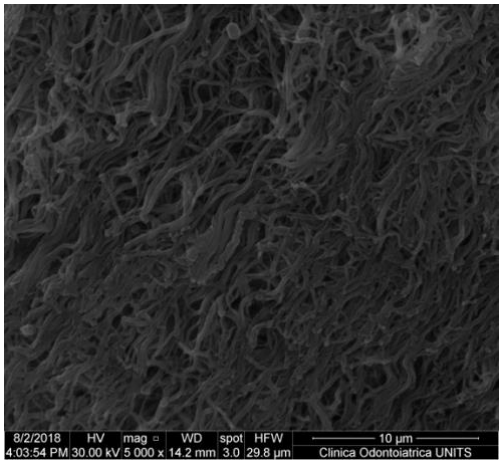

Fig. 38: pristine PRF membrane under 5000x magnification SEM microscope (Scale bar 10 µm). Woven morphology of the fibers appear with the same diameter distribution.

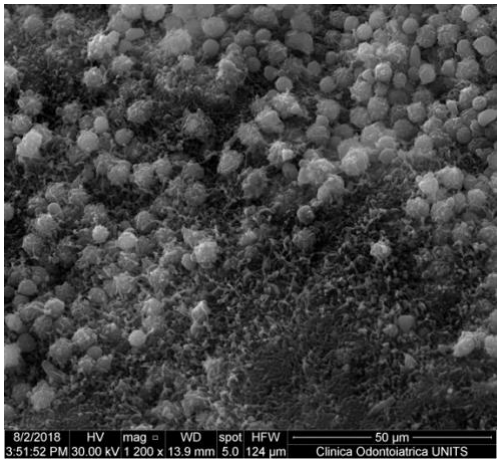

Fig. 39: pristine PRF membrane under 2500x magnification SEM microscope (Scale bar 20 µm). Red blood cells on the membrane's surface can be observed.

SBF dissolution assay

8 vials of blood were harvested from a single subject. The centrifugation took place immediately, at 2700 rpm for 12 minutes by Intra-LockTM centrifuge (Fig. 40 and 44).

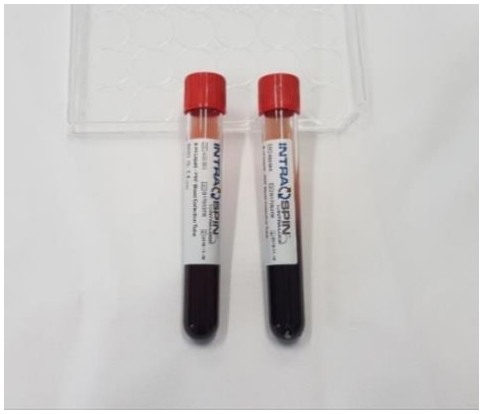

Fig. 40: plastic tubes with entire blood after centrifugation (2700 rpm for 12 minutes).

After centrifugation the fibrin clot was separated with sharp sterile surgical scissors and deposit on the grid of the Xpression kit™ (Fig. 40). The pores of the grid allow the passage of serum, thus the thinning of the clot after compression.

Fig. 41: fibrin clot after separation from red blood cell phase.

Subsequently, the stainless steel plate of the kit was laid upon the grid for 2 minutes to let the weight of the plate compress the clots to eliminate serum, thus compacting the clots and generating the membranes.

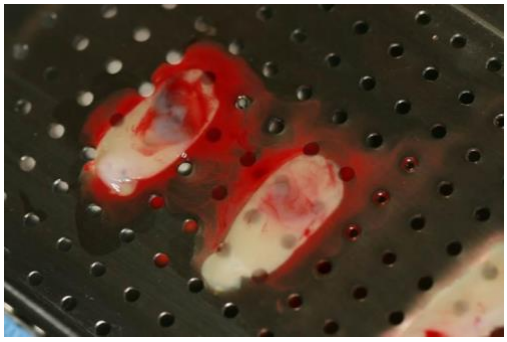

Fig. 42: PRF membranes after compression for 2 minutes.

After compression, the obtained membranes were cropped with a sterile punch scalpel to obtain the samples used in the experiment.

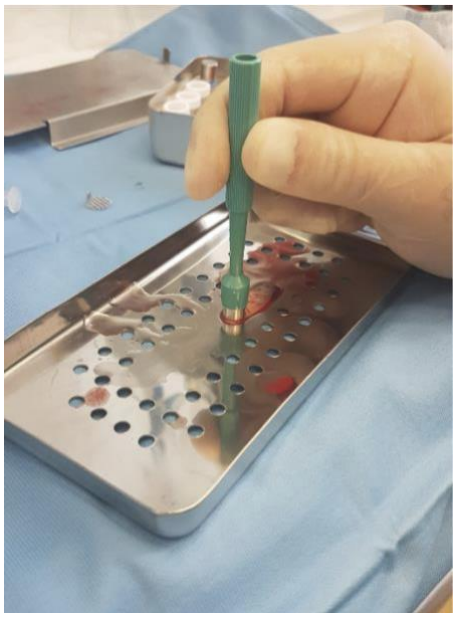

Fig. 43: PRF membranes cropping with 8mm round punch.

The cropped membranes were inserted in a 24-multi-well containing a customized sterile metal grid and 2ml of SBF each.

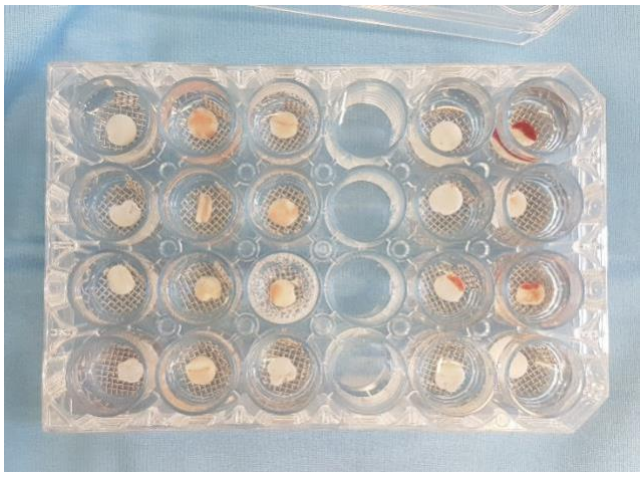

Fig. 44: PRF membranes cropped and immersed in 2ml of SBF in 24-multi-well laid on a custom round metallic grid.

From a descriptive point of view, the maximum imbibition phase of the membranes in SBF was observed at the T2 time point (2 days). This was indirectly deduced from the highest membrane weights measured in the time points considered in this study (data not showed).

In figure 46 the comparison of weight variation after aging in SBF was plotted. The membranes showed a linear constant weight loss justified by the loss of serum by the fibrin network.

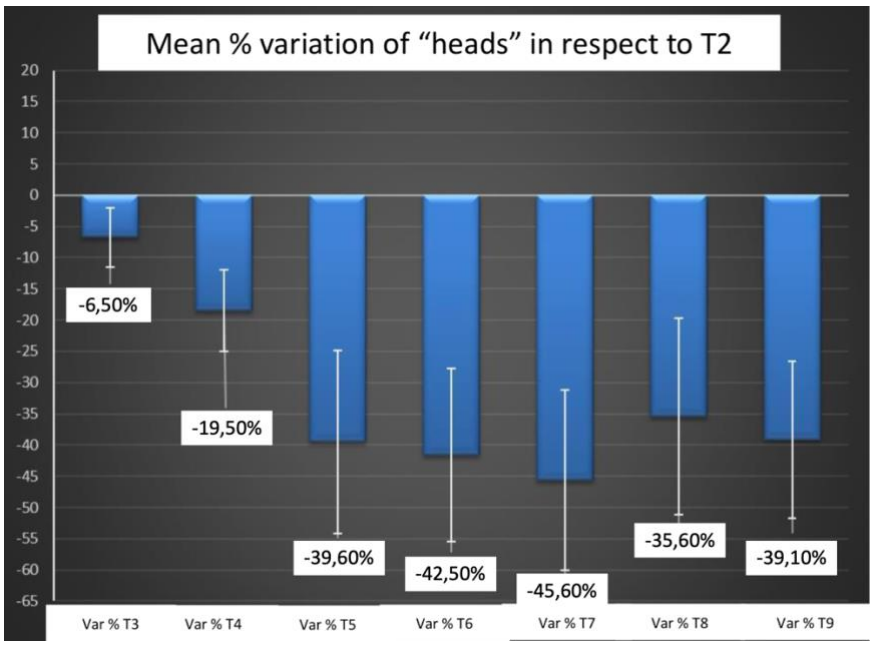

Fig. 46: percentage variation of weight with T2 of head samples.

Same analysis was conducted for the membranes’ tails (Fig. 47). A linear behavior can be seen during time, similarly to “head” samples, proportional to the aging. The differences in cell population present in heads and tails seems not to affect the weight variation during SBF aging.

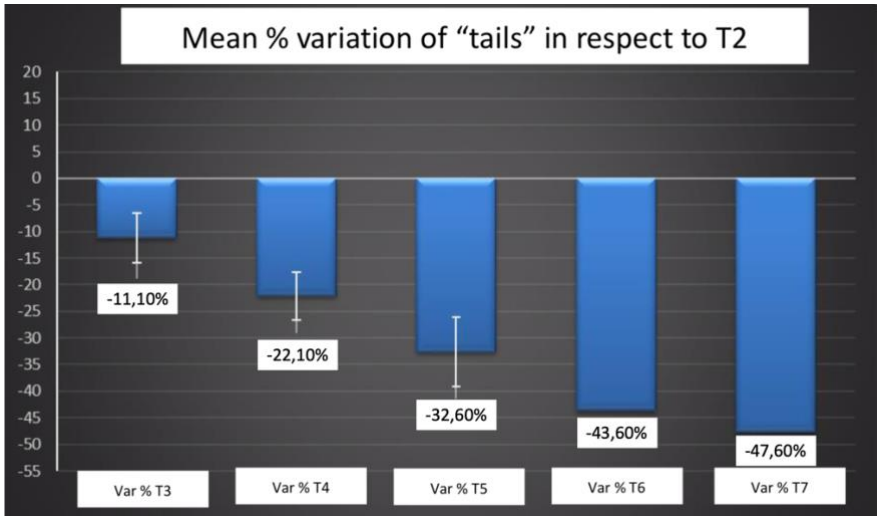

Fig. 47: percentage variation of weight with T2 of tail samples.

From the subsequent timepoints, a gradual decrease in weight was observed, substantially given by the dissolution of the fibrin reticulum. It was not possible to detect the increase of the pores during SEM analyzes since the sample preparation method (including the dehydration of the same) inevitably led to dry and therefore to the shrinkage of the same (Figures 48 and 54, 55).

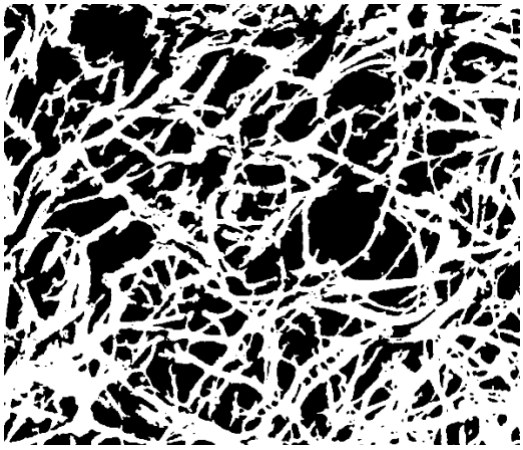

Fig. 48: pristine PRF membrane under 8000x magnification SEM microscope, after processing by DiameterJ of Fiji.

The graph of Fig. 49 show a constant fiber diameter of fibrin during time in the “head” samples. An expected swelling of the fibers did not take place. The diameters are under the microscale level.

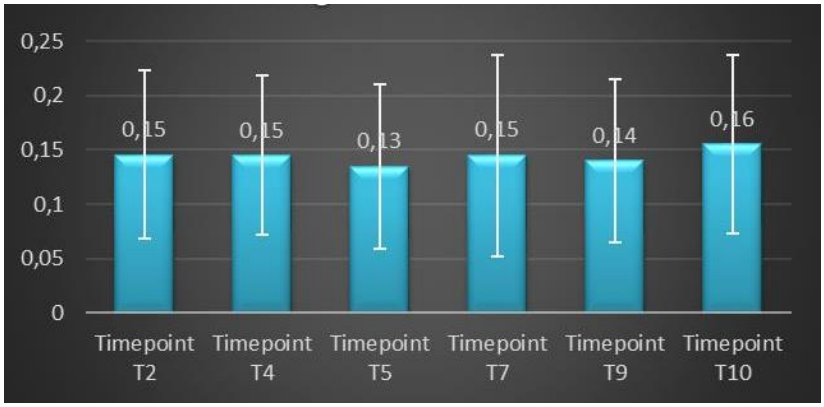

Fig. 49: mean and SD of diameter of fibers of head samples of PRF membranes (µm) at different timepoints.

The same behavior can be seen for the “tail” samples, without significant difference with the heads (Fig. 50).

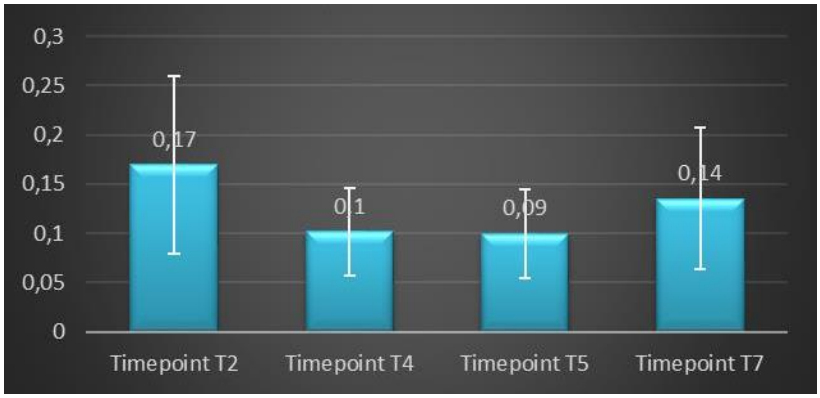

Fig. 50: mean and SD of diameter of fibers of tail samples of PRF membranes (µm) at different timepoints.

After fiber diameter assessment, also pores distribution was plotted after DiameterJ analysis of SEM images of the same membranes aged in SBF (Fig. 51). The porosity percentage remains constant during time, both for the heads and the tails. These graphs show a reliable structure of the membrane that highlights a morphological stability despite the weight loss. The most accredited explanation is a volume loss consequent to the serum loss and a hindered imbibition of SBF.

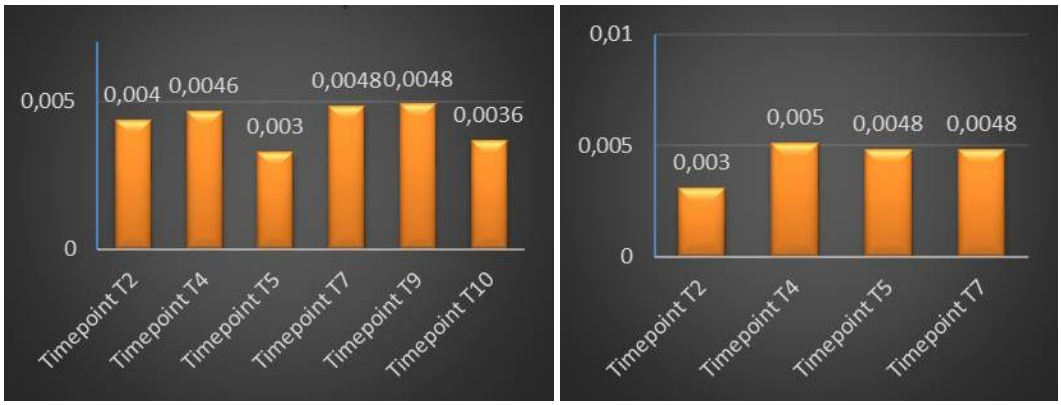

Fig. 51: percent porosity of head (left) and tail (right) samples of PRF membranes (values x 100) at different timepoints.

In all the SEM images examined (Fig. 52 and 53) no homogeneity was found in the pattern of fiber arrangement, both within the same membrane, and at the various time points. Conversely, the presence of a morphological and dimensional stability at the various time points of the fiber diameters has been found (Fig. 52 and 53). Furthermore, unlike the study by Sam et al. [50], in this experiment no cells were detected on the membrane surface. The absence of cells may be explained by the accurate irrigation of the membranes with SBF before dissolution assay.

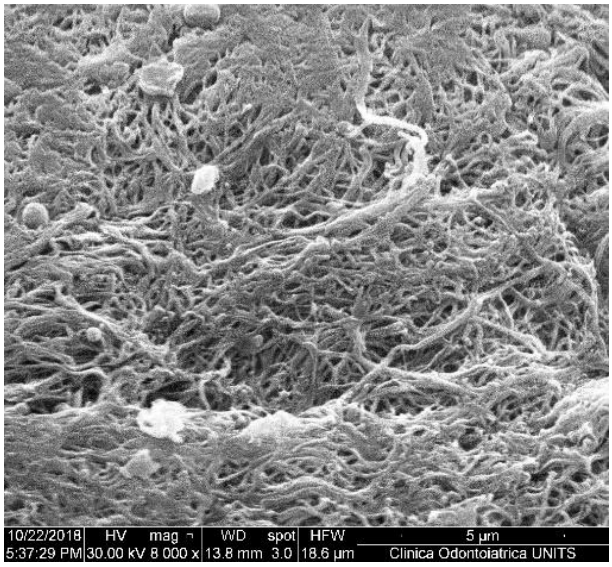

Fig. 52: pristine PRF membrane under 8000x magnification SEM microscope (Scale bar 5 µm), timepoint 10, head of sample n.8.

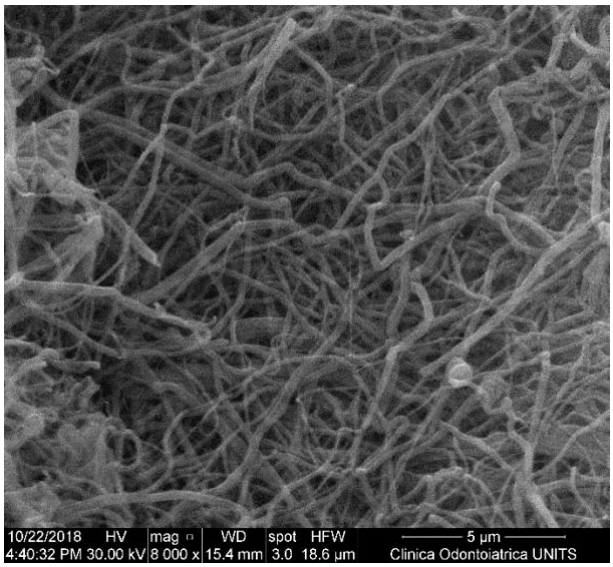

Fig. 53: pristine PRF membrane under 8000x magnification SEM microscope (Scale bar 5 µm), time point 2, tail of sample n.9.

Mechanical testing with DMA

The ultimate tensile strength was evaluated on both fresh pristine PRF membranes and with PRF membranes aged in SBF for three days (Fig. 54). Despite the reduced time-span, the three membranes, tested for the two time-points, showed a scattered behavior which was found to be not correlated to the aging. In fact, even though all the tested membranes showed the typical failure behavior of fragile materials (or with very limited plastic deformation), the values of both load and displacement at failure were not constant for the membranes of the same subgroup. It has to be

said, however, that a normalization of the data was not possible given the individual differences in terms of width, thickness and shape of the samples. Even if a standardized method in membrane production was adopted, the inner variability of the blood sample, the elimination of serum with the metal press and the cutting within the dog-bone shaped specimens, could have brought some differences. However, considering the limited load which these membranes can sustain, they cannot be considered as proper candidates for guided bone generation applications, given the minimal load required for this purpose, *i.e.* 2 N [115].

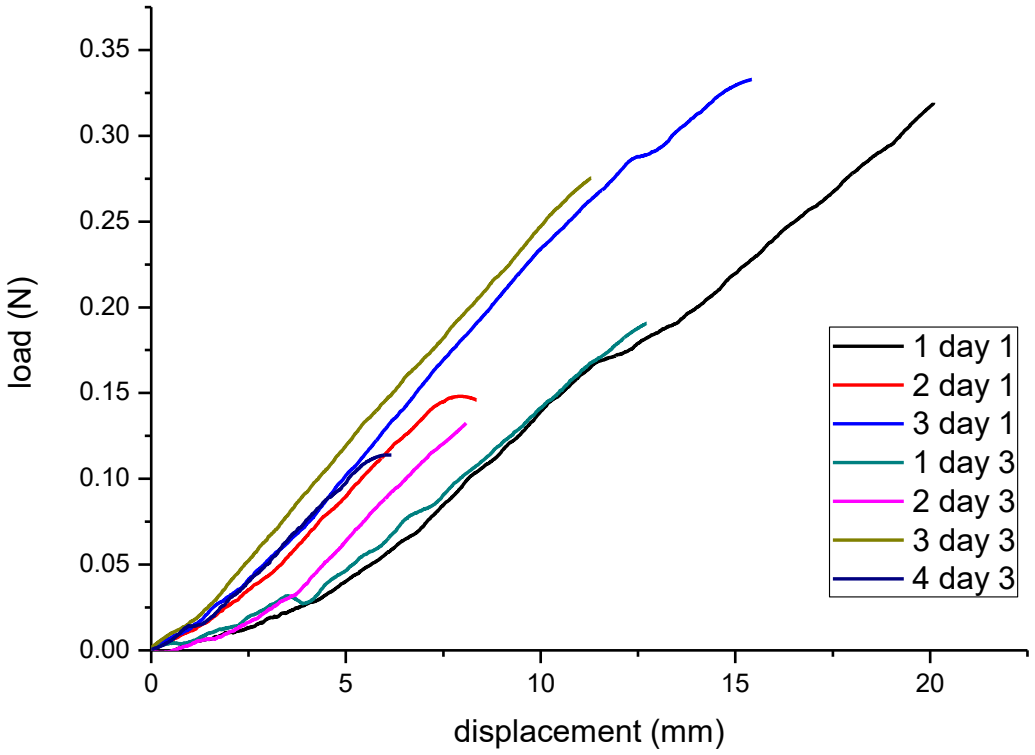

Fig. 54: load-displacement graph of dog-bone shaped sample of pristine PRF and after 3 days in SBF.

nHAp enrichment first experiment

After centrifugation (2700 rpm, 12 minutes) the three tubes for each of the scheduled nHAp addition (10mg, 1mg, 0,1mg) appear macroscopically separated in the usual two phases of fibrin clot (on the top) and red blood cells (on the bottom). Moreover, a variable quantity (proportional to the initial nHAp added) of non-entrapped nHAp has been found on the bottom of the vials (Fig. 57).

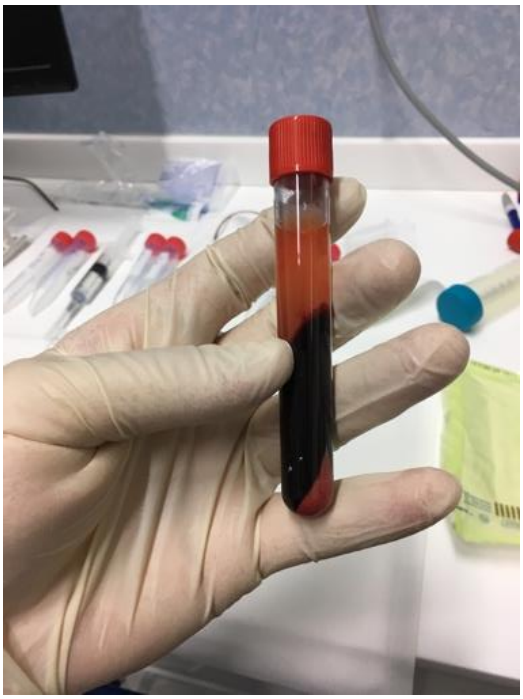

Fig. 55: exemplificative image of the nHAp sediment after centrifugation in the bottom of the vial. Serum and red blood cells phases can be distinguished.

After membrane production, cropping, fixing and metallization, the membranes appeared at SEM morphological analysis with randomly distributed nanometric fibers of fibrin. Isolated deposits of aggregates of nHAp were found in some regions of the sample, confirmed by backscattered electrons (Fig. 56). A uniform nHAp distribution on the membrane surface was not reached (Fig. 57).

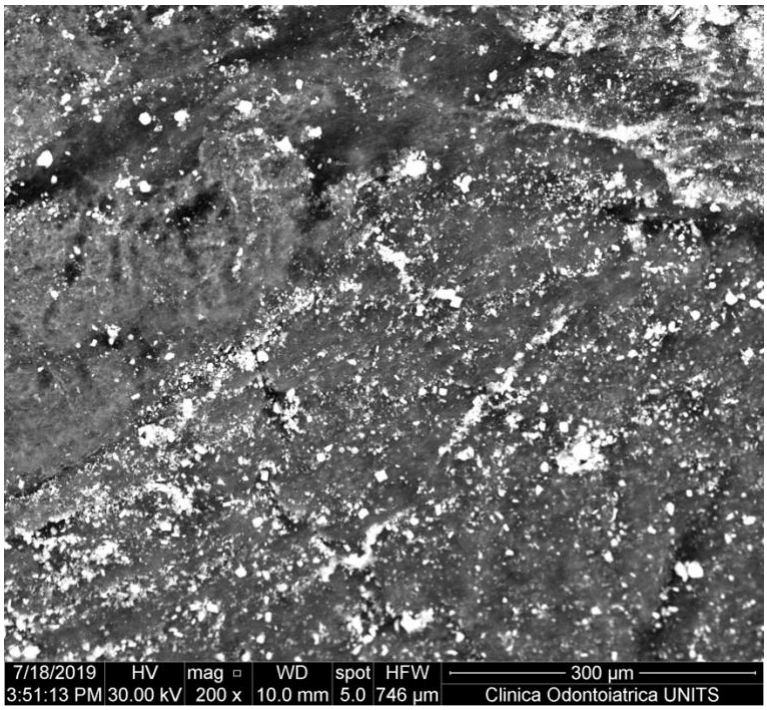

Fig. 56: nHAp enriched PRF membrane under 200x magnification SEM microscope (Scale bar 300 µm), HAp aggregates in bright white.

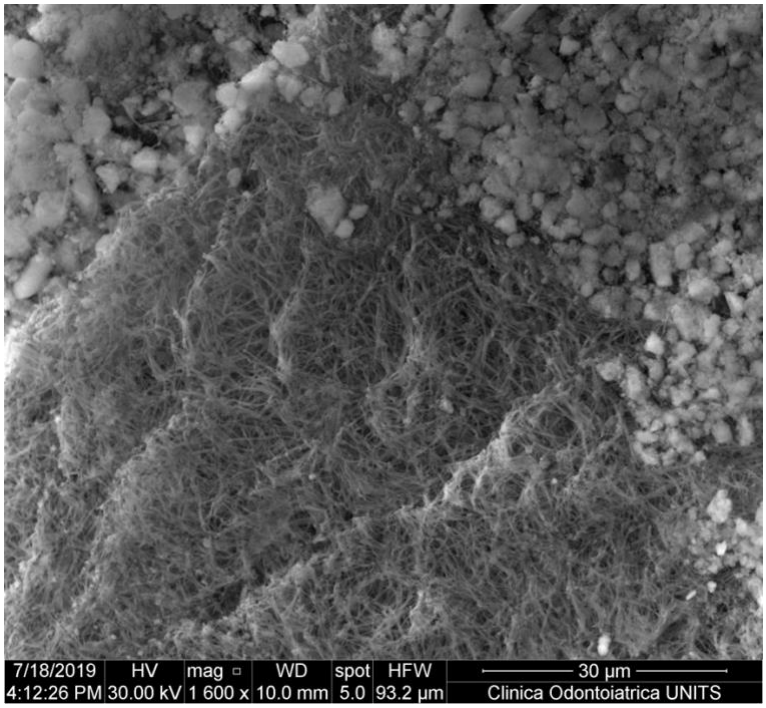

Fig. 57: nHAp enriched PRF membrane under 1600x magnification SEM microscope (Scale bar 30 µm), HAp aggregates in the upper part of the image.

SEM EDS morphologic and chemical analysis of HAp-enriched PRF membranes second experiment

The second attempt of nHAp enrichment of the PRF membrane was performed with the insertion of tubular Alg-nHAp scaffolds inside the tubes, before blood withdrawal. No sediment could be found on the bottom of the vials after centrifugation (2700 rpm, 12 minutes). The scaffolds were found always on the top of the clot (Fig. 58).

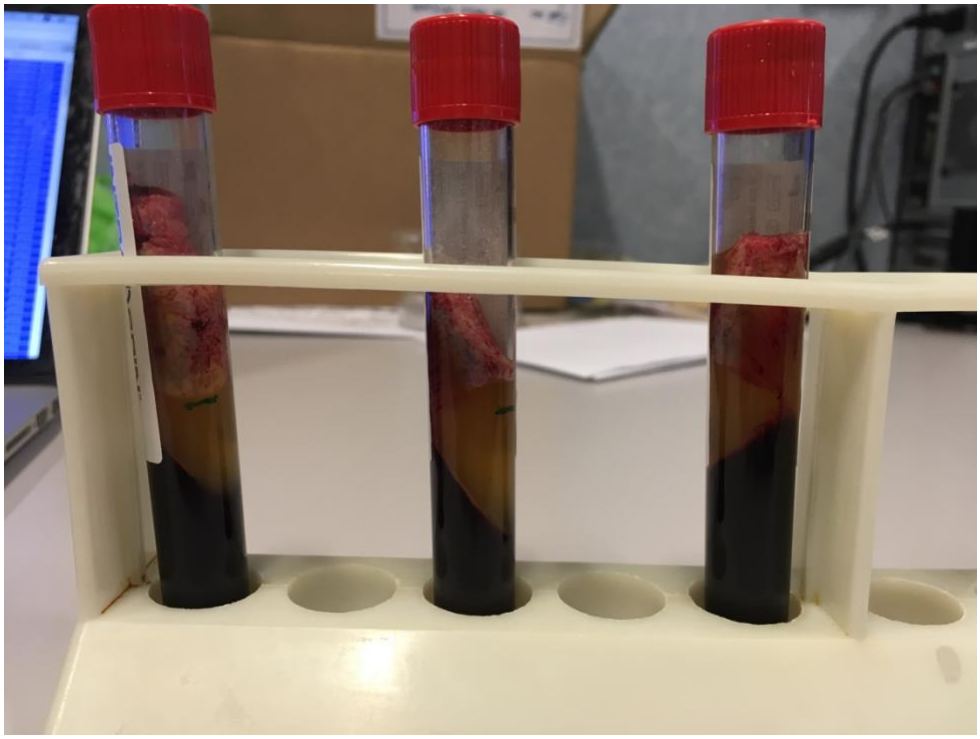

Fig. 58: three of the samples of Alg-nHAp scaffold after centrifugation with entire blood. The localization of the scaffolds in the fibrin phase can be observed.

Both scaffold and obtained PRF membranes were fixed and metallized for SEM analysis. The Alg-nHAp scaffolds did not show any trace of fibrin network, neither cells on the surface in all the samples. The membranes showed only a few traces of isolated deposits of crystal of nHAp similarly to the previous experiment, confirmed by EDS (Fig. 59 and 60). No homogeneous distribution of nHAp on the membranes surface could be found in all the three combinations of scaffold shape. Half of the samples of the membranes were carbon sputtered for EDS analysis, comprising a pristine freeze-dried Alg-nHAp scaffold as control (Fig. 59 and 60). The chemical analysis confirmed the presence of a Ca and P in the crystals observed (Fig. 64).

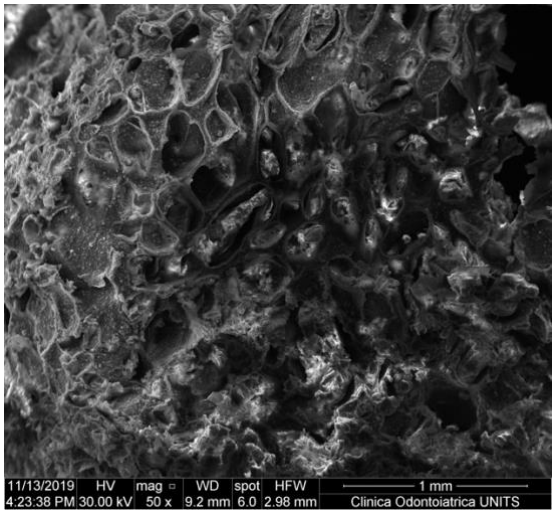

Fig. 59: SEM image of Alg-nHAp pristine scaffold under 50x magnification (Scale bar 1mm); pores are visible. The following EDS analysis has been conducted on this field.

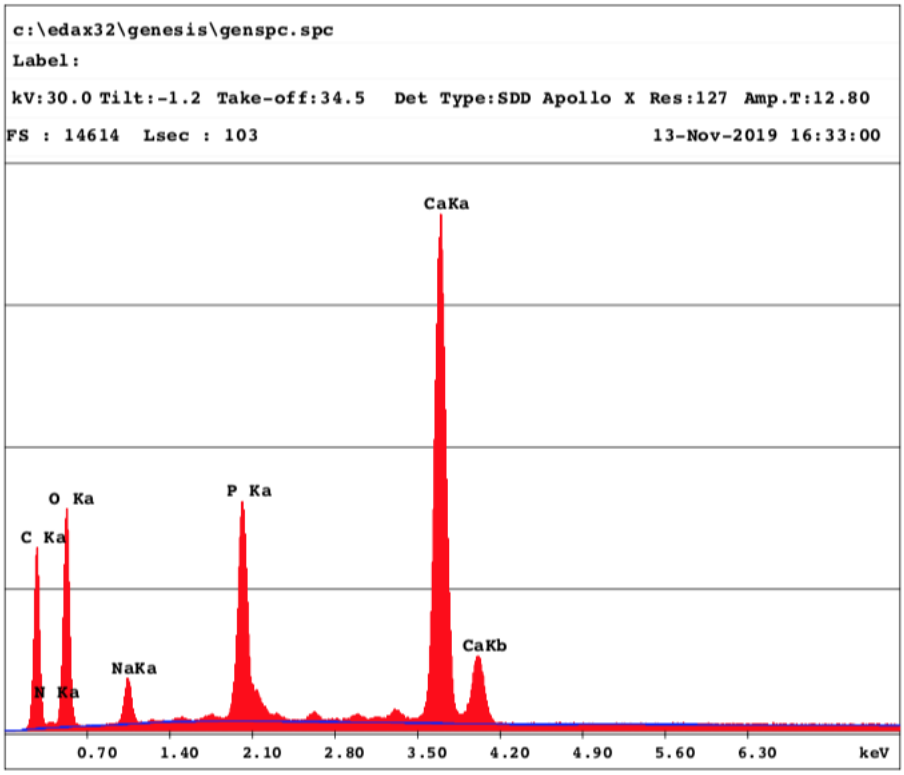

EDAX ZAF Quantification (Standardless)
Element Normalized
SEC Table : Default

Element	Wt %	At %	K-Ratio	Z	A	F
C K	34.49	46.47	0.1097	1.0224	0.3109	1.0005
N K	3.25	3.75	0.0033	1.0148	0.0997	1.0007
O K	37.88	38.31	0.0526	1.0080	0.1378	1.0001
NaK	3.09	2.17	0.0073	0.9470	0.2485	1.0010
P K	5.83	3.05	0.0422	0.9416	0.7629	1.0066
CaK	15.46	6.24	0.1465	0.9412	1.0064	1.0000
Total	100.00	100.00				

Fig. 60: EDS chemical analysis of the contents of the field of Fig. 59. The peaks of Ca and P can eb observed.

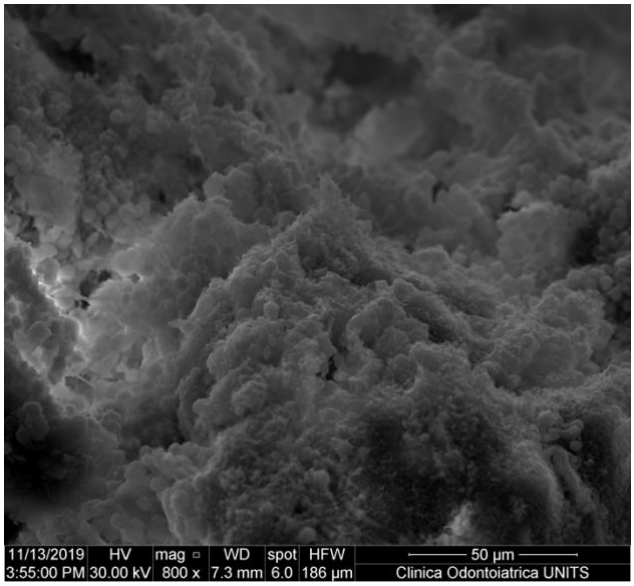

Fig. 61: nHAp enriched PRF membrane under 800x magnification SEM microscope (Scale bar 50 µm), HAp crystal aggregations are visible. The following EDS analysis has been conducted on this field.

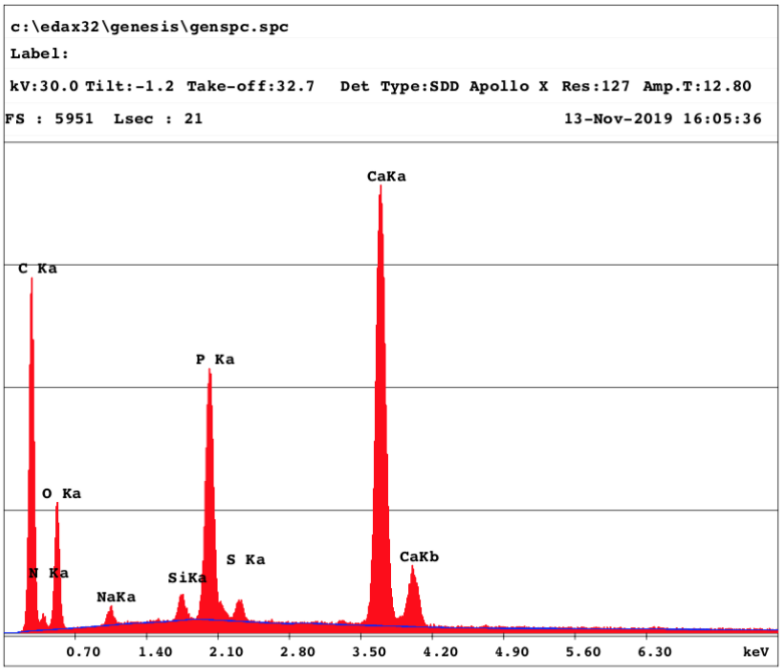

EDAX ZAF Quantification (Standardless)
Element Normalized
SEC Table : Default

Element	Wt %	At %	K-Ratio	Z	A	F
C K	51.75	63.75	0.1847	1.0161	0.3512	1.0003
N K	7.54	7.96	0.0066	1.0086	0.0874	1.0004
O K	22.16	20.49	0.0259	1.0018	0.1165	1.0001
NaK	0.91	0.58	0.0024	0.9412	0.2756	1.0010
SiK	0.57	0.30	0.0039	0.9670	0.7030	1.0075
P K	5.30	2.53	0.0411	0.9360	0.8228	1.0058
S K	0.44	0.20	0.0035	0.9612	0.8229	1.0087
CaK	11.35	4.19	0.1087	0.9343	1.0249	1.0000
Total	100.00	100.00				

Fig. 62: EDS chemical analysis of the contents of the field of Fig. 61. The peaks of Ca and P can be observed. Similar chemical report of the pristine Alg-nHAp of Fig. 60.

Chapter 3 bone regeneration analysis

It is generally agreed that a bone represents an individual organ of the skeleton, but the term ‘‘bone’’ has at least three different meanings. The first is mineralized bone matrix excluding osteoid; this use rigorously indicates the definition of bone as a hard tissue. Osteoid is bone matrix that will be (but is not yet) mineralized. The second meaning of ‘‘bone,’’ is bone matrix, whether mineralized or not, *i.e.*, including both mineralized bone and osteoid. The third meaning of ‘‘bone’’ is a tissue including bone marrow and other soft tissue, as well as bone as just defined. It should be appropriate to refer to the combination of bone and associated soft tissue or marrow as ‘‘bone tissue.’’ ‘‘Tissue’’ is defined as ‘‘an aggregation of similarly specialized cells united in the performance of a particular function” [116].

Histomorphometric analysis represents the state of art of regenerated bone assessment in terms of performance of the bone substitute, scaffold of membrane [117]. This examination requires the harvesting of a bone sample, usually retrieved with a trephine bur, from the living tissue. For ethical issues it is usually carried out in the animal model (for titanium implant retrieval) or even from the human. The latter option foresees the implant bed preparation with a trephine bur, thus the simultaneous bone core biopsy harvesting and the implant site preparation that allows the implant insertion without any other supplementary invasive procedure for the patient. The analysis represents a step further in respect of the histological examination of a mineralized tissue and requires experience, histological skills and facilities as well. In fact, it allows the quantification of mineralized tissue, marrow spaces, residual graft particles and regenerated bone together with bone microarchitecture [116]. It is actually, the most powerful tool for the assessment of bone regeneration process in two dimensions. Moreover, to obtain a slide suitable for histomorphometric analysis, well trained technician, standardized protocols, accuracy and time are required. The average time for preparing a slide form a bone core biopsy of 3mm x 10 mm is 21 days, while the acquisition at microscope and the analytic process requires about 3 hours. Moreover, histomorphometric analysis of human bone specimen may help in the diagnosis of metabolic bone disease such as osteoporosis and end stage renal disease. As such, this examination is still indicated under certain circumstances [118]. These are the reason why the possibility of organizing and optimizing a research group for the mineralised bone analysis has been explored; a process that required about three years, with the contribution of already established bone research laboratories (*e.g*. Hard Tissue an Biomaterial Research of Karl Donath Laboratory, University Dental Clinic of Vienna) brought to the establishment in the end of 2018 of the research group “Bone Lab” of the

University of Trieste, for mineralised tissue analysis, previously absent in UniTS thanks to which already a paper has been published [119]. Therefore, even if the histomorphometric analysis does not represent an experimental objective, it has been reported here because of the complementarity with the other two experimental parts. Moreover, the optimization of the protocol and the literature exploration, allowed us to standardize the SEM-EDS assays for the analysis of the mineralized tissue, starting from histologic slides. Similar protocols have been reported only twice in the current literature and allow a deeper analysis of bone.

Material and methods

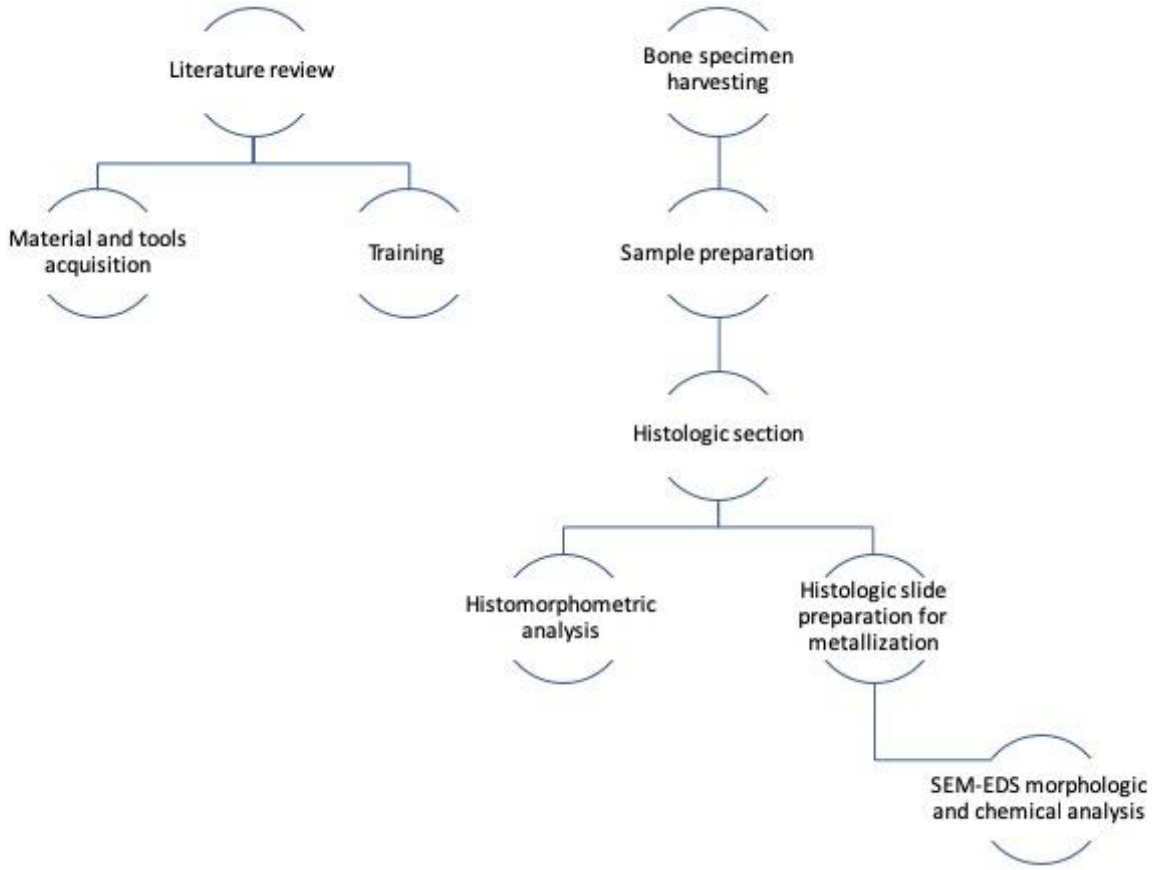

Fig. 63: experimental set-up

Materials

London White Resin (LWR- Sigma Aldrich); ethanol 99%; formaldehyde 4%; drill press, microtome, lapping machine with descending average roughness (*Ra*); Canada balsam; glass slides and coverslips; histological staining: acid fuchsine; toluidine blue; von Kossa staining; Masson's trichrome staining.

Samples preparation: collection

For the optimization of the histomorphometric protocol (at the time of writing, still not performed in UniTS but from research group in which this work was performed), bone samples were taken from both human patients and from sacrificed animals using a trephine drill, with a maximum diameter of 5mm and a maximum length of 10 mm. The analyzed samples derived from native bone, regenerated bone or native bone with and osseointegrated titanium dental implant. The first attempt of sample preparation have been made on fresh commercially available bone samples (bovine ribs) used for training of every stage of sample preparation and analysis. The specimens were harvested with a 3.5 mm external diameter trephine bur mounted on a surgical handpiece at 1200 rpm cooled with sterile saline solution. Other samples analyzed (data not reported) belonged to several research project for whom, the Bone Lab led the histomorphometric analysis. Ethical committee approved the protocols: SLSS protocol approved by CERU 60-2015-Os; SYNBIO protocol, approved by Cosenza 55/2016; GS protocol approved by Cosenza 66/2016; KTB protocol approved by CERU 42-2014-Os. Three cases were reported in this manuscript to present the procedure and clearly highlight its details.

Collection of sample: case 1

A Caucasian 50 years old healthy woman, no smoker, underwent to maxillary sinus floor elevation with lateral approach in 2003. A monocortical-cancellous block of fresh frozen allogeneic bone from iliac crest (FFB), which was shaped, positioned in contact with the sinus floor and stabilized with two screws, was used as graft. After 14 years of function the two implants inserted in the block failed due to untreatable peri-implantitis and were retrieved by using a counter-torque ratchet. After two months of healing, a new implant bed was prepared between the sites of the two removed fixtures by using a 3-mm trephine bur and a new implant was placed (Zimmer Biomet Dental, Palm Beach Gardens, USA).

Collection of sample: case 2

Exemplificative analyzes of the process were reported for a sample consisting of a titanium alloy implant (Ti, Al, V) grafted onto fresh bovine bone ribs (cortico-cancellous bone). The implant, compact bone, trabecular and cancellous bone samples were investigated for the analysis of the bone-implant interface.

Collection of sample: case 3

For exemplificative description of histomorphometric analysis with standard staining, a bone core biopsy from human maxillary sinus is here reported. Maxillary sinus lift is a regenerative procedure aiming at the restoration of the bone volume lost in the posterior maxilla, for dental implant insertion. Anterolateral portion of the maxillary sinus is exposed after the detachment of a full thickness flap, the bone is eroded till the achievement of the sinus membrane that is detached from the inner surface of the bone. The space therefore obtained is filled of bone substitute (in this case particles of deproteinized bovine bone) and the surgical access is closed. After six months of healing the second surgery takes place: with trephine bur one or more implant site are prepared and bone core biopsy can be obtained, as depicted in figure 81.

Collection of sample: case 4

This bone core biopsy was retrieved from a left maxillary bone in which a regenerative procedure was performed. This comprehended the filling of the bone defect with autologous bone harvested from an intraoral donor site, and the three-dimensional boxing of the defect with cortical bovine deproteinized lamina fixed with stainless steel screws. At the surgical reentry, the implant bed was prepared with a trephine bur allowing the harvesting of the biopsy for the histomorphometric analysis. In this case, the lamina was almost completely absorbed (1,5% of the total volume) together with the autologous bone particles. Thus the remaining sample is occupied by newly formed bone and marrow spaces (Fig. 82).

Samples preparation: resin inclusion

After harvesting procedure every sample was fixed in formalin (4%) for 24h-3 days according to the sample size. After fixation process, the sample was immersed ethanol 70% for 3 days, therefore in ethanol 90% overnight, then a second pass in a new ethanol solution of 90% for two hours and finally one day in ethanol 99% for 24 hours.

Two parts of London White Resin (LWR- Sigma Aldrich) and one part of 99% ethanol have been mixed and the sample embedded overnight. Following this step, the bone sample was embedded in a pure solution of LWR under vacuum overnight. After another day and a change of the resin, the samples have been put in the fridge for further resin infiltration of 5 days. Finally, the samples have been immersed in pure resin and place in an oven at 60° C for 24 hours.

Samples preparation: cutting

The sample included in solid resin has been paste onto a sample holder by means of an activator in order to obtain a complex formed by sample and sample holder, removing the excess of resin around the sample using a drill press. The obtained complex was fixed on a microtome sample holder, mount on a microtome, making sure to position the long axis of the sample parallel to the blade of the instrument before starting the cutting process.

After obtaining the desired slice, the sample has been removed from the microtome and from the sample holder of the instrument. The sample slices removed from the resin sample holder was paste on a glass slide using Attack™ glue. The attached sample was then placed under vacuum to eliminate possible incorporated bubbles.

Samples preparation: lapping

The sample was thinned with the LS 2 REMET lapping machine with the use of abrasive discs with different grain sizes, from P320 and P600 and finally P1200. The final goal was a global thickness of 100 µm for slices containing a titanium implant while for the bone samples, a final thickness of 40 A µm has been seek.

Samples preparation: polishing

Abrasive papers have been only used with the suction cup holder, all other accessories (Isomet-Buhler) have been used with the magnetic support.

For ISOMET-BUEHLER materials the following procedure have been performed:

1. After roughing the surface with the abrasive papers up to P1200 the suction cup holder has been replaced with the magnetic one.
2. TEXMET P cloth with the suspension 9 µm diamond abrasive paste.
3. ULTRAPAD cloth with the abrasive suspension diamond-coated 3µm.
4. VERDUTEX cloth with the abrasive suspension diamond-coated 1µm.
5. CHEMOMET cloth with the ALUMINA in suspension of 0.05 µm.

This procedure guarantees a mirror-like polish.

Samples staining: toluidine blue and acid fuchsine

Toluidine blue 1% solution was filtered at room temperature, then the sample was washed with distilled water and subsequently immersed in in acid fuchsine 1% solution for 7 minutes at room temperature, then washed with distilled water. The sample was finally put in oven at 40° C for 30

minutes. After this procedure a balsam of Canada was applied on the slide therefore covered by a coverslip.

Samples staining: Von Kossa and Red Neutral

Silver nitrate was dropped on the sample therefore placed under UV for 30 minutes. The sample was then immersed in thiosulphate for fixation for 5 minutes. The sample was washed with distilled water and immersed in neutral red solution for 5 minutes, then washed with distilled water and dried in the oven for 30 minutes at 40° C. As aforementioned, a balsam of Canada was applied on the slide therefore covered by a coverslip.

Samples staining: Masson Trichrome

Preparation of components: haematoxylin; solution A consisting of Rosso Ponceau, acetic acid, acid fuchsine; solution B consisting of phosphomolybdic acid, orange G and distilled water; solution C consisting of light green and acetic acid in distilled water.

1% solution of acetic acid in distilled water has been prepared, then the sample was coloured for 5 minutes by embedding in haematoxylin therefore rinsing under distilled water. Thereafter the sample was immersed for 2 minutes in solution A and then rinsed with 1% acetic acid solution. The sample was then immersed for 2 minutes in solution B and rinsed again with 1% acetic acid solution. Finally the sample was immersed in light green solution, rinsed with 1% acetic acid solution and following by 99% ethanol and xylol. The sample was then dried in oven at 40° C for 30 minutes. Once the sample got cold, balsam of Canada was applied followed by the coverslip.

Samples analysis: optical microscope image acquisition and merging

The slide has been watched at optical microscope (Biostar B3, Exacta Optech, San Prospero, Italy) with 40x, and 100x magnification calibrated with a dedicated calibration slide. For histomorphometric purposes, a series of 20 to 25 pictures was acquired at 40x magnification via a digital camera (Moticam 5.0, Motic, Hong Kong) and merged with a specific tool of Photoshop (photomerge). Every further qualitative and quantitative analysis was held through a medical screen of 32 inches with a digital magnification of 75%.

The final image of the sample in 2D has to go through some steps to be elaborated for the purpose of histomorphometric study. These steps include setting up a graphical scale and using specific programs such as Excel (Microsoft Corporation, Redmond USA), Photoshop (Adobe, San Jose USA) and Fiji (Sun-Java, National Institutes of Health USA).

To obtain a scale bar it is necessary to go to trace a known length in the image, which will be defined through a calibration slide on each optical microscope objective; in this specific case, 40x magnification was used.

Photoshop and Fiji:

Once the scale is set, the image is elaborated in Photoshop for the identification of the specific areas of tissue to be analyzed. To this end, a specific protocol has been refined as reported.

Image setting is modified in RGB colour, then with quick selection tool is possible to select the total area to go to analyze. With quick mask mode is possible to highlight the unselected area in red to modify and refine contours via brushing tool. After exiting quick mask mode the whole selected area is be outlined, ready to copy and paste on the new sheet the area selected for quantitative analysis. With Fiji is suggested to filter the image using the grey scale (IMAGE> TYPE> 16 BIT); through the threshold tool is possible to proceed with the study of the image obtained to isolate structure by structure (*e.g.* cortical bone, spongiosum bone, bone substitutes). The structures not isolable with this tool must be highlighted manually with photoshop and then quantified via Fiji (Fig. 62). For each isolated sub-region (*e.g.* cortical bone, residual graft, marrow spaces) the selection is quantified (edit> select> create selection) via measure tool. Once the measurements are obtained have to be into an Excel sheet. To obtain the sum of the total area, it is sufficient to go and relate the area of the specific structure analyzed with the area of the total image selection (partial area / total area) * 100.

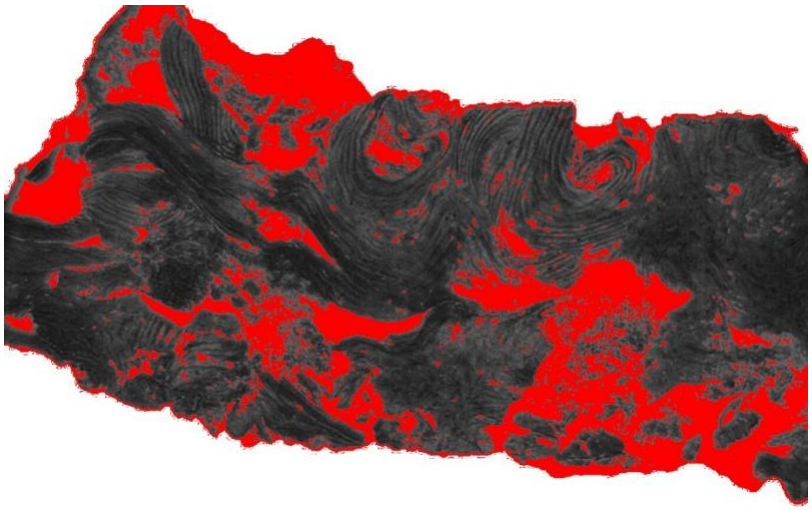

Fig. 64: allogenic graft retrieved from human maxillary sinus. The threshold fractioning using Fiji tool can be observed. Von Kossa staining, optical microscope 10x.

Histomorphometric indices

Conductivity index of bone particles (BPCi): is defined as BPCi = LC / PG, where LC is the sum of the contact lengths between the newly formed bone and the bone graft particles, while PG is the sum of the perimeters of the bone graft particles. This index goes from 0, when new bone is not present (only bone transplantation), to 100% when the bone graft particles are completely surrounded by the host tissues. As such, it can only be measured when material particles are present.

Trabecular thickness (Tb.Th) and trabecular spacing (Tb.Sp): Tb.Sp measures trabecular connectivity; it increases with trabecular bone loss. Tb.Th is a measure of the trabecular structure, it is reduced by age and osteoporosis.

To get Tb.Th: the image has to be elaborated with Photoshop to differentiate bone graft from native bone areas as mentioned above. The contrast between the content and the background is therefore enhanced according to a colour imposition: white background and black background. With Fiji the tool Tb.th is found in the BoneJ plugin, under thickness menu. To obtain Tb.Sp the same methodology used to obtain Tb.th was held, but this time using the image selected with Photoshop in which the non-mineralized portion was delimited.

To calculate the Bone to implant contact (BIC), in case of titanium implant inserted in bone is easily lead using the segmented line tool of Fiji to trace the bone contour in contact with the implant (Fig. 63) thread to be compared with the total amount of the implant profile. After measuring the lengths data are exported in Excel. To obtain the relationship between the total perimeter and the bone in contact with the surface of the plant: BIC (pixel)> = (sum of segments / total perimeter) * 100 = BIC%

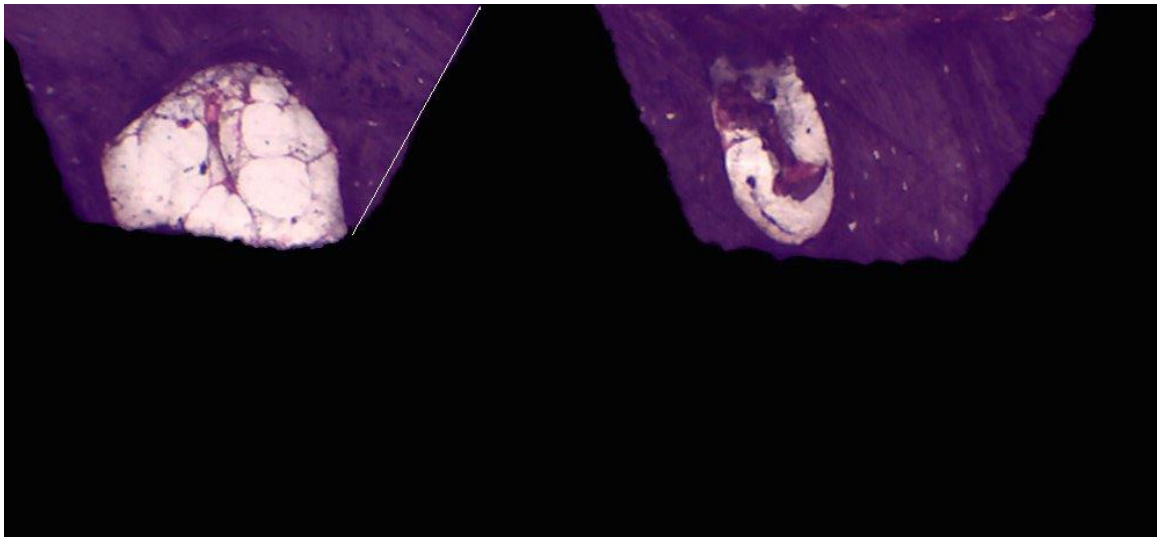

Fig. 65: titanium implant in *ex vivo* model for BIC calculation. Von Kossa staining, optical microscope 40x magnification.

Samples preparation for SEM-EDS analysis

After image acquisition via optical microscope, the slide has been lapped again after removing the coverslip. After lapping procedure to remove balsam and superficial staining, the glass slide has been cut with diamond cutter for glass and attached to a stub covered by a carbon adhesive. The sample has been carbonated with Sputter Coater K550X (Emitech, Quorum Technologies Ltd, UK).

SEM-EDS analysis

The images were acquired with a SEM (Quanta 250 SEM, FEI, Oregon, USA) operating in secondary electron acquisition mode. The working distance (WD) has been modulated so as to obtain the desired magnification; the acceleration voltage has been set at 30 kV, spot at 5.0, high vacuum (between 10^{-3} and 10^{-4} Pa). The analysis of the chemical composition of the samples was performed with an energy dispersion probe (EDS) (Quanta250 FEI with EDAX probe, Hillsboro, OR, USA) coupled to the electron microscope, using an acceleration voltage of 30 kV and a time scanning variable between 2 and 5 minutes.

The SEM-EDX analysis was initially performed on compact, trabecular and medullary bone tissue in such a way as to have reference values with which it is possible to compare, at a later date, the results obtained from the analysis of the bone-implant interface. The titanium implant surface was also evaluated especially at the interface with surrounding bone. During analyzes with the EDX chemical probe the results relating to carbon levels (C) could be distorted considering that the carbonation process goes to add C atoms on the surface of the sample.

Results

Case 1: Histomorphometric analysis of homologous bone block alter 9 years von Kossa staining

The bone biopsy was fixed and prepared as reported above for histomorphometric analysis. The slides were stained with acid fuchsine-toluidine blue and von Kossa staining. Bone histomorphometric analysis was performed evaluating the following measures: bone volume/total volume (BV/TV), native bone (NB), newly formed bone (NFB), residual graft (RG), non-mineralized tissue (NMT). Other static measures were performed: bone-particle conductivity index (BPCi), defined as BPCi = LC/PG in which LC is the sum of contact lengths between new bone and bone graft particles and PG is the sum of perimeters of bone graft particles; trabecular thickness (Tb.Th) and trabecular spacing (Tb.Sp) as useful data for morphological and metabolic bone behavior.

Histomorphometric analysis highlighted residual graft particles, even if completely surrounded by newly formed bone, identified thanks to the presence of empty osteocyte lacunae. Native bone of the residual crest, characterized by fewer marrow spaces, was in deep connection with the regenerated bone. No inflammatory cells were found. The global morphology of the specimen reflected a low-quality D4 native bone (Fig. 64).

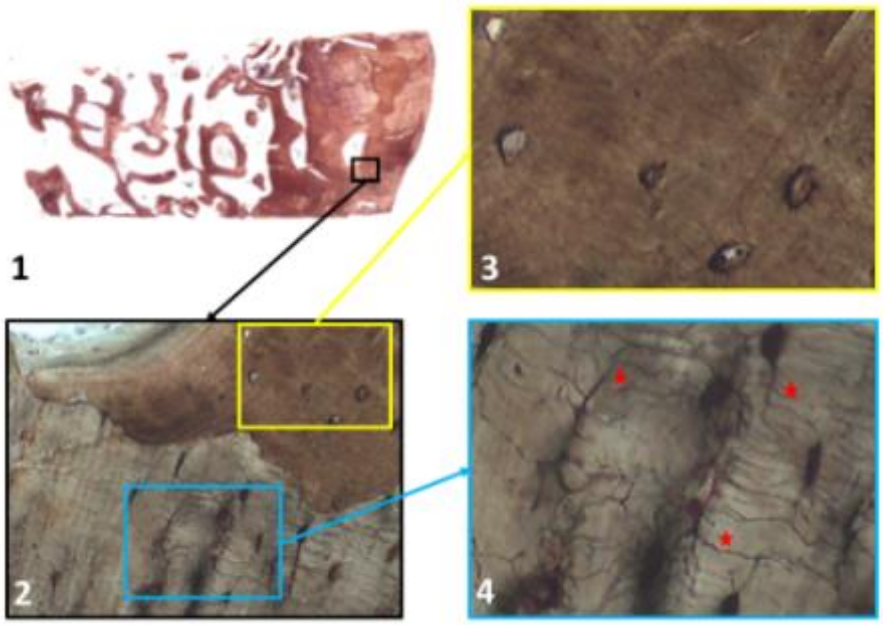

Fig. 66: undecalcified section of the bone specimen retrieved from the maxillary sinus. 1) whole sample; 2) detail of NFB inhabited by dendritic-like osteocytes with cell-to-cell contacts (red stars in picture 4); 3) RG with empty osteocyte lacunae, absence of dendritic-like cells. 4) NFB with osteocytes. Von Kossa staining, resin inclusion, 40x and 400x total magnification.

Lamellar bone with primary and secondary osteons could be found together with cemented lines. Normal population of osteocytes and osteoblasts and absence of osteoclasts reflected the

physiological behavior of maxillary bone. An interesting finding was a possible pseudo-dendritical activity of some osteocytes found on the boundary between old and new bone (Fig. 66).

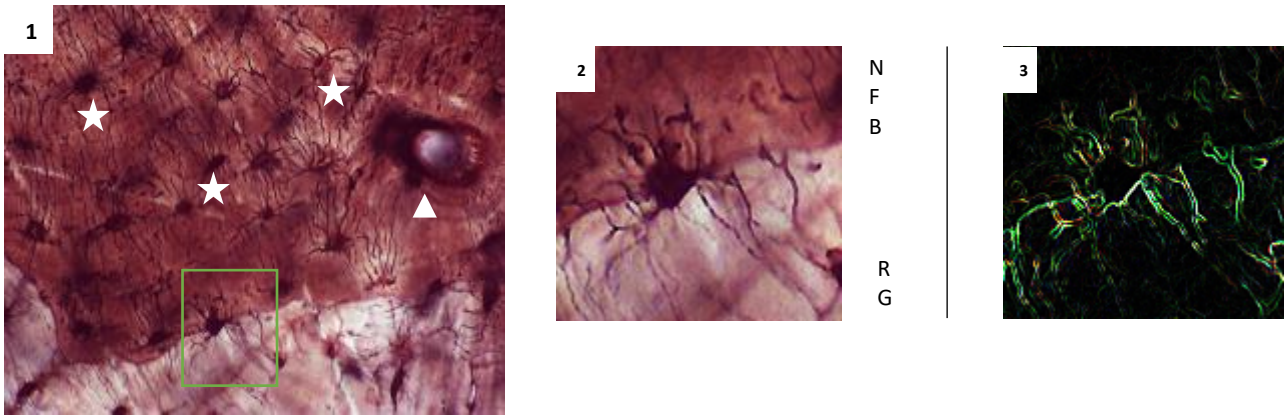

Fig. 67: undecalcified section of lamellar bone (detail of Fig. 3) 1) interface between NFB and RG (below); 2) close-up of an osteocyte with pseudo-dendritical activity towards RG, highlighted by software post-processing in 3). Note the presence of a primary osteon (arrowheads) and osteocytes (stars). Von Kossa staining, resin inclusion, 40x and 400x total magnification.

Histomorphometric analysis showed 40,8% of vital bone, 15,4% of residual graft particles and 43,8% of marrow spaces. BPCi of the residual graft particles was 47,5%; Tb.Th showed an average of 0,34 mm ± 0,21 with maximum value of 0,76 mm; Tb.Sp showed an average of 0,2 mm ± 0,2 with maximum value of 0,44 mm (Fig. 66).

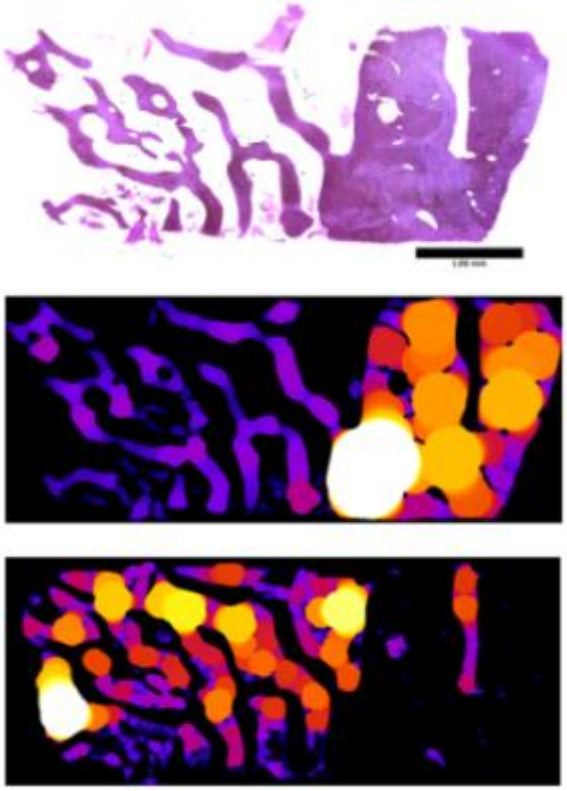

Fig. 68: from top to bottom: undecalcified section of the bone specimen, acid fuchsine-toluidine blue staining, 40x magnification; graphic appearance of trabecular thickness index; graphic appearance of trabecular spacing index.

After histologic examination under optical microscope, the slide underwent the process exposed above of re-lapping and carbon sputtering for SEM-EDS analysis. From backscattered SEM analysis, the mineralized tissues appeared homogeneous without any sign of gap between RG and NFB; only a slight discoloration between the parts could be found, according to the same findings obtained by optical microscope (Fig. 69). EDX analysis showed the same content of Ca and P and the same ratio between the two elements, when analyzing three couples of adjacent portions of RG and NFB (Fig. 68). These findings brought to a publication on an impacted journal [119].

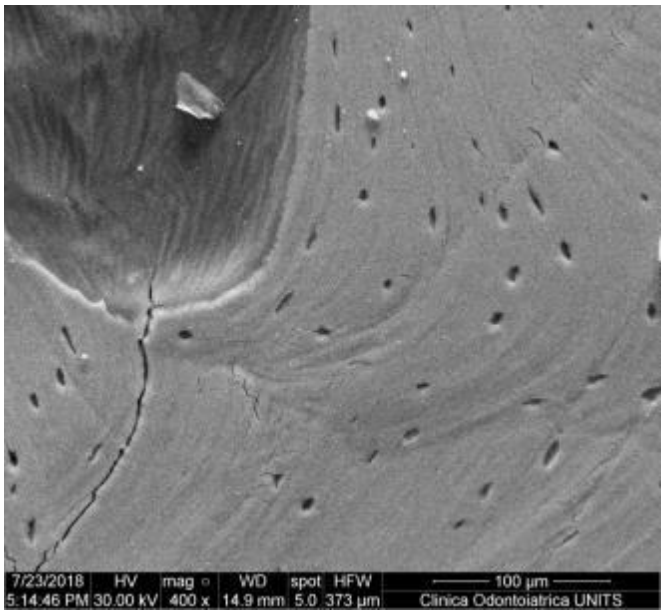

Fig. 69: secondary electrons SEM image of the interface between NFB (upper-right), RG (lower) and MS (upper-left). SEM, scanning electron microscope (scale bar: 100 µm).

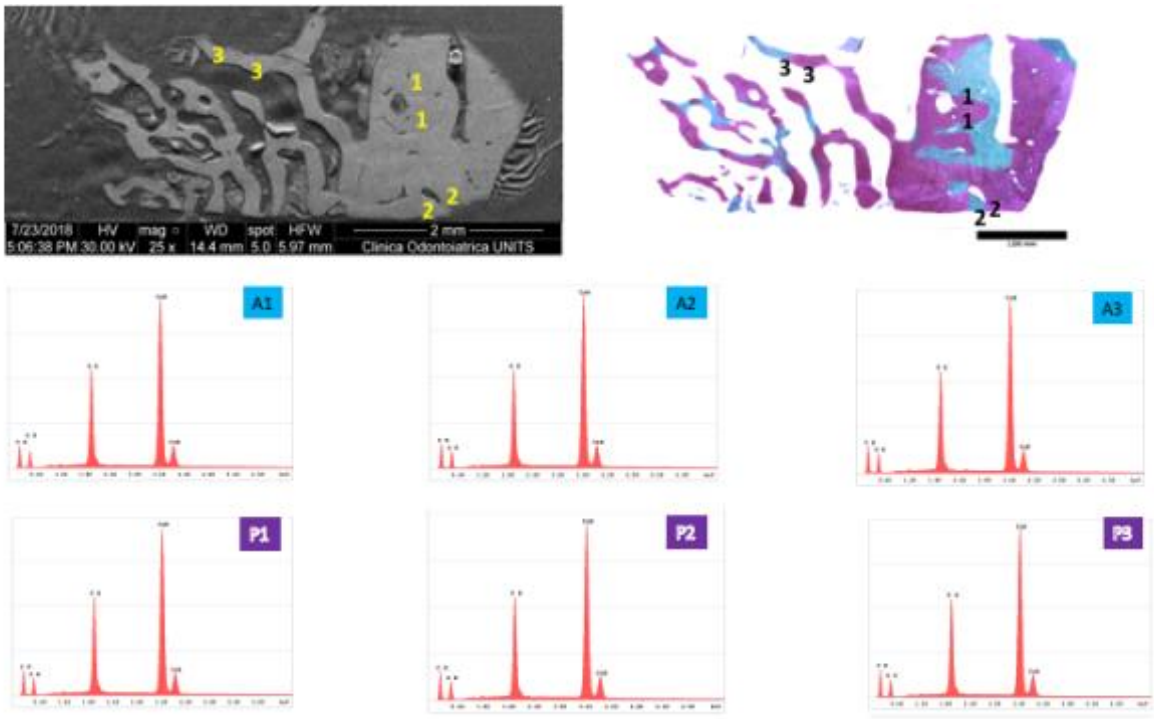

Fig. 70: Upper left: detail of secondary electrons SEM image of the bone specimen with the numerical identification of the sites selected for EDX analysis; upper right: histological section stained with acid fuchsine-toluidine blue modified according to histomorphometric results to highlight NFB (azure) and RG (purple) with correspondence of numerical reference for EDX examination; A1, A2, A3: EDX analysis for NFB; P1, P2, P3: EDX analysis for RG.

Case 2: Histomorphometric and SEM-EDS analysis of ex vivo retrieved titanium implant from bovine bone

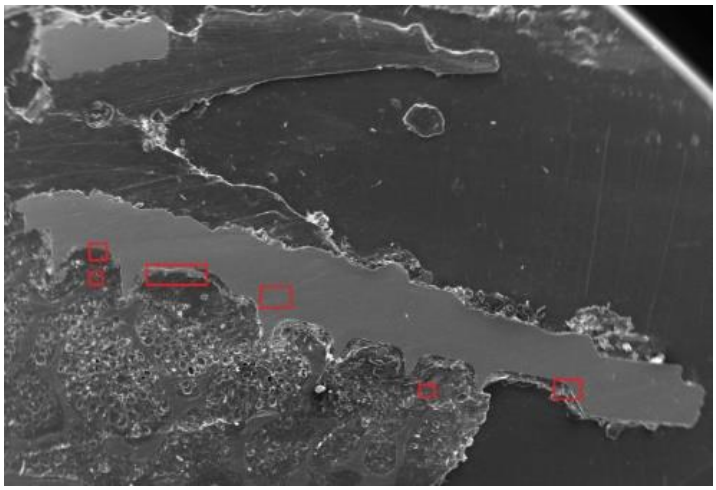

Fig. 71: secondary electrons SEM image of the interface between bone and titanium implant surface. Highlighted are the region of further EDX analysis.

With the EDX analysis it was possible to identify which was the Ti alloy of the plant; the values acquired are: Ti (78.30%), Al (5.35%) and V (2.36%). The titanium alloy found in the examined implant corresponds to the Titanium, Aluminum (6%) and Vanadium (4%) alloy (Grade 5).

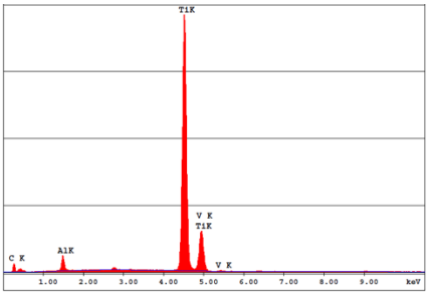

EDAX ZAF Quantification (Standardless)
Element Normalized
SEC Table : Default

Element	Wt %	At %	K-Ratio	Z	A	F
C K	13.98	38.25	0.0416	1.1353	0.2617	1.0009
AlK	5.35	6.52	0.0187	1.0476	0.3325	1.0041
TiK	78.30	53.71	0.7610	0.9685	1.0035	1.0000
V K	2.36	1.52	0.0228	0.9501	1.0165	1.0000
Total	100.00	100.00				

Fig. 72: EDX analysis of titanium of the implant depicted in figure 71. Element abundances are expressed graphically on the left (x-ray spectrum) and quantitatively on the right of the image (WT% column).

Figure 73 shows the cancellous-bone area in which EDS analysis revealed high levels of C (66.05%) and low levels of Ca (11.57%).

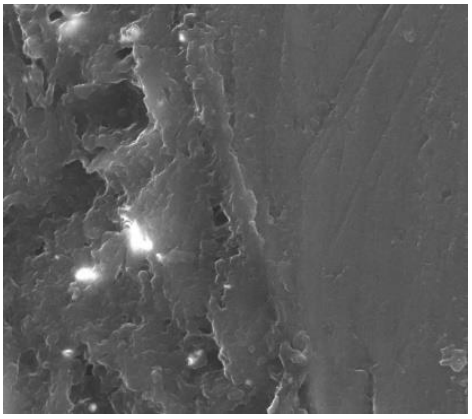

Fig. 73: Secondary electrons SEM image of cancellous bone on which EDX analysis was performed.

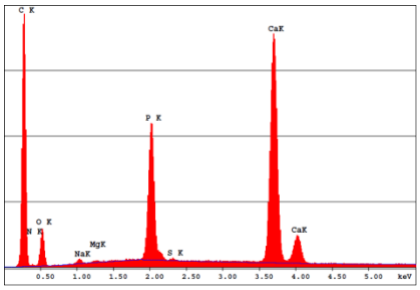

EDAX ZAF Quantification (Standardless)
Element Normalized
SEC Table : Default

Element	Wt %	At %	K-Ratio	Z	A	F
C K	66.05	78.25	0.2666	1.0139	0.3980	1.0002
N K	2.01	2.04	0.0015	1.0064	0.0751	1.0002
O K	14.32	12.74	0.0158	0.9997	0.1102	1.0001
NaK	0.39	0.24	0.0011	0.9392	0.2989	1.0011
MgK	0.13	0.08	0.0005	0.9640	0.4316	1.0022
P K	5.45	2.51	0.0448	0.9341	0.8741	1.0060
S K	0.07	0.03	0.0006	0.9592	0.8559	1.0096
CaK	11.57	4.11	0.1121	0.9320	1.0395	1.0000
Total	100.00	100.00				

Fig. 74: EDX analysis of cancellous bone the area depicted in figure 73. Element abundances are expressed graphically on the left (x-ray spectrum) and quantitatively on the right of the image (WT% column).

The results obtained confirm the presence of a tissue with a high prevalence of organic matrix and therefore a poor mineralization. The analyzed section occupied by compact bone tissue showed high levels of Ca (24.23%) and low levels of C (42.32%).

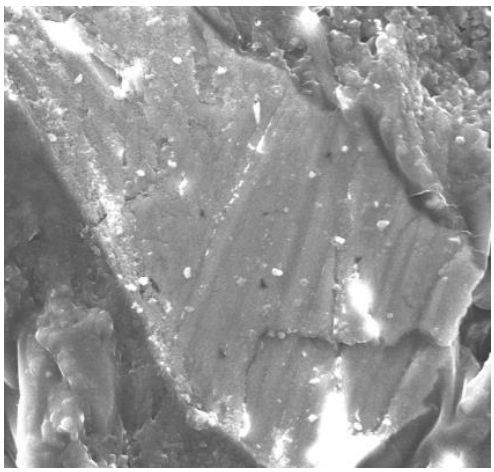

Fig. 75: Secondary electrons SEM image of mineralized tissue on which EDX analysis was performed.

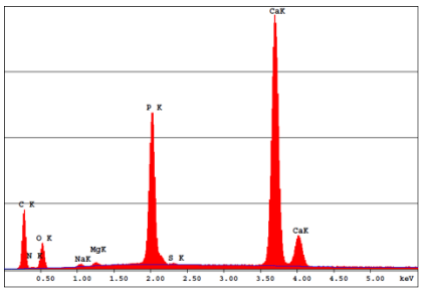

EDAX ZAF Quantification (Standardless)
Element Normalized
SEC Table : Default

Element	Wt %	At %	K-Ratio	Z	A	F
C K	42.32	60.07	0.1104	1.0283	0.2536	1.0003
N K	2.50	3.04	0.0019	1.0207	0.0748	1.0003
O K	18.23	19.43	0.0192	1.0138	0.1039	1.0002
NaK	0.45	0.33	0.0011	0.9524	0.2629	1.0020
MgK	0.44	0.31	0.0016	0.9774	0.3788	1.0040
P K	11.74	6.46	0.0905	0.9470	0.8065	1.0098
S K	0.10	0.05	0.0007	0.9724	0.7148	1.0149
CaK	24.23	10.31	0.2246	0.9482	0.9779	1.0000
Total	100.00	100.00				

Fig. 76: EDX analysis of the mineralized bone of the area depicted in figure 75. Element abundances are expressed graphically on the left (x-ray spectrum) and quantitatively are on the right of the image (WT% column).

From the analysis of the bone-implant interface non-homogenous results were obtained from the three area of sampling: Ca (from 16 to 21%) was comparable to the levels found on compact bone (Ca = 24.13%) around the implant. Only the analysis of a single site at the interface level shows a low Ca level (Ca = 5.23%) and high C levels (75.57%), indicative of organic, and therefore of a non-mineralized component such as a marrow space.

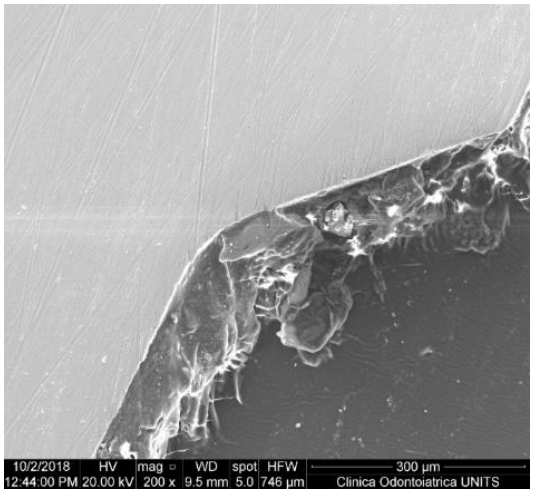

Fig. 77: Secondary electrons SEM image of the interface between bone and titanium implant surface on which EDX analysis was performed.

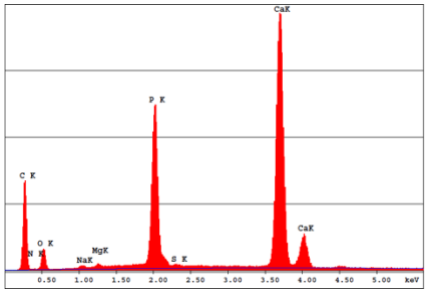

EDAX ZAF Quantification (Standardless)
Element Normalized
SEC Table : Default

Element	Wt %	At %	K-Ratio	Z	A	F
C K	52.04	69.82	0.1463	1.0246	0.2743	1.0003
N K	1.83	2.10	0.0013	1.0170	0.0719	1.0002
O K	13.10	13.20	0.0135	1.0102	0.1023	1.0002
NaK	0.61	0.43	0.0016	0.9490	0.2810	1.0019
MgK	0.58	0.38	0.0023	0.9739	0.4028	1.0037
P K	10.46	5.44	0.0829	0.9436	0.8323	1.0093
S K	0.33	0.17	0.0024	0.9690	0.7478	1.0137
CaK	21.05	8.46	0.1969	0.9440	0.9909	1.0000
Total	100.00	100.00				

Fig. 78: EDX analysis of the bone-implant interface depicted in figure 77. Element abundances are expressed graphically on the left (x-ray spectrum) and quantitatively on the right of the image (WT% column).

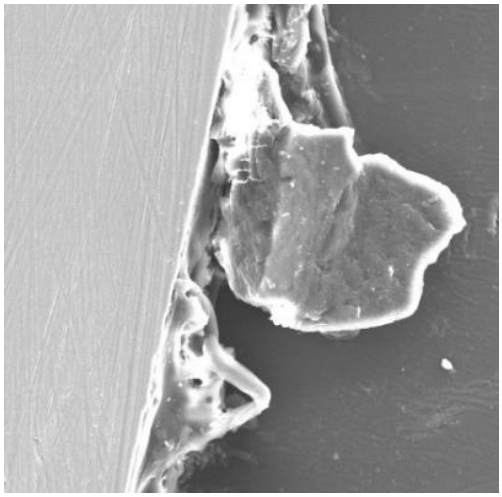

Fig. 79: Secondary electrons SEM image of the interface between bone and titanium implant surface on which EDX analysis was performed.

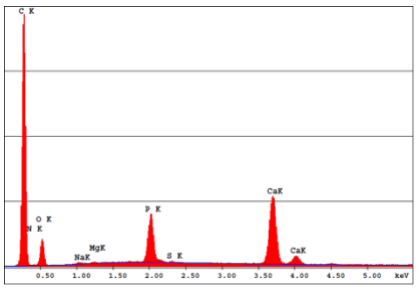

EDAX ZAF Quantification (Standardless)
Element Normalized
SEC Table : Default

Element	Wt %	At %	K-Ratio	Z	A	F
C K	75.57	83.37	0.4014	1.0077	0.5270	1.0001
N K	1.77	1.67	0.0014	1.0002	0.0767	1.0002
O K	14.31	11.85	0.0165	0.9935	0.1159	1.0000
NaK	0.19	0.11	0.0006	0.9335	0.3161	1.0006
MgK	0.10	0.06	0.0005	0.9581	0.4591	1.0011
P K	2.78	1.19	0.0234	0.9284	0.9046	1.0031
S K	0.05	0.02	0.0004	0.9535	0.9292	1.0052
CaK	5.23	1.73	0.0516	0.9249	1.0676	1.0000
Total	100.00	100.00				

Fig. 80: EDX analysis of the bone-implant interface depicted in figure 79. Element abundances are expressed graphically on the left (x-ray spectrum) and quantitatively on the right of the image (WT% column).

Case 3: Histomorphometric analysis of human bone regeneration, toluidine blue and acid fuchsine stain

The acid fuchsine and toluidine blue staining represents the standard for mineralized bone staining, allowing the detection of both acidophilus and basophilic structures, likewise to hematoxylin and eosin. As depicted, the bone core biopsy highlights two macro-components: native bone and regenerated bone. This aspect is extremely important for the subsequent analysis because the non-comprehension of this division would bring to a bias in the histomorphometric values. Thus, for the native bone, only a quantification of the ratio between mineralized tissue and the marrow space can be provided, together with the measurement of the residual crestal bone height at the time of implant placement. For the grafted area (right side of figure 79) different parts can be highlighted: newly formed bone, residual graft particles, non-mineralized tissue. The ratio between these components and the total volume of the specimen (or better, the grafted area) provide the most important data of the histomorphometric analysis. The qualitative distinction of the parts that serves for the quantitative analysis is guided from the staining and from the characteristics of both the native bone and the grafted materials. Native and newly formed bone (host) can be distinguished thanks to the vital osteocytes presence (blue stained) and to the intensity of the staining: older bone appears paler. For the grafted part, it depends on the nature of the graft (autografts, allograft, xenograft, alloplastic). In the analyzed sample, the residual graft particles (bovine bone) appear blue (basophilic) without any sign of *nuclei* in the osteocyte *lacunae*.

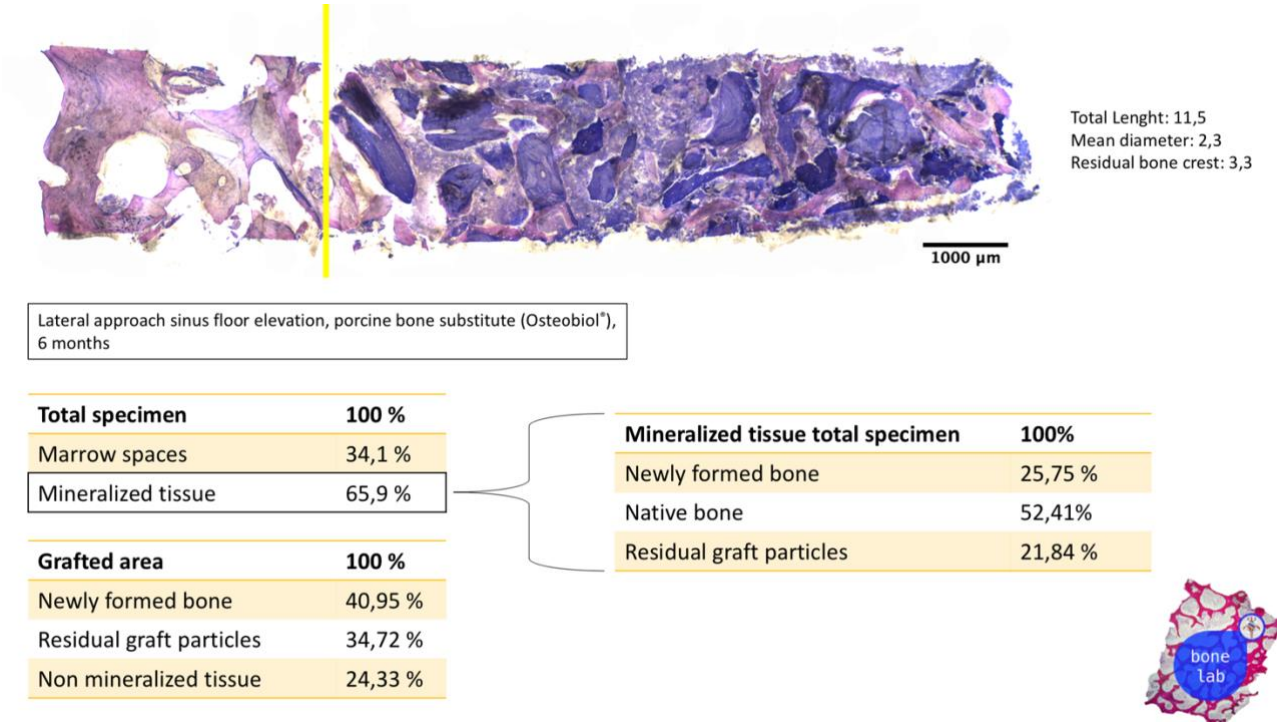

Fig. 81: human bone core biopsy from xenogenic graft, acid fuchsin and toluidine blue stain. Optical microscope, 40x magnification.

Case 4: Histomorphometric analysis of autologous graft for bone regeneration, trichrome Masson stain

This sample allows the comprehension of the qualitative contribute of trichome stain for the mineralized tissue analysis. Likewise the previous sample, even if with a more difficult analysis, quantitative data can be provided (Tab. 5).

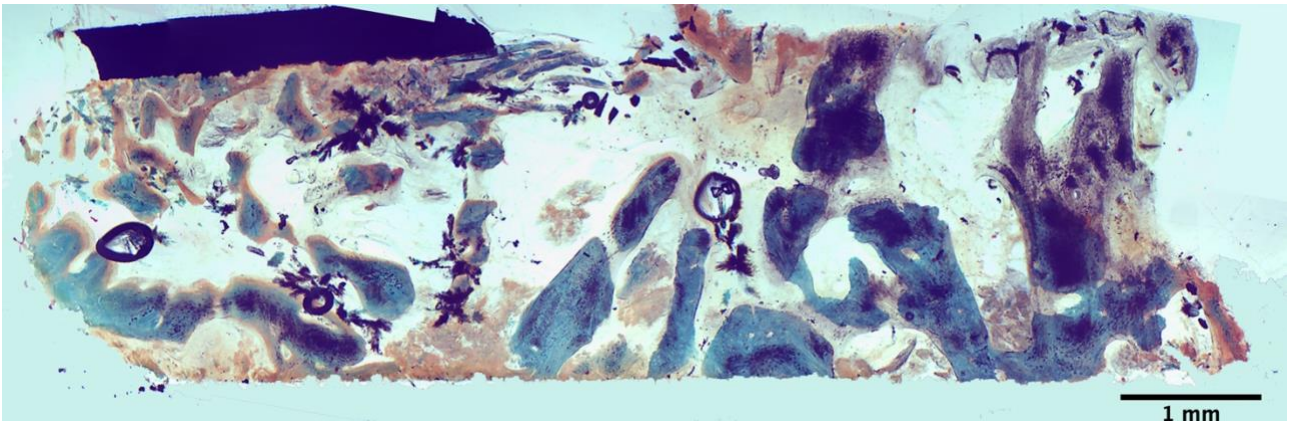

Fig. 82: human bone core biopsy from autologous graft covered by a xenogenic lamina, trichrome Masson stain. Optical microscope, 40x magnification.

	pixel	**area**
total regenerated area	1.879.834	100.00%
soft tissue regenerated area	982.599	52.27%
newly formed bone regenerated area	897.235	46.23%
total graft particles regenerated area	28.139	1.50%

Tab. 5. histomorphometric analysis of bone core biopsy depicted in figure 80.

The trichrome staining highlights, besides the differences of structural separated phases (cancellous bone, marrow spaces and non-mineralized tissue), the non-mineralized bone matrix (orange stain in Fig. 83). The presence of non-mineralized bone matrix (identified as orange stain areas close to pale green ones) is indicative of active bone metabolism. The proximity of these areas with residual bone graft indicates osteoconductivity of the scaffold itself. This histological sequence that anticipate the mineralization, held by osteoblasts, means an active bone physiology according to its prevalence in the sample. This aspect confers a “dynamic” view of the bone sample in which growing bone is detectable.

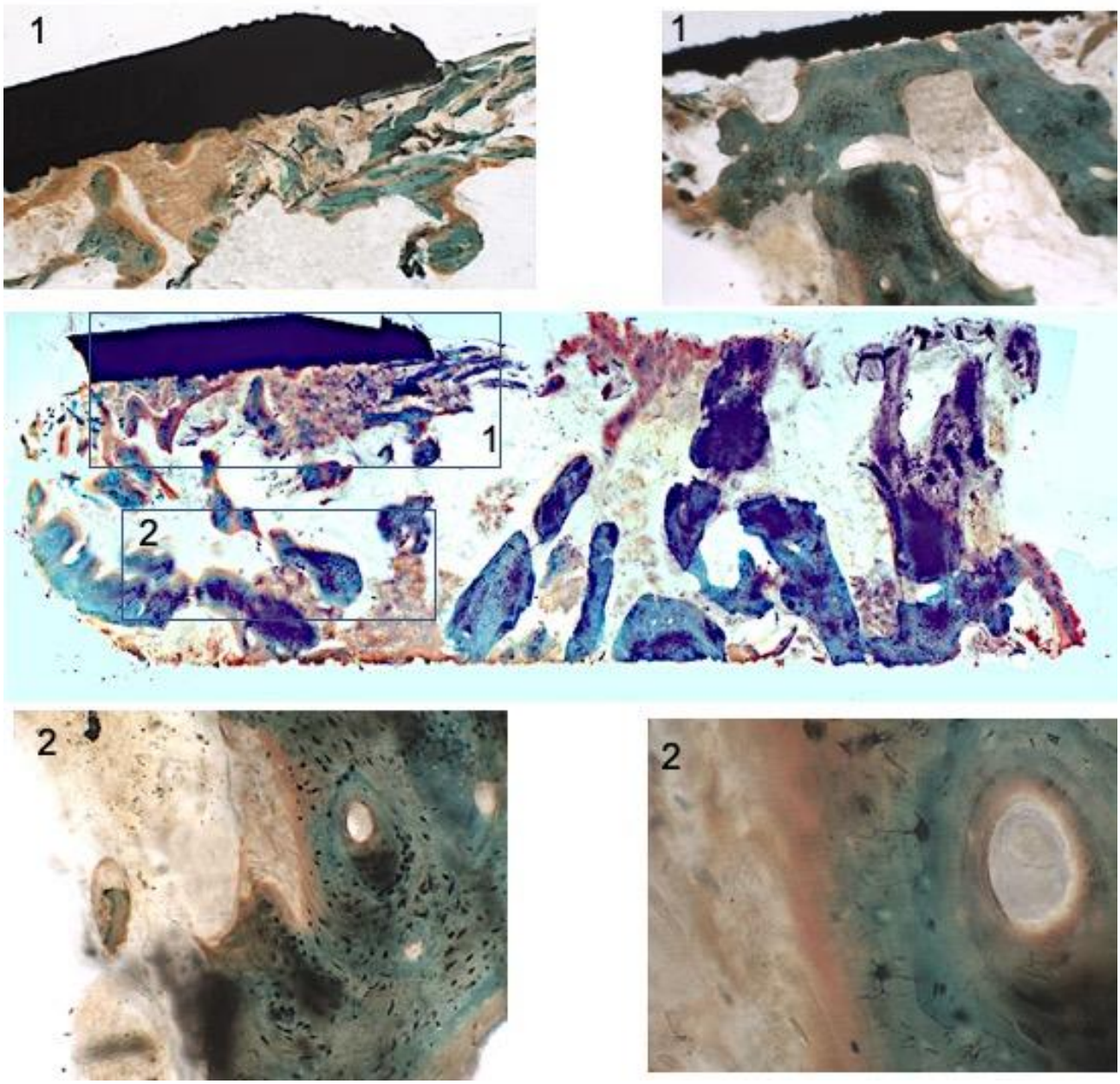

Fig. 83: human bone core biopsy from autologous graft covered by a xenogenic lamina, trichrome Masson stain. Optical microscope, 40x , 100x and 400x magnification. In close-up n.1 are highlighted mineralized bone *trabeculae* in conjunction with non-mineralized bone (orange), while in close-up n. 2 are highlighted haversian channels and osteocytes (black dots). In the right close-up is detectable the interface between marrow space, non-mineralized bone matrix, mineralized lamellar bone with entrapped osteocytes and one haversian channel (from left to right).

Discussion

Electrospun nanofiber membranes in bone regeneration

Nanofiber-based biological matrices exhibit high surface-to-volume ratio, which allows an improved cell adhesion, representing an attractive subgroup of biomaterials due to their unique properties. Among several techniques of nanofiber production, electrospinning is a cost-effective technique that is to date, attractive for several medical applications. For example, in the oral-maxillofacial field, guided bone regeneration is a surgical procedure in which bone regeneration, used to compensate alveolar bone atrophy, is "guided" by an occlusive barrier. The membrane should protect the initial blood clot from any compression, shielding the bone matrix during maturation from infiltration of soft tissues cells with faster proliferation rate.

Ideal membranes for guided bone regeneration should be biocompatible, space making, permeable to fluids but acting as barriers for cells, slowly resorbable, bone promoting and coupled with antimicrobial properties; expectantly not expensive [120]. All the aforementioned properties can be reached starting from electrospun polymers or their mixtures, which result in nanostructured matrices with proper mechanical properties that can eventually be tuned with antimicrobial and bone-promoting compounds. The antimicrobial properties of the herein described PCL-CTL-nAg construct was demonstrated according to the biofilm inhibition assay, in line with the results reported by previous articles on nAg antimicrobial properties [98]. Other compounds have been previously explored to attribute antimicrobial properties to GBR membranes such as the most commonly used agents are represented by amoxicillin [34], metronidazole [35], ciprofloxacin [36] (as antibiotics); polyvinylpyrrolidone [37], silver nanoparticles [30], zinc oxide [38]. Moreover the non-toxicity of the nAg-enriched membranes was tested successfully both with Alamar Blue™ and LDH assay, accordingly to previous papers [97][30]. The antimicrobial activity represents an extremely desirable aspect for a membrane used in oral cavity. This because the plenty of pathogenic species living the oral *milieu* and for the relative high exposure complication rate that affects this surgical procedure [121]. The exposure of the membrane through the full-thickness flap is associated with low success rate of the regenerative procedure [122] because the bacterial could infect both of the membrane and the underlying scaffold used as bone filler. Lian and co-workers developed a bi-layered electrospun membrane with osteogenic and antibacterial properties based on a softer layer of (PLGA)/gelatin nanofibers incorporating dexamethasone-loaded mesoporous silica nanoparticles (DEX@MSNs), and a denser layer of PLGA nanofibers loaded with doxycycline hyclate (DCH). *In vitro* evaluation showed the effective antibacterial potency of the DCH/PLGA

membrane together with an enhanced osteoinductive capacity for rat bone marrow stromal cells (BMSCs) [42]. Moreover, the group of He *et al.* verified the antimicrobial properties and bone formation induction of an electrospun composite membrane made of gelatin (Gln) and chitosan (CS) containing hydroxyapatite nanoparticles (nHAp) and (Pac-525)-loaded PLGA microspheres (AMP@PLGA-MS) [46]. Permeability was successfully tested for a PCL/PLGA electrospun membrane with the fluorescein isothiocyanate-bovine serum albumin (FITC-BSA; Sigma) used as a nutrient model [47]. These two works are explicative of the actual tendency of membrane tailoring for GBR purposes. The extremely favourable surface-to-volume ratio of electrospun membranes [26] could be finely tuned modulating the numerous variables regulating the electrospinning process. Hydrophobic polymers, such as PCL, need to be coupled with volatile but stable solvents, such as the ones used in this work. Moreover, a co-solvent, such as DMF, which favours solvent evaporation, low surface tension, thus producing regular and homogeneous nanofibers in terms of diameter size distribution. A list of all the variables that may affect the shape, dimension, homogeneity of electrospun nanofibers is reported in Tab. 1 [63–65].

The final goal of the process is the fabrication of fibers with diameters at the nanoscale and without the presence of defects (*e.g.* beads, which are the expression of incomplete solvent evaporation). Precise choice of the principal polymer and its adequate solvents should be settled in order to obtain limited surface tension, adequate viscosity and charge density. This has to favour the formation of a continuous flow, which must not collapse in droplets, or beads, after potential difference administration. Both viscosity and surface tension, in conjunction with polymer molecular weight, polymer concentration, conductivity of the solution, influence the fiber morphology and porosity.

Molecular weight depends on the chain length of the polymer and can be related to the entanglements of the molecules. This fact explains why high molecular weight results in viscous solutions compared to low molecular weight. Therefore, the molecular weight of the polymer should be correctly considered for the selection of solvents and concentrations. Indeed, if the solution exhibit too high viscosity, this will hamper the flow through the capillary and the polymer may dry up or drip at the needle tip. Conversely, solutions with relatively low concentration will result into droplets. Solubility and boiling point of the solvent are paramount factors. Volatile solvents are ideal options due to rapid evaporation during the transit from the needle tip to the collector [66]. High boiling points solvents may not evaporate completely prior to hit the target, resulting in flat ribbon shape (Fig. 1) fibers instead of circular fibers, presence of beads or other

defects (Fig. 2) [67]. The volatility of the solvent may affect the final microscopic characteristics of the obtained fibers including porosity, shape and size.

Another important issue, connected to the final use, is the hydrophilicity. Hydrophilicity of the final membrane facilitates cellular adhesion; on the contrary, hydrophobic surface may hamper cellular or bacterial colonization; this effect could be desired in certain circumstances (e.g. outer layer of membranes in guided bone regeneration). Nonetheless, surface hydrophilicity may be easily augmented by means of rapid, reliable and simple techniques such as the air-plasma treatment [123,124]. As reported in chapter 1 of this Thesis, the choice of air-plasma treatment on PCL electrospun membranes reduced significantly the surface tension allowing both *in vivo* tissue adhesion and *in vitro* tunability with bio-promoting agents such as CTL. CTL was chosen as compound to add bio-inducing properties to the pristine PCL membranes accordingly to previous papers [90][98]. Moreover, CTL acts as a stabilizing agent of silver ions in the reductive reaction of silver nitrate. In the present work, CTL demonstrated its ability to improve cell's proliferation when added to the PCL structure. In fact, after 8 days of MG63 cell culture, the PCL-CTL membranes appeared superior in terms of proliferation rate in comparison with PCL and PCL-CTL-nAg. In the latter preparation, the limitation in the proliferation can be correlated to the presence of the silver nanoparticles that may exert a constrained but not neglectable cytotoxic effect. However, biocompatibility of PCL, PCL-CTL and PCL-CTL-nAg membranes has been demonstrated, as reported above and no detrimental effect on the viability of osteoblast-like MG63 cells was detected. Given the fact that in the biological environment degradable electrospun fibers are chemically degraded by enzymes such as lysozyme, it is crucial that the products must be biocompatible [125]. Besides the biological features, the mechanical properties of membranes for GBR are of paramount interest. The most studied electrospun polymers in this field can be classified into natural polymer, synthetic polymer; these can be also used in blends. Nanofibers prepared with synthetic polymers exhibit higher mechanical performances than those based on natural ones. An interesting strategy to ameliorate nanofibers mechanical properties and bioactivity is to combine different synthetic polymers or natural polymers or even to mix natural with synthetic polymers [126]. Some examples of studied polymers are PCL (polycaprolactone) [124], PLA (polylactic acid) [127], PLGA poly(lactic-co-glycolic acid) [25], PTFE (polytetrafluorethylene) [27], alginate [28], hyaluronic acid (HA)[29] chitosan [30], silk fibroin [31], cotton cellulose [32]. The state of the art of commercially available resorbable membranes is nowadays represented by the cross-linked heterologous collagen-based (type I and type III, derived from swine) bilayer membrane Bio Gide® (Geistlich Pharma AG,

Wolhusen, Switzerland); whereas the non-degradable benchmark product is a titanium reinforced expanded polytetrafluoroethylene (ePTFE) membrane named Cytoplast® (Osteogenics Biomedical, Lubbock, USA). Hence, it is evident the paramount difference in terms of technology and fabrication processes between the commercially available membranes and the state of the art of scientific research. The superiority also in mechanical characteristics with the commercially available benchmarks has been previously reported. Billiar *et al.* published an augmented pull-out strength membrane, obtained adding PCL nanofibers to the PLGA/F127 membrane solution. The PCL/PLGA membrane reached almost 8 N in the pull-out test, a result that is comparable with the gold standard Bio-Gide®, and to the benchmark threshold of 2 N (generally accepted for suturing during surgery) [115]. Moreover, when the PCL/PLGA membrane was soaked in saline solution, it showed a higher pull-out strength when compared to the wetted Bio-Gide®, which is more hydrophilic, therefore absorbent [47]. Our PCL-CTL-nAg was tested also in tensile tests with DMA to assess maximum strength and strain, or strain and stress at break, and elastic modulus during dissolution process in SBF. This experiment highlights surprising mechanical properties of the tested membranes up to twenty weeks of aging in simulated body fluid. The durability of a membrane for GBR has to be associated to the space making role during bone matrix mineralization. In fact, these implantable devices have to act as space making and space keeping material (opposing gravity, competitor tissues growth and muscle activity), and to maintain a separation between different cell and tissue types.

Bone regeneration with enriched hemoderivatives

PRF is a one-step standardized method to obtain platelet concentrates (PCs). Through centrifugation of peripheral blood, physiologic clot formation and fractioning are induced without the requirement of other compounds, such as anticoagulants, therefore, PRF represents the only PC system that is fully autologous [128]. Using specific plastic tubes with silica inner covering, the coagulation cascade initiates and activates platelets during centrifugation. The resulting PRF consists of a fibrin scaffold that contains platelets, leukocytes and plasma proteins. After centrifugation, the resulted 3D scaffold of the PRF clot serves as a reservoir of growth factors [111]. Bioactive molecules (growth factor, cytokines, fibronectin, thrombospondin, adhesive proteins) are primarily released from the *alpha* and dense platelet's granules [129]. Moreover, cell interaction between activated platelets and the included leukocytes such as neutrophils, seems to increase the degranulation of inflammatory cytokines (IL-1β, IL-8) and chemokine (MCP-1) [130]. All the aforementioned aspects justify the actual spread of PRF in outpatient procedures. Oral surgery represents one of the most

suitable field of use of PCs because the proven activity towards soft tissues healing [109]. On the other hand, actual evidence on promoting bone regeneration, remains controversial [108]. Actual tendency in scientific clinical research appears, in fact, towards the coupling of PRF with other bone promoting agents such as BMPs, antiresorptive agents (*e.g.* alendronic acid) [59][112]. This literature tendency motivated our experimental approach to implement the standardize protocol for PCs production with a bone promoting agent, with the same producing method. nHAp was chosen as compound for several reasons: the well-established bone promoting action [131][132], the biocompatibility, the hydrophilicity of the molecule and the Ca^{++} content (acting as pro-coagulant). In the first attempt of coupling PRF with nHAp, different mineral concentration were tested without a homogeneous deposition of the crystals on the obtained membranes. Miscibility of the components and moreover, the fractioning process of centrifugation might explain the substandard results. Subsequent attempt foresaw the use of a hydrogel based on alginate/HA already used in the filling of bony defects [133]. This freeze-dried scaffold should have antagonized the centrifugal force during centrifugation, not laying on the bottom of the vial. This result was described in chapter 2. However, the nHAp content was not transferred to the fibrin fiber, or the outer clot surface, as expected. More efforts will be carried out to find the proper technique of enriching the PRF clot with nHAp. Nonetheless, the results of the experiments brought important knowledge about *in vitro* dissolution of PRF membranes, not previously reported. The SBF dissolution assay demonstrated a non-significant alteration of fiber diameter and pores distribution of the tested PRF membranes until day 10. Ideally, the membrane should last at least 12 days to guarantee the biological activity of the incorporated GFs that has been proven to be present *in vitro* until 12 days [111]. Moreover, the uniaxial tensile mechanical test performed on the membranes clearly showed that the resistance is not proportional with the aging in SBF (Figure 53); this is in contrast, with the morphological examination of the membranes that appeared unaltered even after 7 days in SBF. Moreover, the mechanical properties of PRF membranes seem to be not optimal for volume maintenance in bone regenerative procedures. In fact, PRF membranes did not show sufficient mechanical properties to be considered as suitable for GBR technique.

Bone regeneration analysis

Histological and histomorphometric examination of undecalcified bone biopsy specimens is a valuable and well-established clinical and research tool for studying the etiology, pathogenesis, and treatment of metabolic bone diseases. Moreover, in bone regenerative surgery (oral-maxillofacial and orthopedic) it represents a standard method for *in vitro* and *in vivo* studies to assess the

regenerative efficacy of a grafting material or a surgical technique. The histological assessment of bone samples requires the harvesting procedure that is considered invasive. Thus, if not justified by a clinical purpose, the surgical retrieval needs to respect ethical requirements, if the purpose relies on scientific research. This, turned in real life, binds the researcher of finding ethical oriented protocols for the bone specimen harvesting in the clinical research (*e.g.* implant site preparation with trephine bur, or custom-made mini implants as phantoms to be harvested before definitive implant insertion. In any case, the extremely important information brought from histomorphometric analysis is paramount for a complete comprehension of the regenerative behavior of experimental scaffolds. Nonetheless, some Authors suggest the implementation of this analysis with three-dimensional structural evaluation of mineralized tissue by means of µ-CT scans [134,135]. Dias DR *et al.* however failed to demonstrate interchangeability between the two techniques because of the poor agreement between measures obtained by histomorphometry and µCT. Nevertheless, µCT may provide supplementary information to the well-established histomorphometric protocol. Thus, µCT scans, being a non-destructive method for the sample, might be associated to histomorphometry. All the aforementioned arguments explain the efforts in optimizing a histomorphometric laboratory at UniTS. Moreover, the standard protocols have been further optimized. In fact, SEM and the chemical EDS analysis was mentioned only a few times for oral-maxillofacial field [62,136,137]. The absence of standard references in Ca/P ratio or in Ca content in different bone sub-structures requires further investigations to standardize the values and the outcomes related. However, from the articles of Mangano *et al.* [137] imaging with backscattered electrons in the examination of peri-implant bone provided important information regarding the maturation of bone, such that different shades of grey represent different phases of bone deposition, with older bone appearing brighter (*i.e.,* more mineralized) than neo-deposed bone. This characterization appeared more difficult in the histological sections even if, on the other hand, provided useful data for osteointegration process. Moreover, the capability of characterizing chemically the cranio-caudal *ratio* of P/N and Ca/N of the peri-implant bone (meaning the ratio between mineralized and organic components) may highlight the topographic distribution of load on the fixture. Furthermore the organic content may suggest the time of implant insertion according to the findings of Gandolfi and coworkers [62]. Finally, the possibility to directly assess the results of the experiments in the animal model thanks to the histomorphometric analysis facilitates an examination that, nowadays, can be held in University of Trieste and would be otherwise expensive in terms of money and time.

Conclusion and future plans

ELS in producing PCL membranes appears a reliable method, sustained by literature evidence and by the results reported in the present work. The experimental work aimed to find the best combination of variables to produce a nanostructured membrane based on polycaprolactone. The improvement of both antimicrobial properties and bioactivity was allowed by the use of CTL (bioactive molecule) in which nAg can be prepared and included (antimicrobic agent). Qualities such as biocompatibility, bioactivity and antimicrobial activity have been successfully proven *in vitro*. Further *in vivo* studies are needed to understand if the results reached *on bench* might bring advantages also in a clinical setting. On the other side, platelet concentrates, in particular PRF is nowadays a standard technique to obtain an autologous *reservoir* of growth factors able to boost soft tissue healing. The capability of this material of inducing bone regeneration is still a matter of debate. Nonetheless the scientific trend shows great attention to the combination of these derivatives with bone promoting agents. Regrettably, PRF enrichment with nHAp has not shown yet the expected homogeneity with reliable results. Therefore, more efforts will be spent to find out the best set-up to obtain a nHAp-L-PRF membrane. After a morphological and chemical characterization, its potential will be tested *in vitro* and hopefully in an animal model. Finally, the work spent on the optimization of a histomorphometric laboratory has already brought its results, bringing reliability and scientific soundness. This aspect will be of paramount importance in the further investigation of both PRF and PCL membranes. Moreover, the morphological and chemical analyzes of bone through SEM-EDS will give an important tool in the understanding of a nanoscale *milieu* such is the bone-to-implant interface.

References

1. Cima, L.G.; Vacanti, J.P.; Vacanti, C.; Ingber, D.; Mooney, D.; Langer, R. Tissue engineering by cell transplantation using degradable polymer substrates. *J. Biomech. Eng.* **1991**, *113*, 143–151.
2. Salgado, A.J.; Oliveira, J.M.; Martins, A.; Teixeira, F.G.; Silva, N.A.; Neves, N.M.; Sousa, N.; Reis, R.L. Tissue engineering and regenerative medicine: Past, present, and future. *Int. Rev. Neurobiol.* **2013**, *108*, 1–33.
3. Danie Kingsley, J.; Ranjan, S.; Dasgupta, N.; Saha, P. Nanotechnology for tissue engineering: Need, techniques and applications. *J. Pharm. Res.* **2013**, *7*, 200–204.
4. Rho, J.Y.; Kuhn-Spearing, L.; Zioupos, P. Mechanical properties and the hierarchical structure of bone. *Med. Eng. Phys.* **1998**, *20*, 90–102.
5. Reilly, D.T.; Burstein, A.H. The elastic and ultimate properties of compact bone tissue. *J. Biomech.* **1975**, *8*, 393–405.
6. Misch, C.E.; Qu, Z.; Bidez, M.W. Mechanical properties of trabecular bone in the human mandible: Implications for dental implant treatment planning and surgical placement. *J. Oral Maxillofac. Surg.* **1999**, *57*, 700–706.
7. Dohan, D.M.; Choukroun, J.; Diss, A.; Dohan, S.L.; Dohan, A.J.J.; Mouhyi, J.; Gogly, B. Platelet-rich fibrin (PRF): A second-generation platelet concentrate. Part I: Technological concepts and evolution. *Oral Surgery, Oral Med. Oral Pathol. Oral Radiol. Endodontology* **2006**, *101*, 37–44.
8. Ma, P.X. Scaffolds for tissue fabrication. *Mater. Today* **2004**, *7*, 30–40.
9. Zhang, L.; Webster, T.J. Nanotechnology and nanomaterials: Promises for improved tissue regeneration. *Nano Today* 2009, *4*, 66–80.
10. Rahman, S.U.; Oh, J.H.; Cho, Y.D.; Chung, S.H.; Lee, G.; Baek, J.H.; Ryoo, H.M.; Woo, K.M. Fibrous Topography-Potentiated Canonical Wnt Signaling Directs the Odontoblastic Differentiation of Dental Pulp-Derived Stem Cells. *ACS Appl. Mater. Interfaces* **2018**, *10*, 17526–17541.
11. Smith, L.A.; Ma, P.X. Nano-fibrous scaffolds for tissue engineering. *Colloids Surfaces B Biointerfaces* **2004**, *39*, 125–131.
12. Niece, K.L.; Hartgerink, J.D.; Donners, J.J.J.M.; Stupp, S.I. Self-assembly combining two bioactive peptide-amphiphile molecules into nanofibers by electrostatic attraction. *J. Am. Chem. Soc.* **2003**, *125*, 7146–7147.
13. Martin, C.R. Template Synthesis of Electronically Conductive Polymer Nanostructures. *Acc. Chem. Res.* **1995**, *28*, 61–68.
14. Greiner, A.; Wendorff, J.H. Electrospinning: A fascinating method for the preparation of ultrathin fibers. *Angew. Chemie - Int. Ed.* **2007**, *46*, 5670–5703.
15. Jordan, A.M.; Viswanath, V.; Kim, S.E.; Pokorski, J.K.; Korley, L.T.J. Processing and surface modification of polymer nanofibers for biological scaffolds: A review. *J. Mater. Chem. B* **2016**, *36*, 5958–5974.
16. Matthews, J.A.; Wnek, G.E.; Simpson, D.G.; Bowlin, G.L. Electrospinning of collagen nanofibers. *Biomacromolecules* **2002**, *3*, 232–238.
17. Samprasit, W.; Kaomongkolgit, R.; Sukma, M.; Rojanarata, T.; Ngawhirunpat, T.; Opanasopit, P. Mucoadhesive electrospun chitosan-based nanofibre mats for dental caries prevention. *Carbohydr. Polym.* **2015**, *117*, 933–940.
18. Borges, A.L.S.; Münchow, E.A.; de Oliveira Souza, A.C.; Yoshida, T.; Vallittu, P.K.; Bottino, M.C. Effect of random/aligned nylon-6/MWCNT fibers on dental resin composite reinforcement. *J. Mech. Behav. Biomed. Mater.* **2015**, *48*, 134–144.
19. Ravichandran, R.; Ng, C.C.H.; Liao, S.; Pliszka, D.; Raghunath, M.; Ramakrishna, S.; Chan, C.K.

Biomimetic surface modification of titanium surfaces for early cell capture by advanced electrospinning. *Biomed. Mater.* **2012**, *7*, 015001.

20. Noh, H.K.; Lee, S.W.; Kim, J.M.; Oh, J.E.; Kim, K.H.; Chung, C.P.; Choi, S.C.; Park, W.H.; Min, B.M. Electrospinning of chitin nanofibers: Degradation behavior and cellular response to normal human keratinocytes and fibroblasts. *Biomaterials* **2006**, *27*, 3934–3944.
21. Verreck, G.; Chun, I.; Peeters, J.; Rosenblatt, J.; Brewster, M.E. Preparation and characterization of nanofibers containing amorphous drug dispersions generated by electrostatic spinning. *Pharm. Res.* **2003**, *20*, 810–817.
22. Rampichová, M.; Chvojka, J.; Jenčová, V.; Kubíková, T.; Tonar, Z.; Erben, J.; Buzgo, M.; Daňková, J.; Litvinec, A.; Vocetková, K.; et al. The combination of nanofibrous and microfibrous materials for enhancement of cell infiltration and in vivo bone tissue formation. *Biomed. Mater.* **2018**, *13*, 025004.
23. Bottino, M.C.; Thomas, V.; Schmidt, G.; Vohra, Y.K.; Chu, T.M.G.; Kowolik, M.J.; Janowski, G.M. Recent advances in the development of GTR/GBR membranes for periodontal regeneration - A materials perspective. *Dent. Mater.* **2012**, *28*, 703–721.
24. Rakhmatia, Y.D.; Ayukawa, Y.; Furuhashi, A.; Koyano, K. Current barrier membranes: Titanium mesh and other membranes for guided bone regeneration in dental applications. *J. Prosthodont. Res.* **2013**, *57*, 3–14.
25. Cai, X.; ten Hoopen, S.; Zhang, W.; Yi, C.; Yang, W.; Yang, F.; Jansen, J.A.; Walboomers, X.F.; Yelick, P.C. Influence of highly porous electrospun PLGA/PCL/nHA fibrous scaffolds on the differentiation of tooth bud cells in vitro. *J. Biomed. Mater. Res. - Part A* **2017**, *105*, 2597–2607.
26. Eichhorn, S.J.; Sampson, W.W. Statistical geometry of pores and statistics of porous nanofibrous assemblies. *J. R. Soc. Interface* **2005**, *2*, 309–318.
27. Park, J.Y.; Lee, J.H.; Kim, C.H.; Kim, Y.J. Fabrication of polytetrafluoroethylene nanofibrous membranes for guided bone regeneration. *RSC Adv.* **2018**, *8*, 34359–34369.
28. Hokmabad, V.R.; Davaran, S.; Aghazadeh, M.; Rahbarghazi, R.; Salehi, R.; Ramazani, A. Fabrication and characterization of novel ethyl cellulose-grafted-poly (ε-caprolactone)/alginate nanofibrous/macroporous scaffolds incorporated with nano-hydroxyapatite for bone tissue engineering. *J. Biomater. Appl.* **2019**, *33*, 1128–1144.
29. Vicini, S.; Mauri, M.; Vita, S.; Castellano, M. Alginate and alginate/hyaluronic acid membranes generated by electrospinning in wet conditions: Relationship between solution viscosity and spinnability. *J. Appl. Polym. Sci.* **2018**.
30. Lee, D.; Lee, S.J.; Moon, J.H.; Kim, J.H.; Heo, D.N.; Bang, J.B.; Lim, H.N.; Kwon, I.K. Preparation of antibacterial chitosan membranes containing silver nanoparticles for dental barrier membrane applications. *J. Ind. Eng. Chem.* **2018**, *66*, 196–202.
31. Türkkan, S.; Pazarçeviren, A.E.; Keskin, D.; Machin, N.E.; Duygulu, Ö.; Tezcaner, A. Nanosized CaP-silk fibroin-PCL-PEG-PCL/PCL based bilayer membranes for guided bone regeneration. *Mater. Sci. Eng. C* **2017**, *80*, 484–493.
32. He, X.; Cheng, L.; Zhang, X.; Xiao, Q.; Zhang, W.; Lu, C. Tissue engineering scaffolds electrospun from cotton cellulose. *Carbohydr. Polym.* **2015**, *115*, 485–493.
33. Dodiuk-Kenig, H.; Lizenboim, K.; Roth, S.; Zalsman, B.; McHale, W.A.; Jaffe, M.; Griswold, K. Performance enhancement of dental composites using electrospun nanofibers. *J. Nanomater.* **2008**, *2008*, 1–6.
34. Topsakal, A.; Uzun, M.; Ugar, G.; Ozcan, A.; Altun, E.; Oktar, F.N.; Ikram, F.; Ozkan, O.; Turkoglu Sasmazel, H.; Gunduz, O. Development of amoxicillin-loaded electrospun polyurethane/Chitosan/β-tricalcium phosphate scaffold for bone tissue regeneration. *IEEE Trans. Nanobioscience* **2018**, *17*, 321–328.

35. He, M.; Jiang, H.; Wang, R.; Xie, Y.; Zhao, C. Fabrication of metronidazole loaded poly (ε-caprolactone)/zein core/shell nanofiber membranes via coaxial electrospinning for guided tissue regeneration. *J. Colloid Interface Sci.* **2017**, *490*, 270–278.
36. Wright, M.E.E.; Wong, A.T.; Levitt, D.; Parrag, I.C.; Yang, M.; Santerre, J.P. Influence of ciprofloxacin-based additives on the hydrolysis of nanofiber polyurethane membranes. *J. Biomed. Mater. Res. - Part A* **2018**, *106*, 1211–1222.
37. Karayegen, G.; Koçum, I.C.; Çökeliler Serdaroglu, D.; Dogan, M. Aligned polyvinylpyrrolidone nanofibers with advanced electrospinning for biomedical applications. *Biomed. Mater. Eng.* **2018**, *29*, 685–697.
38. Nasajpour, A.; Ansari, S.; Rinoldi, C.; Rad, A.S.; Aghaloo, T.; Shin, S.R.; Mishra, Y.K.; Adelung, R.; Swieszkowski, W.; Annabi, N.; et al. A Multifunctional Polymeric Periodontal Membrane with Osteogenic and Antibacterial Characteristics. *Adv. Funct. Mater.* **2018**, *28*, 1703437.
39. da Silva, T.N.; Gonçalves, R.P.; Rocha, C.L.; Archanjo, B.S.; Barboza, C.A.G.; Pierre, M.B.R.; Reynaud, F.; de Souza Picciani, P.H. Controlling burst effect with PLA/PVA coaxial electrospun scaffolds loaded with BMP-2 for bone guided regeneration. *Mater. Sci. Eng. C* **2019**, *97*, 602–612.
40. Polini, A.; Petre, D.G.; Iafisco, M.; de Lacerda Schickert, S.; Tampieri, A.; van den Beucken, J.; Leeuwenburgh, S.C.G. Polyester fibers can be rendered calcium phosphate-binding by surface functionalization with bisphosphonate groups. *J. Biomed. Mater. Res. - Part A* **2017**, *105*, 2335–2342.
41. Ji, Y.; Wang, L.; Watts, D.C.; Qiu, H.; You, T.; Deng, F.; Wu, X. Controlled-release naringin nanoscaffold for osteoporotic bone healing. *Dent. Mater.* **2014**, *30*, 1263–1273.
42. Lian, M.; Sun, B.; Qiao, Z.; Zhao, K.; Zhou, X.; Zhang, Q.; Zou, D.; He, C.; Zhang, X. Bi-layered electrospun nanofibrous membrane with osteogenic and antibacterial properties for guided bone regeneration. *Colloids Surfaces B Biointerfaces* **2019**, *176*, 219–229.
43. Tang, Y.; Chen, L.; Zhao, K.; Wu, Z.; Wang, Y.; Tan, Q. Fabrication of PLGA/HA (core)-collagen/amoxicillin (shell) nanofiber membranes through coaxial electrospinning for guided tissue regeneration. *Compos. Sci. Technol.* **2016**, *125*, 100–107.
44. Stewart, S.A.; Domínguez-Robles, J.; Donnelly, R.F.; Larrañeta, E. Implantable polymeric drug delivery devices: Classification, manufacture, materials, and clinical applications. *Polymers (Basel).* **2018**, *10*, 1379.
45. Persenaire, O.; Alexandre, M.; Degée, P.; Dubois, P. Mechanisms and kinetics of thermal degradation of poly(ε-caprolactone). *Biomacromolecules* **2001**, *2*, 288–294.
46. He, Y.; Jin, Y.; Wang, X.; Yao, S.; Li, Y.; Wu, Q.; Ma, G.; Cui, F.; Liu, H. An Antimicrobial Peptide-Loaded Gelatin/Chitosan Nanofibrous Membrane Fabricated by Sequential Layer-by-Layer Electrospinning and Electrospraying Techniques. *Nanomaterials* **2018**, *8*, 327.
47. Cho, W.J.; Kim, J.H.; Oh, S.H.; Nam, H.H.; Kim, J.M.; Lee, J.H. Hydrophilized polycaprolactone nanofiber mesh-embedded poly(glycolic- co -lactic acid) membrane for effective guided bone regeneration. *J. Biomed. Mater. Res. Part A* **2008**, *91A*, 400–407.
48. Oh, S.H.; Kim, J.H.; Kim, J.M.; Lee, J.H. Asymmetrically porous PLGA/Pluronic F127 membrane for effective guided bone regeneration. *J. Biomater. Sci. Polym. Ed.* **2006**, *17*, 1375–1387.
49. Bhattarai, D.P.; Aguilar, L.E.; Park, C.H.; Kim, C.S. A review on properties of natural and synthetic based electrospun fibrous materials for bone tissue engineering. *Membranes (Basel).* **2018**, *8*, 62.
50. Sam, G.; Vadakkekuttical, R.J.; Amol, N.V. In vitro evaluation of mechanical properties of platelet-rich fibrin membrane and scanning electron microscopic examination of its surface characteristics. *J. Indian Soc. Periodontol.* **2015**, *19*, 32–36.
51. Ross, R.; Glomset, J.; Kariya, B.; Harker, L. A platelet dependent serum factor that stimulates

the proliferation of arterial smooth muscle cells in vitro. *Proc. Natl. Acad. Sci. U. S. A.* **1974**, *71*, 1207–1210.
52. Gassling, V.; Douglas, T.; Warnke, P.H.; Açil, Y.; Wiltfang, J.; Becker, S.T. Platelet-rich fibrin membranes as scaffolds for periosteal tissue engineering. *Clin. Oral Implants Res.* **2010**, *21*, 543–549.
53. Soffer, E.; Ouhayoun, J.P.; Anagnostou, F. Fibrin sealants and platelet preparations in bone and periodontal healing. *Oral Surg. Oral Med. Oral Pathol. Oral Radiol. Endod.* **2003**, *95*, 521–528.
54. Nevins, M.; Giannobile, W. V.; McGuire, M.K.; Kao, R.T.; Mellonig, J.T.; Hinrichs, J.E.; McAllister, B.S.; Murphy, K.S.; McClain, P.K.; Nevins, M.L.; et al. Platelet-Derived Growth Factor Stimulates Bone Fill and Rate of Attachment Level Gain: Results of a Large Multicenter Randomized Controlled Trial. *J. Periodontol.* **2005**, *76*, 2205–2215.
55. Simonpieri, A.; Del Corso, M.; Sammartino, G.; Ehrenfest, D.M.D. The Relevance of Choukroun's Platelet- Rich Fibrin and Metronidazole During Complex Maxillary Rehabilitations Using. Bone Allograft. Part I: A New Grafting Protocol. *Implant Dent.* **2009**, *18*, 102–11.
56. Lourenço, E.S.; Mourão, C.F. de A.B.; Leite, P.E.C.; Granjeiro, J.M.; Calasans-Maia, M.D.; Alves, G.G. The in vitro release of cytokines and growth factors from fibrin membranes produced through horizontal centrifugation. *J. Biomed. Mater. Res. - Part A* **2018**, *106*, 1373–1380.
57. Khorshidi, H.; Raoofi, S.; Bagheri, R.; Banihashemi, H. Comparison of the Mechanical Properties of Early Leukocyte-and Platelet-Rich Fibrin versus PRGF/Endoret Membranes. *Int. J. Dent.* **2016**, *2016*, 1849207.
58. Mendoza-Azpur, G.; Olaechea, A.; Padial-Molina, M.; Gutiérrez-Garrido, L.; O'Valle, F.; Mesa, F.; Galindo-Moreno, P. Composite Alloplastic Biomaterial vs. Autologous Platelet-Rich Fibrin in Ridge Preservation. *J. Clin. Med.* **2019**, *8*, 223.
59. Li, F.; Jiang, P.; Pan, J.; Liu, C.; Zheng, L. Synergistic Application of Platelet-Rich Fibrin and 1% Alendronate in Periodontal Bone Regeneration: A Meta-Analysis. *Biomed Res. Int.* **2019**.
60. do Lago, E.S.; Ferreira, S.; Garcia, I.R.; Okamoto, R.; Mariano, R.C. Improvement of bone repair with l-PRF and bovine bone in calvaria of rats. histometric and immunohistochemical study. *Clin. Oral Investig.* **2019**.
61. Karayürek, F.; Kadiroğlu, E.T.; Nergiz, Y.; Coşkun Akçay, N.; Tunik, S.; Ersöz Kanay, B.; Uysal, E. Combining platelet rich fibrin with different bone graft materials: An experimental study on the histopathological and immunohistochemical aspects of bone healing. *J. Cranio-Maxillofacial Surg.* **2019**.
62. Gandolfi, M.; Zamparini, F.; Iezzi, G.; Degidi, M.; Botticelli, D.; Piattelli, A.; Prati, C. Microchemical and Micromorphologic ESEM-EDX Analysis of Bone Mineralization at the Thread Interface in Human Dental Implants Retrieved for Mechanical Complications After 2 Months to 17 Years. *Int. J. Periodontics Restorative Dent.* **2018**, *38*, 431–441.
63. Deitzel, J.M.; Kleinmeyer, J.; Harris, D.; Beck Tan, N.C. The effect of processing variables on the morphology of electrospun nanofibers and textiles. *Polymer (Guildf).* **2001**, *2*, 261–272.
64. Bhardwaj, N.; Kundu, S.C. Electrospinning: A fascinating fiber fabrication technique. *Biotechnol. Adv.* **2010**, *28*, 325–347.
65. Zafar, M.; Najeeb, S.; Khurshid, Z.; Vazirzadeh, M.; Zohaib, S.; Najeeb, B.; Sefat, F. Potential of electrospun nanofibers for biomedical and dental applications. *Materials (Basel).* **2016**, *9*, 73.
66. Pillay, V.; Dott, C.; Choonara, Y.E.; Tyagi, C.; Tomar, L.; Kumar, P.; du Toit, L.C.; Ndesendo, V.M.K. A Review of the Effect of Processing Variables on the Fabrication of Electrospun Nanofibers for Drug Delivery Applications. *J. Nanomater.* **2013**, *2013*, 1–22.
67. Lannutti, J.; Reneker, D.; Ma, T.; Tomasko, D.; Farson, D. Electrospinning for tissue

engineering scaffolds. *Mater. Sci. Eng. C* **2007**, *27*, 504–509.
68. Zhang, Y.Z.; Feng, Y.; Huang, Z.M.; Ramakrishna, S.; Lim, C.T. Fabrication of porous electrospun nanofibres. *Nanotechnology* **2006**, *17*, 3.
69. Liu, Z.; Li, X.; Yang, Y.; Zhang, K.; Wang, X.; Zhu, M.; Hsiao, B.S. Control of structure and morphology of highly aligned PLLA ultrafine fibers via linear-jet electrospinning. *Polymer (Guildf).* **2019**, *20*, 2455.
70. Pai, C.L.; Boyce, M.C.; Rutledge, G.C. Morphology of porous and wrinkled fibers of polystyrene electrospun from dimethylformamide. *Macromolecules* **2009**, *42*, 2102–2114.
71. Haider, A.; Haider, S.; Kang, I.K. A comprehensive review summarizing the effect of electrospinning parameters and potential applications of nanofibers in biomedical and biotechnology. *Arab. J. Chem.* **2018**, *11*, 1165–1188.
72. Figueira, D.R.; Miguel, S.P.; de Sá, K.D.; Correia, I.J. Production and characterization of polycaprolactone- hyaluronic acid/chitosan- zein electrospun bilayer nanofibrous membrane for tissue regeneration. *Int. J. Biol. Macromol.* **2016**, *93*, 1100–1110.
73. Shao, J.; Yu, N.; Kolwijck, E.; Wang, B.; Tan, K.W.; Jansen, J.A.; Walboomers, X.F.; Yang, F. Biological evaluation of silver nanoparticles incorporated into chitosan-based membranes. *Nanomedicine* **2017**, *12*, 2771–2785.
74. Sibaja, B.; Culbertson, E.; Marshall, P.; Boy, R.; Broughton, R.M.; Solano, A.A.; Esquivel, M.; Parker, J.; Fuente, L.D. La; Auad, M.L. Preparation of alginate-chitosan fibers with potential biomedical applications. *Carbohydr. Polym.* **2015**, *4*, 1457–1465.
75. Yuan, X.Y.; Zhang, Y.Y.; Dong, C.; Sheng, J. Morphology of ultrafine polysulfone fibers prepared by electrospinning. *Polym. Int.* **2004**.
76. Zhou, T.; Yao, Y.; Xiang, R.; Wu, Y. Formation and characterization of polytetrafluoroethylene nanofiber membranes for vacuum membrane distillation. *J. Memb. Sci.* **2014**, *453*, 402–408.
77. Megelski, S.; Stephens, J.S.; Bruce Chase, D.; Rabolt, J.F. Micro- and nanostructured surface morphology on electrospun polymer fibers. *Macromolecules* **2002**, *35*, 8456–8466.
78. Zuo, W.; Zhu, M.; Yang, W.; Yu, H.; Chen, Y.; Zhang, Y. Experimental study on relationship between jet instability and formation of beaded fibers during electrospinning. *Polym. Eng. Sci.* **2005**, *45*, 704–709.
79. Wannatong, L.; Sirivat, A.; Supaphol, P. Effects of solvents on electrospun polymeric fibers: Preliminary study on polystyrene. *Polym. Int.* **2004**, *53*, 1851–1859.
80. Baumgarten, P.K. Electrostatic spinning of acrylic microfibers. *J. Colloid Interface Sci.* **1971**, *36*, 71–79.
81. Haghi, A.K.; Akbari, M. Trends in electrospinning of natural nanofibers. *Phys. Status Solidi Appl. Mater. Sci.* **2007**, *204*, 1830–1834.
82. Fong, H.; Chun, I.; Reneker, D.H. Beaded nanofibers formed during electrospinning. *Polymer (Guildf).* **1999**, *40*, 4585–4592.
83. Huang, L.; Nagapudi, K.; Apkarian, P.R.; Chaikof, E.L. Engineered collagen - PEO nanofibers and fabrics. *J. Biomater. Sci. Polym. Ed.* **2001**, *12*, 979–993.
84. Zhang, C.; Yuan, X.; Wu, L.; Han, Y.; Sheng, J. Study on morphology of electrospun poly(vinyl alcohol) mats. *Eur. Polym. J.* **2005**, *41*, 423–432.
85. Kim, B.; Park, H.; Lee, S.H.; Sigmund, W.M. Poly(acrylic acid) nanofibers by electrospinning. *Mater. Lett.* **2005**, *59*, 829–832.
86. Mit-Uppatham, C.; Nithitanakul, M.; Supaphol, P. Ultrafine electrospun polyamide-6 fibers: Effect of solution conditions on morphology and average fiber diameter. *Macromol. Chem. Phys.* **2004**, *205*, 2327–2338.
87. Casper, C.L.; Stephens, J.S.; Tassi, N.G.; Chase, D.B.; Rabolt, J.F. Controlling surface morphology of electrospun polystyrene fibers: Effect of humidity and molecular weight in the

electrospinning process. *Macromolecules* **2004**, *37*, 573–578.
88. Schiffman, J.D.; Schauer, C.L. A review: Electrospinning of biopolymer nanofibers and their applications. *Polym. Rev.* **2008**, *48*, 317–352.
89. Taylor, G.I. Disintegration of water drops in an electric field. *Proc. R. Soc. A Math. Phys. Eng. Sci.* **1964**, *280*, 383–397.
90. Donati, I.; Stredanska, S.; Silvestrini, G.; Vetere, A.; Marcon, P.; Marsich, E.; Mozetic, P.; Gamini, A.; Paoletti, S.; Vittur, F. The aggregation of pig articular chondrocyte and synthesis of extracellular matrix by a lactose-modified chitosan. *Biomaterials* **2005**, *26*, 987–998.
91. Schindelin, J.; Arganda-Carreras, I.; Frise, E.; Kaynig, V.; Longair, M.; Pietzsch, T.; Preibisch, S.; Rueden, C.; Saalfeld, S.; Schmid, B.; et al. Fiji: An open-source platform for biological-image analysis. *Nat. Methods* **2012**, *9*, 676.
92. Nhi, T.T.; Khon, H.C.; Hoai, N.T.T.; Bao, B.C.; Quyen, T.N.; Van Toi, V.; Hiep, N.T. Fabrication of electrospun polycaprolactone coated withchitosan-silver nanoparticles membranes for wound dressing applications. *J. Mater. Sci. Mater. Med.* **2016**, *27*, 5768–5774.
93. Du, L.; Xu, H.; Zhang, Y.; Zou, F. Electrospinning of polycaprolatone nanofibers with DMF additive: The effect of solution proprieties on jet perturbation and fiber morphologies. *Fibers Polym.* **2016**, *17*, 751–759.
94. Valence, S. De; Tille, J.C.; Chaabane, C.; Gurny, R.; Bochaton-Piallat, M.L.; Walpoth, B.H.; Möller, M. Plasma treatment for improving cell biocompatibility of a biodegradable polymer scaffold for vascular graft applications. *Eur. J. Pharm. Biopharm.* **2013**, *85*, 78–86.
95. Can-Herrera, L.A.; Ávila-Ortega, A.; de la Rosa-García, S.; Oliva, A.I.; Cauich-Rodríguez, J. V.; Cervantes-Uc, J.M. Surface modification of electrospun polycaprolactone microfibers by air plasma treatment: Effect of plasma power and treatment time. *Eur. Polym. J.* **2016**, *84*, 502–516.
96. Yildirim, E.D.; Pappas, D.; Güçeri, S.; Sun, W. Enhanced cellular functions on polycaprolactone tissue scaffolds by o 2 plasma surface modification. *Plasma Process. Polym.* **2011**, *8*, 256–267.
97. Travan, A.; Pelillo, C.; Donati, I.; Marsich, E.; Benincasa, M.; Scarpa, T.; Semeraro, S.; Turco, G.; Gennaro, R.; Paoletti, S. Non-cytotoxic silver nanoparticle-polysaccharide nanocomposites with antimicrobial activity. *Biomacromolecules* **2009**, *10*, 1429–35.
98. Marsich, E.; Travan, A.; Donati, I.; Turco, G.; Kulkova, J.; Moritz, N.; Aro, H.T.; Crosera, M.; Paoletti, S. Biological responses of silver-coated thermosets: An in vitro and in vivo study. *Acta Biomater.* **2013**, *9*, 5088–5099.
99. Feng, Q.L.; Wu, J.; Chen, G.Q.; Cui, F.Z.; Kim, T.N.; Kim, J.O. A mechanistic study of the antibacterial effect of silver ions on Escherichia coli and Staphylococcus aureus. *J. Biomed. Mater. Res.* **2000**, *52*, 662–668.
100. Morones, J.R.; Elechiguerra, J.L.; Camacho, A.; Holt, K.; Kouri, J.B.; Ramírez, J.T.; Yacaman, M.J. The bactericidal effect of silver nanoparticles. *Nanotechnology* **2005**, *16*, 2346–2353.
101. Clement, J.L.; Jarrett, P.S. Antibacterial Silver. *Met. Based. Drugs* **1994**, *1*, 467–482.
102. Pham, Q.P.; Sharma, U.; Mikos, A.G. Electrospun poly (ε-caprolactone) microfiber and multilayer nanofiber/microfiber scaffolds: Characterization of scaffolds and measurement of cellular infiltration. *Biomacromolecules* **2006**, *7*, 2796–2805.
103. Shin, M.; Yoshimoto, H.; Vacanti, J.P. In Vivo Bone Tissue Engineering Using Mesenchymal Stem Cells on a Novel Electrospun Nanofibrous Scaffold. *Tissue Eng.* **2004**, *10*, 33–41.
104. Miron, R.J.; Zucchelli, G.; Pikos, M.A.; Salama, M.; Lee, S.; Guillemette, V.; Fujioka-Kobayashi, M.; Bishara, M.; Zhang, Y.; Wang, H.L.; et al. Use of platelet-rich fibrin in regenerative dentistry: a systematic review. *Clin. Oral Investig.* **2017**, *21*, 1913–1927.
105. Moraschini, V.; Barboza, E. dos S.P. Use of Platelet-Rich Fibrin Membrane in the Treatment of Gingival Recession: A Systematic Review and Meta-Analysis. *J. Periodontol.* **2016**, *87*, 281–

290.
106. Femminella, B.; Iaconi, M.C.; Di Tullio, M.; Romano, L.; Sinjari, B.; D'Arcangelo, C.; De Ninis, P.; Paolantonio, M. Clinical Comparison of Platelet-Rich Fibrin and a Gelatin Sponge in the Management of Palatal Wounds After Epithelialized Free Gingival Graft Harvest: A Randomized Clinical Trial. *J. Periodontol.* **2016**, *87*, 103–113.
107. Jankovic, S.; Aleksic, Z.; Klokkevold, P.; Lekovic, V.; Dimitrijevic, B.; Kenney, E.B.; Camargo, P. Use of platelet-rich fibrin membrane following treatment of gingival recession: a randomized clinical trial. *Int. J. Periodontics Restorative Dent.* **2012**, *32*, 41–50.
108. Ghanaati, S.; Herrera-Vizcaino, C.; Al-Maawi, S.; Lorenz, J.; Miron, R.J.; Nelson, K.; Schwarz, F.; Choukroun, J.; Sader, R. Fifteen years of platelet rich fibrin in dentistry and oromaxillofacial surgery: How high is the level of scientific evidence? *J. Oral Implantol.* **2018**, *44*, 471–492.
109. Miron, R.J.; Fujioka-Kobayashi, M.; Bishara, M.; Zhang, Y.; Hernandez, M.; Choukroun, J. Platelet-Rich Fibrin and Soft Tissue Wound Healing: A Systematic Review. *Tissue Eng. - Part B Rev.* **2017**, *23*, 83–99.
110. Owen, C.A.; Campbell, E.J. The cell biology of leukocyte-mediated proteolysis. *J. Leukoc. Biol.* **1999**, *65*, 137–150.
111. Fujioka-Kobayashi, M.; Miron, R.J.; Hernandez, M.; Kandalam, U.; Zhang, Y.; Choukroun, J. Optimized Platelet-Rich Fibrin With the Low-Speed Concept: Growth Factor Release, Biocompatibility, and Cellular Response. *J Periodontol* **2017**, *88*, 112–121.
112. Miron, R.J.; Zhang, Y. Autologous liquid platelet rich fibrin: A novel drug delivery system. *Acta Biomater.* **2018**, *75*, 35–51.
113. Kuo, T.F.; Lin, M.F.; Lin, Y.H.; Lin, Y.C.; Su, R.J.; Lin, H.W.; Chan, W.P. Implantation of platelet-rich fibrin and cartilage granules facilitates cartilage repair in the injured rabbit knee: Preliminary report. *Clinics* **2011**, *66*, 1835–1838.
114. Ji, W.; Wang, H.; van den Beucken, J.J.J.P.; Yang, F.; Walboomers, X.F.; Leeuwenburgh, S.; Jansen, J.A. Local delivery of small and large biomolecules in craniomaxillofacial bone. *Adv. Drug Deliv. Rev.* **2012**, *64*, 1152–1164.
115. Billiar, K.; Murray, J.; Laude, D.; Abraham, G.; Bachrach, N. Effects of carbodiimide crosslinking conditions on the physical properties of laminated intestinal submucosa. *J. Biomed. Mater. Res.* **2001**.
116. Dempster, D.W.; Compston, J.E.; Drezner, M.K.; Glorieux, F.H.; Kanis, J.A.; Malluche, H.; Meunier, P.J.; Ott, S.M.; Recker, R.R.; Parfitt, A.M. Standardized nomenclature, symbols, and units for bone histomorphometry: A 2012 update of the report of the ASBMR Histomorphometry Nomenclature Committee. *J. Bone Miner. Res.* **2013**, *28*, 1–16.
117. Iezzi, G.; Piattelli, A.; Giuliani, A.; Mangano, C.; Barone, A.; Manzon, L.; Degidi, M.; Scarano, A.; Filippone, A.; Perrotti, V. Molecular, Cellular and Pharmaceutical Aspects of Bone Grafting Materials and Membranes During Maxillary Sinus-lift Procedures. Part 2: Detailed Characteristics of the Materials. *Curr. Pharm. Biotechnol.* **2016**, *18*, 33–44.
118. Ketteler, M.; Block, G.A.; Evenepoel, P.; Fukagawa, M.; Herzog, C.A.; McCann, L.; Moe, S.M.; Shroff, R.; Tonelli, M.A.; Toussaint, N.D.; et al. Executive summary of the 2017 KDIGO Chronic Kidney Disease–Mineral and Bone Disorder (CKD-MBD) Guideline Update: what's changed and why it matters. *Kidney Int.* **2017**, *92*, 26–36.
119. Stacchi, C.; Berton, F.; Fiorillo, L.; Nicolin, V.; Lombardi, T.; Cicciù, M.; Di Lenarda, R. Fresh frozen allogeneic bone block in maxillary sinus floor elevation: Histomorphometric analysis of a bone specimen retrieved 15 years after grafting procedure. *Appl. Sci.* **2019**, *9*, 1119.
120. Aukhil, I.; Pettersson, E.; Suggs, C. Guided Tissue Regeneration: An Experimental Procedure in Beagle Dogs. *J. Periodontol.* **1986**, *57*, 727–34.
121. Cucchi, A.; Vignudelli, E.; Napolitano, A.; Marchetti, C.; Corinaldesi, G. Evaluation of

complication rates and vertical bone gain after guided bone regeneration with non-resorbable membranes versus titanium meshes and resorbable membranes. A randomized clinical trial. *Clin. Implant Dent. Relat. Res.* **2017**, *19*, 821–832.
122. Eskan, M.A.; Girouard, M.-E.; Morton, D.; Greenwell, H. The effect of membrane exposure on lateral ridge augmentation: a case-controlled study. *Int. J. Implant Dent.* **2017**, *3*, 26.
123. Wang, J.; Chen, N.; Ramakrishna, S.; Tian, L.; Mo, X. The effect of plasma treated PLGA/MWCNTs-COOH composite nanofibers on nerve cell behavior. *Polymers (Basel).* **2017**.
124. Binkley, D.M.; Lee, B.E.J.; Saem, S.; Moran-Mirabal, J.; Grandfield, K. Fabrication of polycaprolactone electrospun nanofibers doped with silver nanoparticles formed by air plasma treatment. *Nanotechnology* **2019**.
125. Sheikh, Z.; Najeeb, S.; Khurshid, Z.; Verma, V.; Rashid, H.; Glogauer, M. Biodegradable materials for bone repair and tissue engineering applications. *Materials (Basel).* **2015**, *8*, 5774–5794.
126. Tiwari, A.P.; Joshi, M.K.; Park, C.H.; Kim, C.S. Nano-Nets Covered Composite Nanofibers with Enhanced Biocompatibility and Mechanical Properties for Bone Tissue Engineering. *J. Nanosci. Nanotechnol.* **2017**.
127. Sharif, F.; Tabassum, S.; Mustafa, W.; Asif, A.; Zarif, F.; Tariq, M.; Siddiqui, S.A.; Gilani, M.A.; Ur Rehman, I.; MacNeil, S. Bioresorbable antibacterial PCL-PLA-nHA composite membranes for oral and maxillofacial defects. *Polym. Compos.* **2019**.
128. Choukroun, J.; Adda, F.; Schoeffler, C.; Vervelle, A. Une opportunité en paro implantologie: le PRF. *Implantodontie* **2001**, *42*, 55–62.
129. Fernández-Delgado, N.; Hernández-Ramírez, P.; Forrellat-Barrios, M. Platelet functional spectrum: From hemostasis to regenerative medicine. *Rev. Cuba. Hematol. Inmunol. y Hemoter.* **2012**, *28*, 200–216.
130. Neumann, F.J.; Marx, N.; Gawaz, M.; Brand, K.; Ott, I.; Rokitta, C.; Sticherling, C.; Meinl, C.; May, A.; Schömig, A. Induction of cytokine expression in leukocytes by binding of thrombin-stimulated platelets. *Circulation* **1997**, *95*, 2387–2394.
131. Kankala, R.K.; Xu, X.M.; Liu, C.G.; Chen, A.Z.; Wang, S. Bin 3D-printing of microfibrous porous scaffolds based on hybrid approaches for bone tissue engineering. *Polymers (Basel).* **2018**, *10*, E807.
132. Shi, Z.; Huang, X.; Cai, Y.; Tang, R.; Yang, D. Size effect of hydroxyapatite nanoparticles on proliferation and apoptosis of osteoblast-like cells. *Acta Biomater.* **2009**, *5*, 338–45.
133. Turco, G.; Marsich, E.; Bellomo, F.; Semeraro, S.; Donati, I.; Brun, F.; Grandolfo, M.; Accardo, A.; Paoletti, S. Alginate/hydroxyapatite biocomposite for bone ingrowth: A trabecular structure with high and isotropic connectivity. *Biomacromolecules* **2009**, *10*, 1575–1583.
134. Márton, K.; Tamás, S.B.; Orsolya, N.; Béla, C.; Ferenc, D.; Péter, N.; Csaba, D.N.; Lajos, C.; Zsombor, L.; Eitan, M.; et al. Microarchitecture of the augmented bone following sinus elevation with an albumin impregnated demineralized freeze-dried bone allograft (BoneAlbumin) versus anorganic bovine bone mineral: A randomized prospective clinical, histomorphometric, and micro-com. *Materials (Basel).* **2018**, *11*, E202.
135. Dias, D.R.; Leles, C.R.; Batista, A.C.; Lindh, C.; Ribeiro-Rotta, R.F. Agreement between Histomorphometry and Microcomputed Tomography to Assess Bone Microarchitecture of Dental Implant Sites. *Clin. Implant Dent. Relat. Res.* **2015**, *17*, 732–41.
136. Albrektsson, T.; Brånemark, P.I.; Hansson, H.A.; Lindström, J. Osseointegrated titanium implants: Requirements for ensuring a long-lasting, direct bone-to-implant anchorage in man. *Acta Orthop.* **1981**, *52*, 155–170.
137. Mangano, F.; Raspanti, M.; Maghaireh, H.; Mangano, C. Scanning Electron Microscope (SEM) evaluation of the interface between a nanostructured calcium-incorporated dental implant

surface and the human bone. *Materials (Basel).* **2017**, *10*, 1438.